Symmetry of the Charge Ordering Phases in Hole-Doped Cuprates Studied by Resonant X-Ray Absorption and Scattering

by

Christopher Mackenzie McMahon

A thesis
presented to the University of Waterloo
in fulfillment of the
thesis requirement for the degree of
Doctor of Philosophy
in
Physics

Waterloo, Ontario, Canada, 2019

Examining Committee Membership

The following served on the Examining Committee for this thesis. The decision of the Examining Committee is by majority vote.

External Examiner	Bill Atkinson Associate Professor
Supervisor	David Hawthorn Professor
Internal Member	Robert Hill Associate Professor
Internal-External Member	Guo-Xing Mao Associate Professor
Other Member	Anton Burkov Professor

Author's Declaration

I hereby declare that I am the sole author of this thesis. This is a true copy of the thesis, including any required final revisions, as accepted by my examiners.

I understand that my thesis may be made electronically available to the public.

Statement of Contributions

This thesis derives primarily from three projects that originated in the research group headed by Professor David Hawthorn at the University of Waterloo. The majority of the work on these projects was contributed by graduate students in that group, including myself, along with various collaborators from universities and the accelerator facilities where most of our experiments were performed. In the following, I outline some of the more significant contributions made by the various parties, with particular attention to my personal contributions that ultimately led to the content of this thesis. At the end, I also briefly describe work on other projects that, while not presented in this thesis, occupied a substantial fraction of my efforts over the course of my doctoral degree and provided an invaluable addition to my education as an experimentalist focussed on the electronic structure of the cuprates.

Symmetry of Charge Density Wave Order in the Cuprates

Resonant x-ray scattering (RXS) was refined into a conventional experimental technique using tunable synchrotron-based light sources roughly a decade ago,[1–6] making it a relatively new addition to the spectroscopic toolbox. Its selectivity to the energy and momentum of a targeted electronic transition has allowed researchers to directly observe the three-dimensional angular dependence of individual electronic states in a crystal's unit cell and thus map the density and symmetry of charge on a local scale. In discussions between our research group and collaborators, especially the group of Ricardo Comin at the University of British Columbia, an idea for a new RXS experiment was proposed where the angular dependence of x-ray scattering at the reciprocal space wave vector corresponding to charge density wave (CDW) order could, in a similar way, reveal the local symmetry of the CDW in the cuprates. Such an experiment was subsequently realized and led to two publications, both in Nature Materials. One paper[7] was published jointly with Comin's group and our own, for which a fellow graduate student, Andrew Achkar, led our group's contribution at that time. Working with him, I collected and analyzed much of our published data at the REIXS beamline of the Canadian Light Source (CLS). The second paper,[8] for which I am an author, reported results from additional experiments on YBCO and LBCO that again were conducted at the CLS where our team and I collected and anlyzed most of the data. Much of the contents of these papers are featured in Chapter 3. After this, our group turned its focus to collecting more detailed data on YBCO samples, and I took over as our group's internal lead on the project. The data from these most recent experiments composes the rest of Chapter 3, and at the time of writing, it is being prepared for imminent publication with myself as first author.

Anisotropic Tensor Scattering in La-Based Cuprates

In the La-based cuprates, the (0 0 1) Bragg peak is typically forbidden but can be seen on resonance at low temperatures when the crystal transitions into a structural phase with anisotropy in the electronic structure along the *ab*-plane. Based on the idea that electronic nematic ordering could be discovered by comparing the thermal evolution of the (0 0 1) peak below the transition at different resonant edges, our group collaborated with the group of Jochen Geck at IFW Dresden and others to perform RXS experiments on various La-based samples. Again, I collected much of the data at REIXS, along with students Andrew Achkar and Martin Zwiebler, and am an author of the resulting publication in Science.[9] Subsequently, I led a follow-up study that explored this phenomenon in additional materials with different dopant concentrations. The details and results of this study, along with those of the preceding paper, are the primary focus of Chapter 4, and are being prepared as another publication with myself as first author.

Temperature-Dependent X-Ray Absorption Spectroscopy of YBCO

Stimulated by the success of the preceding study on the La-based cuprates, David Hawthorn proposed a search for similar electronic nematic behaviour in YBCO by studying the thermal evolution of x-ray absorption spectra tuned to the CuO_2 plane states. I took the lead on this project; collecting the data, performing the analysis, and developing the interpretation of their meaning (of course with many discussions between David and I). The culmination of this work is summarized in Chapter 5, and once again the results are currently being prepared for publication with myself as first author.

Additional Works

Outside of the work presented in this thesis, I have been involved—to a sometimes minor, and other times major, degree—in a number of additional projects that our research group has undertaken. This has included twenty-one visits to the CLS and three visits to the SLAC National Accelerator Laboratory where I have spent many thousands of hours conducting experiments at six endstations using a variety of sophisticated spectroscopic techniques ranging from photoemission electron microscopy to femtosecond x-ray diffraction. On many of these visits, I led the project team or operated the endstation solo; or sometimes even ran experiments on two endstations on separate beamlines simultaneously. Several of these projects have led to authored publications including work exploring quenched structural disorder in YBCO,[10] spectroscopic signatures of charge order in electron-doped cuprates,[11] and the effects of oxygen annealing in $LaAlO_3/SrTiO_3$ heterostructures.[12,13]

Abstract

In the underdoped cuprates, superconductivity coexists with a rich variety of other electronic orders. Understanding the nature of these orders, how they interact with one another, and the mechanisms that produce them is key to understanding the electronic behaviour of this important class of quantum materials. In this dissertation, we report on the results from three novel experiments that used resonant x-ray spectroscopy to explore the symmetry of the charge density wave (CDW) and other phases in La- and Y-based cuprates. For the uninitiated reader, a brief theoretical description of the experimental methods is also provided.

Theoretical proposals have suggested that CDW order in the cuprates may adhere to a d-symmetry form factor, where charge on the O sites surrounding Cu in the CuO_2 planes modulates out of phase and produces a quadrupolar local environment. This is supported by STM measurements in $Bi_2Sr_2CaCu_2O_{8+x}$ and $Ca_{2-x}Na_xCuO_2Cl_2$ and resonant x-ray scattering in $YBa_2Cu_3O_{6+x}$ (YBCO). We conduct our own resonant scattering measurements on $La_{1.875}Ba_{0.125}CuO_4$ and find evidence for a monopolar CDW, confirmed at both the O and Cu absorption edges where the measurement selectively probes the respective in-plane orbitals. Studying the (0 0.31 L) CDW peak at the Cu edge in YBCO, we again find the same result. Furthermore, using an alternative measurement geometry that is more sensitive to the symmetry of the CDW, we are able to contrast our results against a previous study that was limited by experimental accuracy. Finally, we find a surprisingly different symmetry at the (0.31 0 L) peak in YBCO that indicates the presence of orbital order alongside simple charge order. Model calculations for this data propose a CDW with significant in-plane anisotropy, or perhaps with a modulating orbital orientation.

Anisotropy in electronic structure that arises from strong correlations—classified as electronic nematicity—has been observed in multiple cuprates, and whether or not this electronic ordering phase should be suspected as a generic feature of the underdoped phase diagram has become a topic of debate. Exploiting a unique structural distortion in the La-based cuprates, we perform anisotropic tensor scattering (ATS) on resonance in samples with a variety of isovalent and heterovalent dopings to investigate the relationship between structure, CDW order, and electronic nematic order. In four of the five samples, we observe a temperature evolution that is distinct from the structural distortion in the spectra that corresponds to orbitals in the CuO_2 plane, indicating the presence of an electronic nematic phase. Like CDW order, this phase often onsets at the same temperature as the structural distortion, or else below the base temperature of our spectrometer. However, the CDW is clearly seen to onset at a moderately lower temperature than the other phases in $La_{1.65}Eu_{0.2}Sr_{0.15}CuO_4$, revealing an enhancement in the electronic nematicity at T_{CDW}.

We argue that the extent of the tilt in the structural transition, which varies with the unit cell volume, could provide an underlying connection between the properties of the three phases.

In an attempt to observe evidence of an electronic nematic state in YBCO, polarized near-edge x-ray absorption spectroscopy is performed at the Cu L and O K edges in three samples that span the material's doping phase diagram: $\delta = 0.335$, $\delta = 0.5$, and $\delta = 0.999$. We argue that electronic nematicity could be observed as a relative change in the temperature evolution of the unoccupied density of states projected along the crystal's a- and b-axes, perhaps as the spontaneous increase of anisotropy below a threshold temperature. We report a modest reduction and broadening of many peaks in the spectra as temperature increases, including at both absorption edges, all dopings, and all polarizations. Alternatively, the peaks associated with the upper Hubbard band and the twin peaks in the c-axis spectra increase. Substantial spectral weight also appears in the region just below the upper Hubbard band. We propose that phonon coupling through a Franck-Condon mechanism could be responsible for the latter effect. The x-ray linear dichroism is calculated between the a- and b-axis spectra, but only subtle changes to the anisotropy are apparent. Ultimately, the presence of an electronic nematic phase cannot be verified, and our results instead provide an upper-limit for the magnitude of any effects from such a phase on the absorption spectra.

Acknowledgements

This thesis would not have been possible without the help and support of a great number of people in particular, and the condensed matter communities at the University of Waterloo and the Canadian Light Source synchrotron in general.

As is customary, and in this case well-deserved, I must single-out my supervisor David Hawthorn before all others. His teachings informed every aspect of this work, and I sincerely believe my success would not have been possible without his guidance, support, understanding, and motivation. Thanks, Dave, for everything.

Next, I must give thanks to my fellow group members and student experimenters, especially Haofei Wei, Andrew Achkar, Xiaopan Mao, Rantong Gong, Tianyu Shi, Isaiah Djianto, Jyler Menard, Silas Vriend, Martin Zwiebler, and Jacob Ruf. Our many discussions added immensely to my learning, and having teammates with whom to share the load while working for so many days and nights under the deafening hum of the synchrotron added infinitely to my enjoyment.

I must also thank the many professors and scientists at the University of Waterloo and the Canadian Light Source that so generously offered their help and advice. This is especially heartfelt for Ronny Sutarto, Tom Regier, Feizhou He, and Teak Boyko who not only provided their expertise, but also their labour on the beamline, often at ungodly hours. (May your families forgive you!) And of course, I am indebted to those who aided me off the beamline, too. Though it isn't discussed as often, a PhD student's course work and TA duties present an equally daunting challenge as his research. I cannot possibly list everyone who has helped me in this arena, but I will quickly thank Jeff Gardiner, Tan Dinh, and Stefan Idziak.

Of course, none of the people I just mentioned would be able to do their jobs without the administrative staff who keep the academic machine oiled and running. I especially want to thank Judy McDonnell and Anja Drygala who were forced to endure the brunt of my bureaucratic incompetence. On behalf of everyone in the department, but especially myself, I just want to say, sorry for handing in absolutely every form late and riddled with errors.

I would be remiss not to mention the innumerable contributions made behind the scenes of this thesis. First, there are the many people who built, run, maintain, and perpetually fix the CLS synchrotron. It is truly a wonder that such a complicated facility can provide the effortless interface that its users enjoy. And second, there are the crystal growers who provided not only the samples in this thesis, but the countless hours of research in the

science of crystal growth that I, and all of us in the condensed matter community, might otherwise take for granted.

I must thank NSERC, CIFAR, the University of Waterloo, and the many other funding agencies that directly or indirectly paid for my research efforts, my travel, and my attendance at a number of delightful conferences and summer schools.

Finally, I wish to offer my deepest thanks to my family and friends who have seen me through the long journey of my graduate education. It has, with little contest, contained some of the best and worst moments of my life, and I cannot express how lucky I am to have had all of you to share in my many frustrations and celebrations. To my parents Jodi and Brian; my sister Jasmine; my close friends Benji, Kevin, Donald, Kier, Kyle, and Will; and of course my beloved cheerleader and favourite distraction Stephanie; I cannot thank you enough, but that will never stop me from trying.

Dedication

To Stephanie,
who today receives her honorary
doctorate in patience.

Table of Contents

List of Figures **xiii**

1 Introduction **1**

1.1 Superconductivity in the Cuprates 4

2 X-Ray Spectroscopies **13**

2.1 X-Ray Absorption Spectroscopy 13

2.1.1 The Absorption Coefficient 14

2.1.2 The One-Electron Model 15

2.1.3 Fluorescence and Electron Yield Techniques 17

2.1.4 The Configuration Picture 20

2.1.5 A Quantum Treatment of Absorption 21

2.2 X-Ray Diffraction 24

2.2.1 Scattering from Electrons 25

2.2.2 Scattering from an Atom 27

2.2.3 Scattering from a Lattice 28

2.3 Resonant X-Ray Scattering 29

2.3.1 A Quantum Treatment of Scattering 30

2.3.2 Comparison with Nonresonant Diffraction 33

2.3.3 Element and Orbital Specificity 34

2.4 X-Ray Photoemission Spectroscopy 36

3 Symmetry of the Charge Density Wave Orbital Form Factor Studied with Resonant X-Ray Scattering **39**

3.1 Experiment . . . 41
3.2 Modelling the Form Factor . . . 46
3.3 Results and Discussion . . . 48
3.3.1 LBCO . . . 48
3.3.2 YBCO . . . 53
3.4 Summary . . . 61

4 Observing Electronic Nematic Order in the La-based Cuprates with Anisotropic Tensor Scattering **62**

4.1 The Electronic Nematic Phase . . . 63
4.2 The La214 Cuprates . . . 66
4.3 ATS Scattering . . . 70
4.4 Experimental Results and Discussion . . . 72
4.4.1 Group I Samples . . . 73
4.4.2 Group II Samples . . . 88
4.5 The Effect of Tilt Angle on Electronic Nematicity . . . 99
4.6 Summary . . . 104

5 Temperature Dependent XAS of Oxygen-Doped YBCO **106**

5.1 Introduction . . . 106
5.2 Experimental Considerations . . . 109
5.3 Results and Discussion . . . 110
5.3.1 Doping Dependence . . . 110
5.3.2 Temperature Dependence . . . 113
5.4 Conclusions . . . 118

6 Conclusion **125**

References **128**

List of Figures

1.1 Evolution of discovered T_c's over time . . . 3
1.2 Crystal Structure of the Cuprates . . . 6
1.3 d-symmetry of the order parameter from ARPES . . . 7
1.4 Generic cuprate phase diagram . . . 8
1.5 New cuprate phase diagram . . . 10
1.6 Comparison of CDW's between branches of the cuprates . . . 11

2.1 The Absorption Coefficient . . . 14
2.2 One-Electron Model of XAS . . . 16
2.3 Example XAS Spectrum . . . 17
2.4 The TFY & TEY Processes . . . 18
2.5 The Resonant Scattering Process . . . 33
2.6 Example XPS Spectrum . . . 37

3.1 Symmetry types of a CDW . . . 40
3.2 Experimental geometry . . . 42
3.3 CDW peak intensity of LBCO and YBCO-6.67 with background fits . . . 45
3.4 LBCO: ϕ-dependence . . . 49
3.5 LBCO: L-dependence . . . 52
3.6 Intensity of the CDW K-peak for YBCO-6.75 as a function of azimuthal angle 54
3.7 Measurements of I_σ/I_π ratio . . . 55

3.8 Temperature dependence of the CDW H-peak for YBCO-6.67 58
3.9 Ionic displacements in the CDW of YBCO 59
3.10 Proposed CDW in YBCO with nonzero off-diagonal terms in its scattering tensor 60

4.1 Nematic and smectic phases 64
4.2 La214 crystal structure 67
4.3 LTO and LTT distortions 68
4.4 *ab*-plane layering 69
4.5 Phase diagram of LBCO 70
4.6 Energy dependence of the 001 peak at the Cu L and O K edge of LBCO(i) 74
4.7 Temperature series of the (0 0 1) La M edge in LESCO 76
4.8 Temperature series of the (0 0 1) peak at the Cu L edge in LESCO 77
4.9 Temperature dependece of ATS intensity in LBCO, LESCO, and LNSCO showing electronic nematicity 80
4.10 Modelling of azimuthal dependence of a nematic scattering form factor . . 82
4.11 Energy dependence of the CDW peak in LBCO(i) 84
4.12 L dependence of the CDW peak in LBCO(i) 84
4.13 Temperature series of the CDW peak in LBCO(i) 86
4.14 Comparison of nematicity and CDW order in LBCO(i), LESCO, and LNSCO(i) 87
4.15 Temperature series of the ATS peak in LNSCO(ii) 90
4.16 Temperature dependence of the ATS intensity in LNSCO(ii) showing electronic nematicity 91
4.17 Search for the CDW peak in LNSCO(ii) 93
4.18 Temperature series of the ATS peak at the Cu, Ba, and La edges in LBCO(ii) 94
4.19 Temperature dependence of the ATS peak for the Ba, Cu, and La edges of LBCO(ii) 95
4.20 Temperature series of the ATS peak at the apical and in-plane O edges of LBCO(ii) 97

4.21 Comparison of the temperature dependence of the ATS peak between the O and Cu edges in LBCO(ii) 98
4.22 CDW peak in LBCO(ii) 100
4.23 Comparison of ATS and CDW peak intensities in LBCO(ii) 101
4.24 Phase diagram of LNSCO showing critical tilt angle 103

5.1 O K spectra showcasing overlap far from the edge 110
5.2 Comparison of Cu edge spectra for two identical samples 111
5.3 Low-temperature Cu edge XAS 112
5.4 Low-temperature O edge XAS 114
5.5 Temperature dependence of the $\delta = 0.335$ sample at the Cu edge. 115
5.6 Temperature dependence of the $\delta = 0.5$ (o2B) sample at the Cu edge. . . . 116
5.7 Temperature dependence of the $\delta = 0.5$ (c2) sample at the Cu edge. 117
5.8 Temperature dependence of the $\delta = 0.999$ sample at the Cu edge. 120
5.9 Temperature dependence of the $\delta = 0.335$ sample at the O edge. 121
5.10 Temperature dependence of the $\delta = 0.5$ sample at the O edge. 122
5.11 Temperature dependence of the $\delta = 0.999$ sample at the O edge. 123
5.12 X-ray linear dichroism 124

Chapter 1

Introduction

At the beginning of 1986, physicists thought they understood superconductivity. The year was just shy of the 30$^{\text{th}}$ anniversary of the publication of the famous papers from Bardeen, Cooper, and Schrieffer that explained the quantum mechanism by which electrons in a solid can pair up to circumvent the Pauli exclusion principle and collapse into a many-particle, energy-gap-protected wavefuction.[14,15] Unknown to the field, however, J. Georg Bednorz and K. Alex Müller, working at the IBM Research Laboratory in Zurich, were about to make an historic observation while searching for evidence of superconductivity in new materials. Studying copper oxide compounds (known as cuprates), they were unsure of the likelihood of their success and chose to work almost in secret—experimenting after hours with their colleagues' equipment.[16] After months of tests, they found success in a sample of $La_{5-x}Ba_xCu_5O_{5(3-y)}$ that exhibited a superconducting transition temperature as high as $T_c = 35$ K at certain dopings.[17–19] This was 50% greater than the highest-known transition temperature at the time[20,21] and well above the expected natural limit.[22] Word of the discovery ignited a flurry of activity in dozens of research groups, and at the following APS March Meeting of 1987 in New York, this result and several others like it were presented to an overflowing crowd of two thousand people in a session that stretched on past three in the morning.[16] Later that year, Bednorz and Müller shared the Nobel Prize.

Clearly, the potential impact that a high-temperature superconductor could make on our world was not lost on the physics community then, and it continues to motivate research today. Superconductors hold the key to advancements in a plethora of technologies ranging from novel electronic devices, improved magnetic resonance imaging, more efficient power transmission and generation, and (every physics lab instructor's favourite example) magnetically-levitated trains, to name only a few. However, the extremely-low transition

temperatures of conventional superconductors requires cooling with liquid helium, which makes them woefully impractical in most situations. If a superconductor could be found that operated with more conventional cooling methods, or even none at all, the practical obstacles would be removed and a technological revolution unleashed.

While a room-temperature superconductor continues to remain the holy grail of condensed matter physics (i.e. mythological), it is not unreasonable to hold onto hope that the quest may find a successful end in the near future. Over the past century, the record for the highest-known T_c has continued to move—sometimes slowly and sometimes dramatically—and many materials have been discovered that no longer require liquid helium (Figure 1.1). In fact, just months after Bendnorz's and Müller's inital report, the first cuprate known to superconduct above the boiling point of nitrogen was already discovered (and in fact the results were presented at the same March Meeting session[16,23]). Today, a number of cuprates are known to have a T_c well above 100 K, and this family remains a leading candidate to be hiding a yet undiscovered material that will break the room-temperature barrier. After all, the current record, set in 2015, is surprisngly held by the *conventional* superconductor sulfur hydride with a T_c that exceeds 200 K when under 200 GPa of pressure.[24] This is more than an order of magnitude warmer than most conventional superconductors, and thus in juxtaposition, the comparatively small factor of two separating today's unconventional cuprate superconductors from room temperature could yet be achievable with further understanding and technological progress.

Technological benefits aside, solving the problem of high-temperature superconductivity is enticing for its own sake. After three decades of intense study, the mechanism (or perhaps multiple mechanisms) underlying unconventional superconductivity remains elusive despite tremendous advances in our knowledge of the materials in which it inhabits. The phenomenon has been measured in well over one hundred compounds[16] including a vast library of cuprate perovskites, but it has also notably been found in iron-based pnictides (first discovered in 2006[25–27]) and an array of compounds under high pressure. Hundreds of thousands of research papers (funded with uncountable grant money) have been published on the topic, and it can be credited with driving important advances in both experimental and theoretical techniques.[28] Notably (but not comprehensively), it has been the motivation for extensive research in and the further development of ARPES, neutron scattering, STM, NMR, RXS, XRD, XAS, transport, quantum oscillations, and the science of material growth and characterization. Similarly, myriad theoretical studies have exploited and extended such tools as the Hubbard, $t-J$, spin-fermion, and Landau models; resonating valence bond, loop current, intertwined order, charge and spin density wave order, pair-density wave order, nematic Fermi fluids, and Ampearan pairing frameworks; and quantum Monte Carlo, density matrix renormalization group, exact diagonalization,

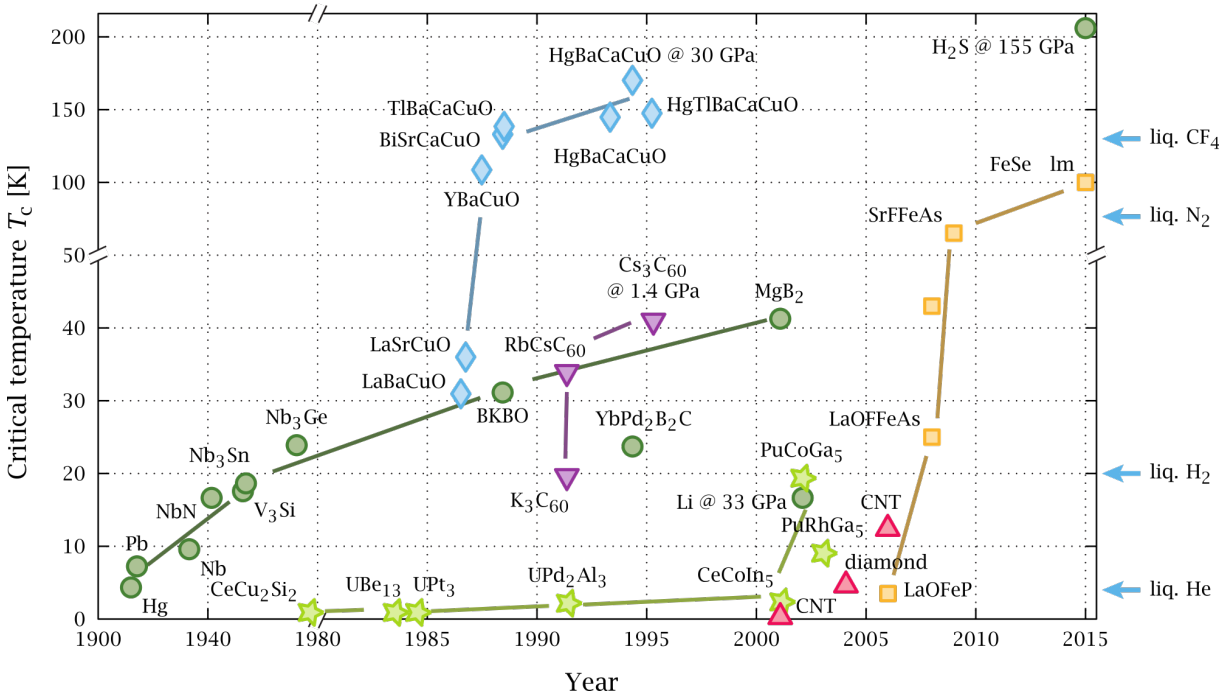

Figure 1.1: A history of the discoveries of superconducting compounds showing the accumulation of known T_c's over time. Conventional superconductors are shown as dark green circles, starting with Onnes' 1911 discovery of Hg. Cuprates are light blue diamonds, and the iron-based pnictides are orange squares. (Figure adapted from Wikipedia.)

and dynamical mean field theory numerical techniques.

Clearly, the body of work upon which our understanding of the cuprates and other unconventional superconductors has been built is enormous, and thus it is unfortunately beyond the scope of this work to attempt to provide anything but the briefest of summaries of the relevant physics, experimental considerations, material properties, and current state of the sub-field relating to the research presented in the following chapters. It must inevitably be the case that important aspects of the field are absent from this text, for which I can do nothing but ask for the reader's understanding and forgiveness. It must also be assumed that the reader has considerable general knowledge of the subject *a priori*, and the reader is encouraged to consult any number of excellent review articles that are available in the literature to supplement their knowledge, if necessary. For example, Refs. 29–35 are quite enlightening (though by no means exhaustive). In what remains of this chapter, a very short review of superconductivity and charge ordering in the cuprates is provided so far as to illuminate the motivations behind the studies presented in Chapters 3-5. Summaries of those chapters—their objectives, experimental setups, results, and interpretations—are then provided. Additionally, in Chapter 2, an overview of the theoretical foundations underlying the experimental techniques utilized in this dissertation is given, which is required for an accurate interpretation of the discussed data.

1.1 Superconductivity in the Cuprates

BCS theory,[14,15] along with the theories of Ginzburg-Landau[22,36] and Eliashberg,[37] essentially show that in materials with itinerant electronic states, if any attraction exists between electrons (no matter how weak) those electrons will bind together into Cooper pairs with opposite spin and crystal momenta. In conventional superconductors, this attraction is provided via phonon-mediated interactions, which in a cartoon picture amounts to a perturbing of the symmetry of the ionic lattice by a passing electron to briefly produce a region of attractive, net-positive charge in its wake. In the cuprates, however, lattice vibrations are too weak to generate superconductivity by this mechanism far above about 30 K.[38] Furthermore, the canonical example of conventional superconductivity occurs in an isotropic Fermi fluid (i.e. a simple metal like aluminium), and it is not clear if and how the theory can be applied to a ceramic Mott insulator with a crystal structure that confines the superconducting charge carriers into quasi-two-dimensional CuO_2 planes (Figure 1.2). As correctly predicted by Anderson, this confluence of Mott-Hubbard physics and low-dimensionality leads to fundamentally new behaviour that the traditional condensed matter frameworks available at the cuprates' initial discovery could not accurately

describe.[31,39]

Following the initial reports of superconductivity in the cuprates, evidence detailing its peculiar properties quickly amassed. One of the most notable was that the order parameter, proportional to the size of the energy gap, changes sign with direction, vanishing at nodes along the quadruply-degenerate $(0,0)$–(π,π) direction (Figure 1.3). In a two-dimensional system, this corresponds to an order parameter with $d_{x^2-y^2}$-symmetry where each pair forms with $L = 2$ angular momentum.[40–44] This is in stark contrast to the isotropic s-symmetry of conventional superconductors that are devoid of internal angular momentum[38,45] and suggests a pairing mechanism based on solely electronic interactions.[46]

Additionally, magnetism plays a very important role in the cuprates' doping-dependent phase diagram. Conventional wisdom would argue that superconductivity and magnetism don't get along due to the opposite spins necessary in Cooper pairing—a property that the cuprates likely share with conventional superconductors. However, the prominence of magnetic interactions in the cuprates follows naturally from the half-filled Mott insulating state of their parent compounds. The super-exchange interaction leads to antiferromagnetic ordering of the charge carriers' spins below Néel transition temperatures as high as 500 K,[48] but upon doping (with either electrons or holes), magnetic defects are introduced that destroy the long range order. Competing forces then lead to new spin and charge ordering phases (see below). With sufficient doping, the high concentration of defects eventually breaks up the Coulombic traffic jam, and metallic conduction can flow through the partially filled Hubbard band (the upper Hubbard band for electron doping and the lower Hubbard band for hole). Between this "overdoped" state of itinerant electronic bands and the "underdoped" state of strong Coulombic repulsion that localizes electrons into atomic-like orbitals with antiferromagnetic spin order, superconductivity emerges from the compromise in a region with strong electronic correlations. On the underdoped side, as antiferromagnetism is suppressed, magnetism can persist in manifestations such as static magnetism or dynamic spin susceptibillity,[49] and the precise nature of its evolution with doping is likely intimately linked with the stability of the superconducting phase. In fact, it has been argued that antiferromagnetic spin fluctuations may be the specific interaction through which the superconducting electrons pair,[49–51] perhaps similarly to what is seen in some heavy Fermion superconductors.[52] Whatever the case, however, it is certain that a theory of superconductivity in the cuprates must take magnetism into account.

The most famous, and arguably most intriguing, difference between conventional superconductors and the cuprates is the so-called pseudogap phase that resides above the underdoped shoulder of the superconducting dome in the hole-doped (and perhaps electron doped[53]) phase diagram, identified in Figure 1.4.[29–31,35,38,52,54] A concise description of the physics in this region remains elusive, but its namesake comes from what appears to be a

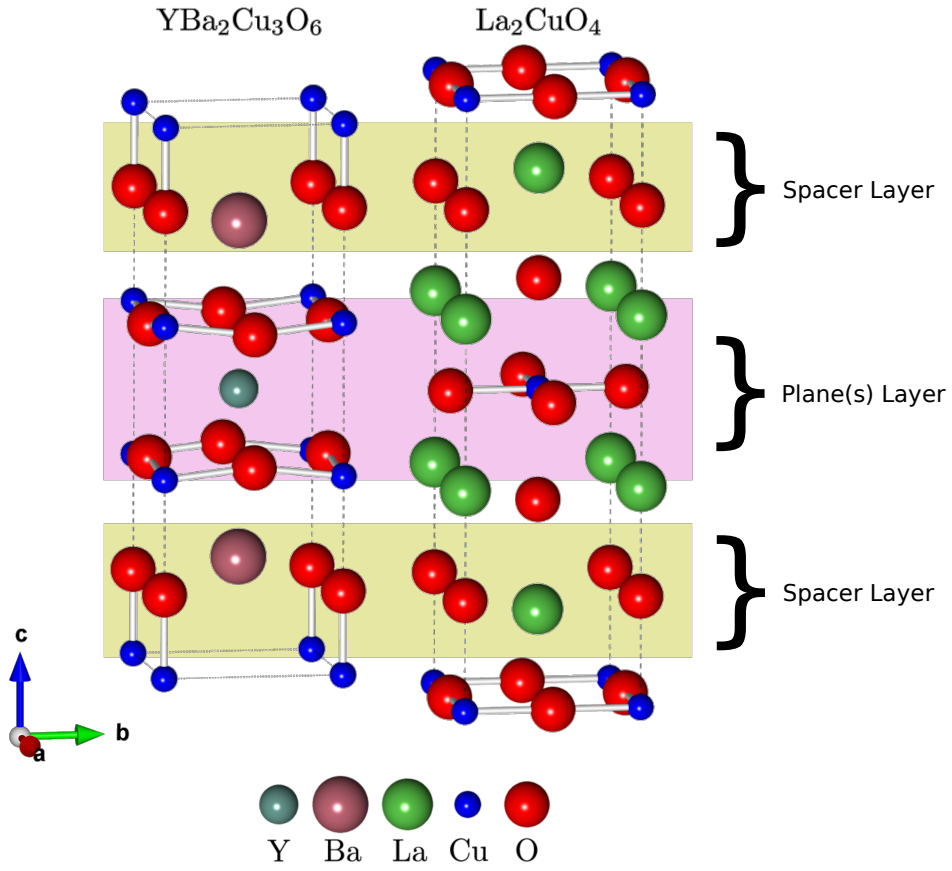

Figure 1.2: General crystal structure of the cuprates, illustrated with two widely-known, undoped parent materials: YBCO (left) and LCO (right). All cuprates share a similar layered structure with one (LCO) or more (YBCO) CuO_2 planes that run parallel to the a and b crystallographic axes (roughly highlighted in gold to guide the eye), and spacer layers in-between composed of rock salt oxides (lavender). Superconducting charge carriers reside primarily in the planes, while the spacer layers provide a "reservoir" of charge that dope electrons or holes into the planes.

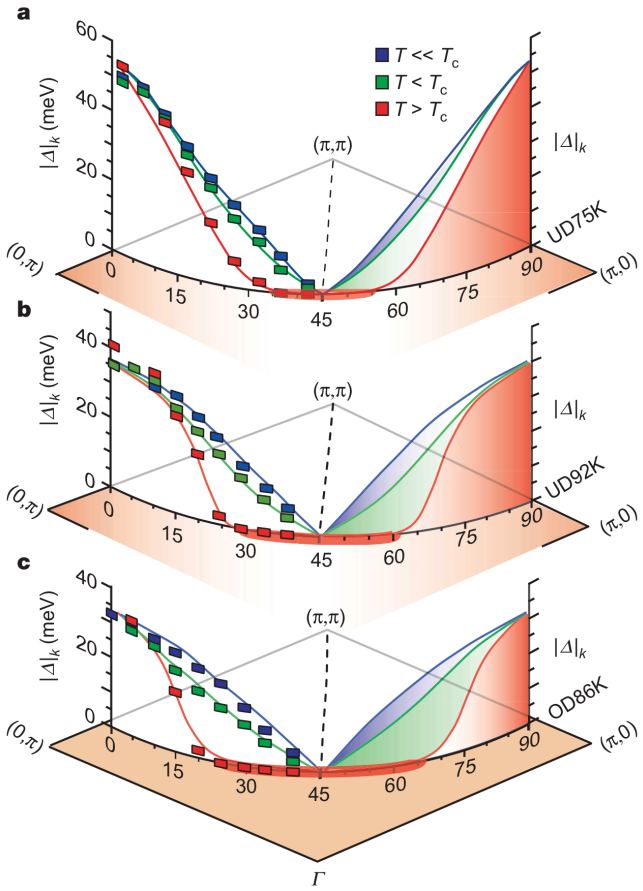

Figure 1.3: ARPES spectra showing the angular dependence of the energy gap in underdoped (a,b) and overdoped (c) $Bi_2Sr_2CaCu_2O_{8+\delta}$ in the first quadrant of the Brillouin zone. At temperatures below T_c (blue and green lines), the $d_{x^2-y^2}$ node where the gap vanishes is clearly seen along the (π, π)-direction. Above T_c (red), the spectra "smear out" to create gapless Fermi arcs at the nodes, but the gap at the antinodes shows little change until the temperature is increased much further to approach T^*. (Figure adapted from Ref. 47.)

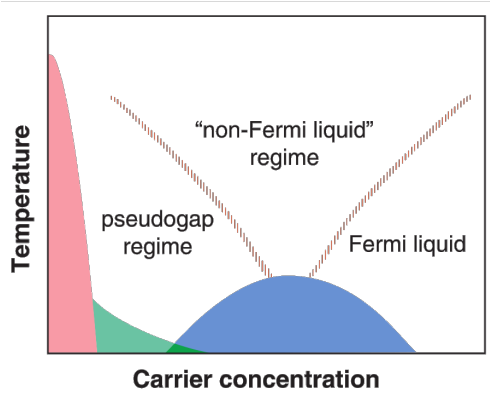

Figure 1.4: Schematic of the cuprates' generic phase diagram as a function of doping. Antiferromagnetic order (red), superconducty (blue), and magnetic order (green) phases are shaded. The charge carriers can be either electrons of holes, though the existence of the pseudogap in electron-doped materials is less well established. Additionally, the superconducting dome is much larger, with both a broader range of carrier concentrations and higher T_c, and the antiferromagnetism extinguishes much more quickly for hole doping. (Figure adapted from Ref. 31.)

gap opening up in the Fermi surface below a critical temperature T^*. ARPES measurements clearly witness a gap-like feature with a similar symmetry as the superconducting order parameter, but it mysteriously maintains the same magnitude above and below T_c, with only a filling-in of the density of states inside the gap as temperature increases (see Figure 1.3).[45,55–57] As a result, excitation spectra exhibit broad, enigmatic peaks above T_c.[38] Furthermore, the precise location of T^* as a function of doping appears to vary somewhat depending on the experimental technique being used,[54] but a discernible change at an upper phase boundary is almost universally observed across probes of the electronic structure.[52]

Theorists have struggled to devise a robust description of the pseudogap that can account for the large body of experimental results as a whole, but leading theories have fallen into two categories. In the first, the pseudogap is proposed to be a precursor to superconductivity. The phase is "attempting" to form at temperatures above T_c but is unable to fully materialize. As a result, some of its signatures are recognizeable in experiment while others remain absent. The dominant example of this centres around coherence of the superconducting wavefunction, which is required for electrons to fall into the many-particle condensate.[58] Essentially, it is predicted that the electrons begin pairing at temperatures as high as T^*, creating the characteristic gap in the excitation spectrum, but thermal noise prevents widespread coherence until the system is cooled to T_c, at which point long-range

superconductivity can develop. If correct, this theory would predict the presence of superconductivity on short scales of time and distance in the pseudogap region, and indeed some evidence for this has been found at temperatures moderately above T_c.[59,60]

The second category of theories claims that the pseudogap is evidence of one or more electronic phases that are distinct from superconductivity appearing at temperatures above T_c. These phases could produce features of the pseudogap directly, or they could do so indirectly through their interactions with superconductivity. Substantial evidence for this scenario has too been found, specifically in the form of charge and spin density waves. Tranquada and collaborators were the first to witness direct evidence via neutron scattering in $La_{1.6-x}Nd_{0.4}Sr_xCuO_4$, where it is now known that the famous "stripe order" occurs across materials in the La-branch of the cuprates.[61] This phase constitutes a combination spin-and-charge density wave that collects the plane layer's doped holes into rivers of charge that serve as an antiphase boundary separating regions of antiferromagnetism. (For a detailed description of the stripe phase, the limits of the theoretical model, and the body of experimental evidence, we refer the reader to a comprehensive review such as Ref. 29.) At the time, it was not known if such a phase was universal in the cuprates or a peculiarity of La-based compounds, with the latter possibility bolstered by the presence of a strutrucal phase transition that typically occurs at the same onset temperature and is unique to this branch of the cuprates (see Chapter 4). Furthermore, the stripe model is expected to be intrinsically stable at a doping of 1/8 holes per unit cell, and the La-cuprates coincidentally experience a suppression of T_c at that doping (the so-called *1/8 anomaly*) that is far more dramatic than anything seen in other compounds. After almost ten years of debate, the phenomenon of density wave ordering was at last found in other cuprates, namely $Bi_2Sr_2CaCu_2O_{8+\delta}$[62] and $Ca_{2-x}Na_xCuO_2Cl_2$,[63] using scanning tunnelling microscopy. However, the absence of an ordering peak in diffraction experiments left room for prudent skepticism about the interpretation of these discoveries, especially with respect to their comparibility with other cuprates.[64] Finally in 2012, after previous studies on the Y-based cuprates had come up empty,[65] clear evidence of electronic ordering in cuprates outside the La-branch was discovered as a charge density wave in $YBa_2Cu_3O_{6+\delta}$ by Ghiringhelli *et al.* using resonant x-ray scattering,[66] followed by further characterization and study by our group and others.[7,8,10,64,67,68]

After additional studies of the materials just discussed, as well as the observation of charge order in a Hg-based cuprate[69] and the onset of stripe order in some La-based cuprates at temperatures distinct from the structural transition,[70] it is now believed that charge density wave order in the underdoped regime of the hole-doped cuprates is in fact a generic phenomenon,[8,9,64] and our understanding of the cuprates' complex phase diagram has needed to evolve (Figure 1.5). Intriguingly, the maximum onset temperature at which

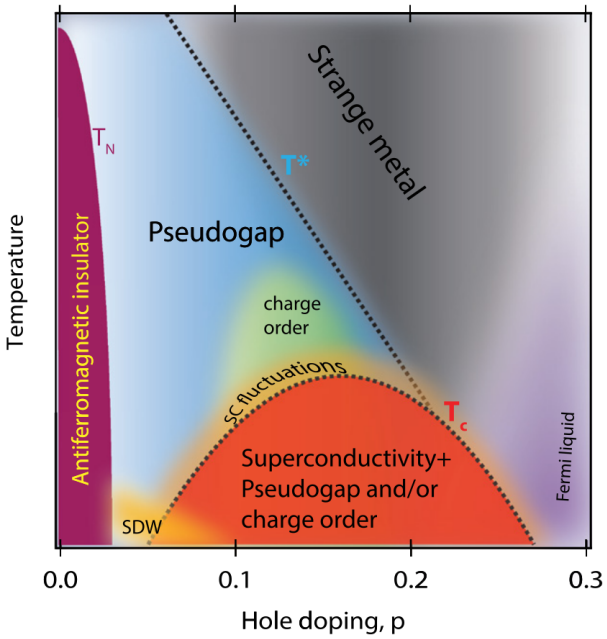

Figure 1.5: An updated version of the hole-doped cuprates' generic phase diagram showing the newly-accepted features of charge ordering on the underdoped side of the superconducting dome with onset temperature below T^* and superconducting flucuations at moderate temperatures above T_c. It is an open question if the origins of the pseudogap can be traced to one, both, or neither of these phenomena. (Figure adapted from Ref. 54.)

ordering occurs as a function of doping roughly coincides across the cuprate family tree (Figure 1.6(a)), specifically optimized above the notorious 1/8 dip in T_c. This suggests that the phenomenon competes with superconductivity. Furthermore, experiments have shown that the strength of the charge ordering decreases at temperatures below the onset of superconductivity and increases when superconductivity is weakened with a magnetic field.[71] It is thus becoming widely accepted that competition with superconductivity is a universal hallmark of the phase.[8,9,64] In addition, as can be seen in Figure 1.6(b), the wavevector at which the ordering occurs, which is consistently incommensurate with the crystal lattice, has been mapped out as a function of doping and takes on different ranges of values between branches of the cuprate family. While the Y- and Bi-based compounds show a monotonic decrease with carrier concentration, the La-based materials show an increase with a sudden change at 1/8 doping that is likely directly related to its unique stripe order pattern.

While our understanding of the cuprates and their electronic ordering phases has in-

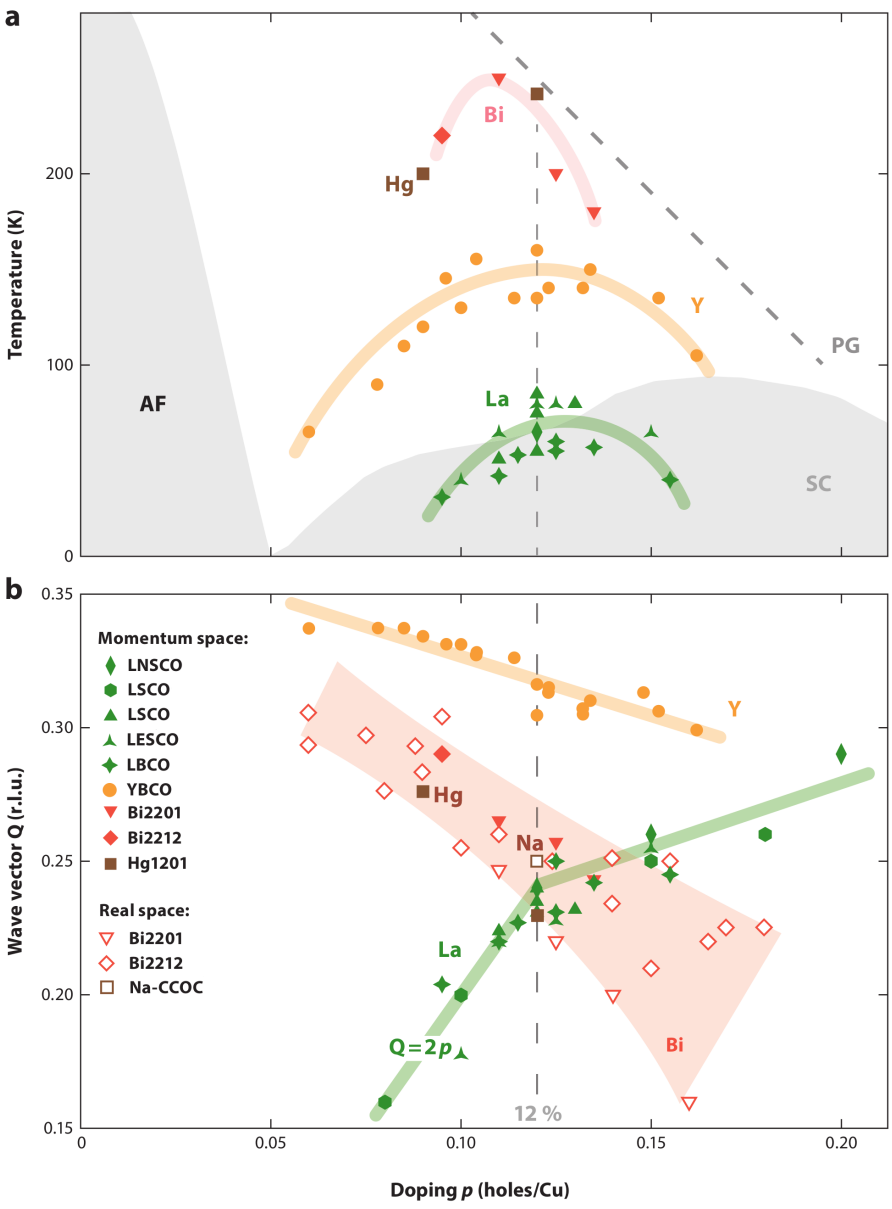

Figure 1.6: Characterization of charge density wave order in the hole-doped cuprates, with the Bi- (pink), Y- (orange), La- (green), and Hg-based (brown) compounds separately indicated for comparison. (a) The onset temperature has different values between material branches but optimizes around the same doping value of 1/8. (b) The incommensurate wavevectors are shown as a function of doping, measured with both real space (hollow) and momentum space (solid) probes. A different pattern of behaviour identifies each branch. The La-based compounds stand out with an increasing wavevector with doping and a kink at 1/8. (Figure adapted from Ref. 64.)

creased remarkably since their early discoveries, important questions endure. While the presence of charge density wave order appears to lower T_c, it is unclear if the two phases share a common origin. Questions also remain about how the two phases interact on the microscopic level; for example if they exhibit phase separation or spatially superimpose. Is it possible to design a cuprate with suppressed charge ordering and enhanced T_c, and does optimization require the elimination of charge order or a proper balance between the phases? Theories about stripe order in particular have suggested that the congregation of charge carriers could induce pairing that might explain the opening of the pseudogap at high temperatures, followed by superconducting fluctuations and large-scale superconductivity as temperature decreases,[38,72–76] but they remain open areas of research. Another question of significant importance is whether or not other ordering phases are waiting to be found in the phase diagram. After all, substantial parameter space remains where charge density wave order cannot explain the observed phenomena of the pseudogap (Figure 1.5). In particular, the cuprates have been described in terms of an electronic liquid crystal[72,73] where multiple phases that originate from strong correlations may appear at differing temperatures and pressures. A nematic phase, for example, where the electronic structure spontaneously breaks rotational symmetry, has been theorized to explain some of the measured properties (see Chapter 4). The research presented in this thesis aims to elucidate some of the mysteries surrounding these questions in the hope that incremental progress toward a robust understanding of the universal properties of the cuprates can be made. We specifically focus on electronic ordering in the La- and Y-based hole-doped cuprates: their symmetry and the potential relationship between charge density wave and nematic phases.

Chapter 2

X-Ray Spectroscopies

For over a century, X-ray spectroscopy has proven to be a formidable tool for the study of materials. Beginning as a way to determine crystal structures, modern advanced x-ray techniques are routinely used to study a plethora of subtle and intricate charge, spin, and structural phenomena in both static and dynamic domains. In this chapter, the theories behind three well-established techniques are explored in an effort to lay the ground work for the experimental studies presented in later chapters. X-ray absorption spectroscopy (XAS) is discussed first. This begins with a semi-classical description and a quick overview of two common methods for performing XAS experiments in the soft x-ray regime. The origins of XAS are then described from a purely quantum mechanical prospective before moving on to the technique of x-ray diffraction (XRD). Here again, the classical Bragg-equivalent description is provided before wading into the more complicated details of resonant x-ray scattering (RXS) that require a quantum mechanical treatment. Finally, x-ray photoemission spectroscopy (XPS) is briefly described in terms of its similarity and complementarity to XAS.

2.1 X-Ray Absorption Spectroscopy

X-ray absorption spectroscopy (XAS) is a common experimental method for studying electronic structure. At its simplest, it is the study of the most intuitive channel of interaction between light and matter: how a beam of photons is absorbed when passing through a collection of atoms. However, by developing a thorough understanding of the subtle intricacies involved in this quantum mechanical process, XAS continues to provide a wealth of

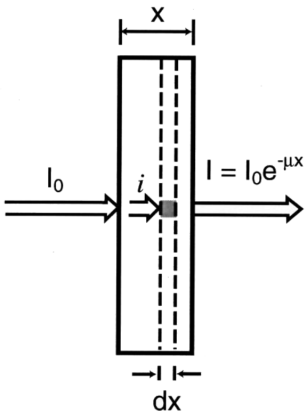

Figure 2.1: The process of x-ray absorption demonstrating the exponential attenuation of the incident beam I_0 governed by absorption coefficient μ. (Figure adapted from Ref.82.)

information to physicists and the wider scientific community. While long-established techniques like extended x-ray absorption fine structure (EXAFS)[77,78] and other nonresonant studies remain a powerful tool for the characterization of structure and composition, we shall focus our discussion on the x-ray absorption near-edge structure (XANES), which examines the absorption profile in the close vicinity around atomic resonances and directly reflects the local electronic structure and bonding environment. We begin this section with a semiclassical review of absorption and the basic equations that govern its spectra, followed by a discussion of some of the subtle points surrounding more robust quantum mechanical descriptions and resonant effects. For a more thorough overview of XAS, we direct the reader to Refs. 79–81.

2.1.1 The Absorption Coefficient

The process that governs the absorption of a photon by an atom is quantum mechanical and therefore probabilistic. Thus, if an x-ray beam of intensity I is shone through a crystal, the amount of light absorbed from the beam will be proportional to I. More precisely, for an infinitesimal sample of thickness $\mathrm{d}x$, we can write

$$\frac{\mathrm{d}I(x)}{\mathrm{d}x} = -\mu I(x) \tag{2.1}$$

where the proportionality factor μ is known as the absorption coefficient. Integrating this equation over a finite sample, and defining our initial beam intensity as I_0, we find the

solution

$$I(x) = I_0 e^{-\mu x} \tag{2.2}$$

known as Beer's Law,[83] which clearly describes an exponential attenuation with distance travelled into the sample. Note that μ is a material-specific property, and in general it can be anisotropic such that it changes with the direction and polarization of the photon beam.

While Equation 2.2 provides a nice summary of the evolution of an x-ray beam, it does not provide any hints to the processes that give rise to the absorption, how μ can be calculated, or any consequential effects to the crystal. For these, we must turn to microscopic theories of the crystal's electronic structure, of which the one-electron model provides a good starting point to visualize the process.

2.1.2 The One-Electron Model

Depicted in Figure 2.2, the one-electron model is a semi-classical theory of photoelectric absorption.[82,84,85] An atom in the material exists initially in an unexcited ground state with electrons possessing energies $\mathcal{E}_k$ until an incident photon of energy $\hbar\omega$ promotes one of the electrons into a previously-unoccupied state above the Fermi energy, ε_F. If $\hbar\omega + \mathcal{E}_k$ is greater than the vacuum energy $\mathcal{E}_{\text{vac}}$, the electron will enter an unbound, continuum state and have the chance to escape the material, with the likelihood of it doing so without reabsorption decreasing exponentially with its starting distance from the surface. If $\hbar\omega + \mathcal{E}_k < \mathcal{E}_{\text{vac}}$, the electron will instead reside in a bound state with energy $\mathcal{E}_{k'}$.

Of course not all energies below ε_F correspond to an electronic state in the material, and the absorption spectrum as a function of photon energy will reflect this. Specifically, as the incident energy is increased from zero, the absorption spectrum will undergo step-like increases at discrete values whenever $\hbar\omega$ becomes sufficiently large so that a transition between two states becomes initially accessible (Figure 2.3); i.e. whenever $\hbar\omega \geq \mathcal{E}_{k'} - \mathcal{E}_k$. This step-up in the observed intensity is known as an absorption edge. For x-ray studies, $\hbar\omega$ is much greater than the span of unoccupied states $\mathcal{E}_{\text{vac}} - \varepsilon_F$, which implies that the initial states must be deeply-bounded core states: atomic-like orbitals bound tightly around the element's nucleus and existing at discrete energies. Therefore, the absorption spectrum will materialize as a sequence of edges whose locations are dictated by the binding energy of the core states, and each edge will be superimposed with a fine-structure of resonances (the XANES spectrum) that reflect the energy-dependence of the unoccupied states. In other words, the spectrum will be smooth except when $\hbar\omega \approx \mathcal{E}_k$ for core states, k, where it

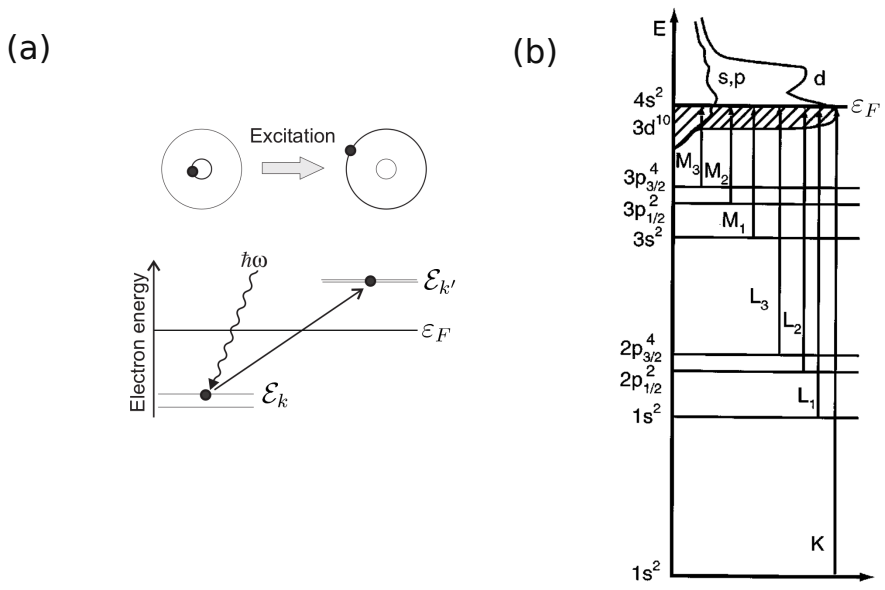

Figure 2.2: Schematic diagram of the semi-classical x-ray absorption process. (a) An incident photon is absorbed by a core electron, promoting it to a higher-energy orbital above the Fermi level. (b) While increasing incident photon energy, edges occur whenever the photon has just enough energy to excite a new core electron into the lowest-energy unoccupied state. Transitions into higher unoccupied states are also allowed. (Figure adapted from Refs. 84 and 86.)

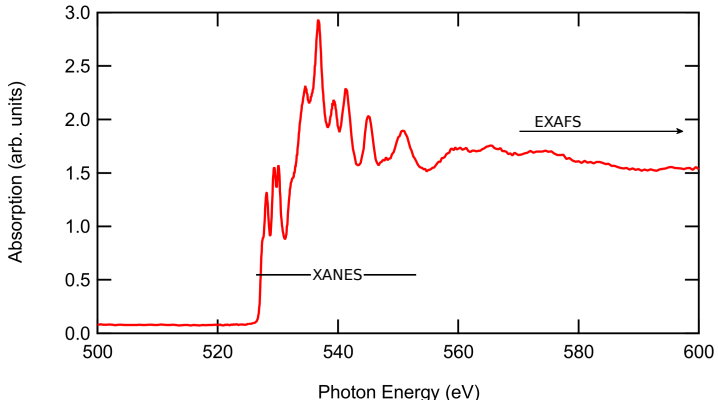

Figure 2.3: Example XAS spectrum of the O K-edge in $YBa_2Cu_3O_{6.335}$. Notice the step increase around 536 eV indicating the location of the absorption edge. The dramatic modulations surrounding the edge-step are due to the projection of the density of unoccupied states (XANES), followed at higher-energies by interference oscillations from scattering off nearby atoms (EXAFS).

will show a steep rise and fine-structure modulations reflecting the available states between ε_F and $\mathcal{E}_{\text{vac}}$.

This behaviour is reflected by the Sommerfeld notation used to label edges, which was developed alongside early experimental observations.[83] Here, each absorption edge is identified by the core state from which it is excited by mapping its atomic-like principle quantum number to a letter ($n = 1, 2, 3 \ldots \rightarrow K, L, M \ldots$), as well as a numeric subscript, if necessary, that corresponds to the edge's rank in descending binding energy for states with that n. For example, an excitation out of the $1s$ core state gives rise to the K edge, $2s$ to the L_1 edge, $2p_{1/2}$ and $2p_{3/2}$ to the L_2 and L_3 edges, respectively, and so on.

2.1.3 Fluorescence and Electron Yield Techniques

After a short time period, the excited electron will decay, and the system will return to the ground state, most likely with the excited electron falling back into the hole that its absence created. If it does so in a single transition, the process is said to be elastic, and the energy will be released via the emission of a new photon, again with energy $\hbar\omega$, or be donated to a second electron that, if it starts in a valence state near ε_F, may enter a high-energy continuum state and escape the material with substantial kinetic energy (an Auger process). The energy may also be released through multiple steps that can see the generation of one or more photons, ejected electrons, and/or phonons in the material,

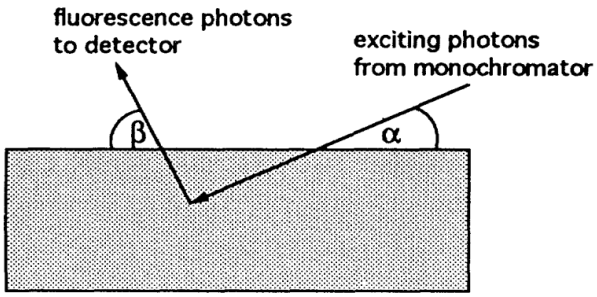

Figure 2.4: The geometry of the TFY measurement technique used in soft x-ray XAS. If the emitted particle is an electron instead of a photon, it contributes to the TEY signal. (Figure adapted from Ref. 87.)

each with energy $< \hbar\omega$, and the process is then classified as inelastic. These by-product processes, elastic or inelastic, are exploited when measuring absorption edges in the soft x-ray regime (less than ~ 2000 eV). Since the photon attenuation length at those energies is on the order of a couple of microns, it is impractical to prepare samples sufficiently thin for transmission studies where the beam is measured directly after passing through the sample. Instead, the photons and electrons that are back-emitted from the same surface as the beam enters are measured.[1] This is relevant to the cuprates, for example, whose O K-edge (~ 535 eV) and Cu L-edge (~ 930 eV) probe the superconducting charge carriers in the CuO_2 planes.

In the subsequent chapters, fluorescence yield (FY) and electron yield (EY) techniques are employed where the rate at which photons and electrons, respectively, are emitted from a sample are counted as a function of incident photon energy.[81,88] Specifically, we employ "total" yield techniques because all emitted particles, irrespective of their energy, are recorded and counted. In "partial" yield techniques, which are also commonly employed, the energy of the detected particles are discriminated to provide an additional dimension of analysis. When normalized to the incident beam intensity, all of these measurements should produce a spectrum that is proportional to the absorption coefficient $\mu(\hbar\omega_{\text{incident}}, \hbar\omega_{\text{measured}})$.[89,90] The details, approximations, and experimental considerations that underline that assertion are deep subjects that can (and do) constitute entire textbooks, and we must omit them from this dissertation. However, to appreciate the results

[1] For the fluorescence process, photons are emitted in all directions fairly uniformly due to their small momentum relative to the electronic states. For electron emission, the current depends on the crystal momentum state, $\vec{k}$, from which they originated. The angular distribution can therefore reveal a substantial amount of additional information about the material's electronic structure, as is commonly exploited in angle-resolved photoemission (ARPES).[85]

presented later, the reader should be aware of a few key facts surrounding TEY and TFY. First, TEY is highly surface-sensitive, as the penetration depth—which determines the depth of the measurement—of electrons produced with soft x-rays are on the order of nanometers.[85,88] Furthermore, TEY requires samples with sufficiently high conduction to avoid the build-up of positive charge on the surface as electrons are removed that can distort the results with unusual backgrounds. TFY, on the other hand, is considered representative of the bulk and is accurate for both conducting and insulating materials, but it suffers from self-absorption effects.[1,87] Essentially, the measurement geometry and sharp variations in μ around absorption edges can destroy the proportionality of the measurement and cause peaks in the spectra to appear compressed in an effect known as saturation. Specifically, the spectrum follows the relation:[2]

$$\frac{I^{(\text{measured})}}{I_0} \propto \sum_{\lambda} \frac{\mu_\lambda(\mathcal{E}_i)}{\mu_{\text{tot}}(\mathcal{E}_i) + \mu_{\text{tot}}(\mathcal{E}_f)g} \tag{2.3}$$

where $\mathcal{E}_i$ and $\mathcal{E}_f$ are the incident and measured photon energy, respectively, λ denotes the contribution of the absorption coefficient from a particular $\mathcal{E}_k \to \mathcal{E}_{k'}$ transition (say, the K-edge), μ_{tot} is the total absorption coefficient, and

$$g = \frac{\sin\alpha}{\sin\beta} \tag{2.4}$$

is a geometric function that depends on the angles α and β between the sample surface and the incident and emitted beams, respectively. The choice of the experimental geometry, g, will therefore have a strong influence on the height of the absorption peak. For example, a small g that corresponds to grazing-incidence/normal-emission implies that $I/I_0 \sim \mu_\lambda(\mathcal{E}_i)/\mu_{\text{tot}}(\mathcal{E}_i)$, and conversely a large g that corresponds to normal-incidence/grazing-emission gives $I/I_0 \sim \mu_\lambda(\mathcal{E}_i)/\mu_{\text{tot}}(\mathcal{E}_f)$. Furthermore, the chemistry of the sample is also important since μ_{tot} is a function of the absorption coefficients of every species in the sample, including μ_λ. In some scenarios, then, such as a small g and a high-concentration of the resonating species ($\mu_{\text{tot}} \sim \mu_\lambda$), the height of the absorption peak can be substantially reduced, and care must be taken if an accurate intensity measurement is required. (For further discussion, we direct the reader to Refs. 79, 81, 91.)

[1] TEY also experiences self-absorption effects, but that is rarely considered its most important drawback.

[2] Assuming an infinitely thick sample.

2.1.4 The Configuration Picture

The one-electron model is often repeated in the literature due to the ease with which it can be visualized, but it leaves out some important subtleties that can have significant effects on real scattering measurements. An important example is that the electron is imagined to be moving up and down the atomic energy levels while the rest of the atom remains static. In reality, the other electrons will of course adjust to the change, and in particular they will relax around the newly created core hole. It is more accurate to consider the process within the context of the configuration picture, where all of the orbitals are described collectively by a multi-electron wavefuction (see Ref. 92). The effect of absorbing a photon must then be imagined as changing the configuration of electrons from a ground state into some excited, higher-energy configuration. The choice of basis set with which to build the wavefunction such that it is accurate but also calculable within the limits of modern computing is an active subject of research, but often it resembles a set of hydrogen-like atomic orbitals. Thus, some versions of the configuration technique are known as a linear combination of atomic orbitals (LCAO) method. For strongly bonded atoms, an LCAO method can be built from a basis set that spans many atoms, and thus it can capture itinerant character of the electronic states and how interactions across bonds are affected by the absorption of a photon.

It is important to note here that the nature of an LCAO orbital can be substantially different than the hydrogen-like orbitals from which it is constructed. Despite this, the convention in physics is to identify each orbital and configuration by its atomic approximation. For example, valence electrons around a Cu atom in the CuO_2 planes of a high-T_c superconductor are said to be in $3d$ orbitals. This nomenclature quickly communicates important information about the orbital's symmetry and approximate binding energy, but it hides other information such as the degree to which it hybridizes with neighbouring O $2p$ orbitals and delocalizes throughout the crystal. For the core orbitals that the unexcited electrons start in, however, they are so tightly bound to the nucleus that they mimic hydrogen-like orbitals far more closely, and the improvements provided from calculating a proper LCAO orbital are modest at best. Thus, overall the reader is cautioned to appreciate the convenience of this shorthand, but also to avoid an over-interpretation of what it conveys.

A quick example can be helpful in elucidating the usefulness of the configuration picture for more than just quantitative adjustments. In an x-ray absorption experiment of the L-edge in a $3d$ transition metal, the one-electron picture shows a $2p$ electron being promoted to an empty $3d$ orbital (Figure 2.2). A $2p$ orbital has $\ell = 1$ angular momentum, and the electron has $s = 1/2$ spin, which results in a total angular momentum of either $j = 1/2$ or

$j = 3/2$. The final state has $\ell = 1$ and $s = 1/2$, which means $j = 3/2$ or $j = 5/2$. Thus, due to modest energy splitting between momentum states in each orbital, four L-edge resonant peaks should appear. The spin-orbit coupling for the $2p$ states is roughly 15 eV, which creates two well-separated peaks L_2 and L_3, and for the $3d$ states it is about 50 meV, which slightly separates each of the L_2 and L_3 peaks into narrow doublets.[84] Indeed, this is what is seen in experiment, however there is conceptually a critical problem. The initially full $2p$ shell has no net orbital momentum and thus does not experience spin-orbit coupling. The situation must be reconsidered in the configuration picture, where it is specified as $2p^6 3d^n \rightarrow 2p^5 3d^{n+1}$ to indicate the partially-filled and active orbitals. The final state has a multi-electron wavefunction with an additional electron in the $3d$-like shell and one hole in the $2p$-like shell. Both the excited electron and the hole will experience spin-orbit coupling in their respective bands, and that leads to the 4 possible absorption resonances seen in experiment. Thus, this is a typical example of how the one-electron picture is used as an easy way to visualize the transition and as a guide to the correct qualitative results, but the configuration picture is required for a robust explanation of the physics and for more-accurate quantitative predictions.

2.1.5 A Quantum Treatment of Absorption

We now depart from our qualitative overview of the absorption process to delve into a quantitative theory that can be used to calculate spectra quantitatively. Influenced by an incident photon beam, the probability per unit time that an electron will undergo a transition from an initial state $|i\rangle$ with energy $\mathcal{E}_i$ to a final state $|f\rangle$ with energy $\mathcal{E}_f$ is given by Fermi's Golden Rule[81,93]

$$T_{if}^{(\mathrm{abs})} = \frac{2\pi}{\hbar} \left|\langle f|H_{\mathrm{int}}|i\rangle\right|^2 \delta(\mathcal{E}_i - \mathcal{E}_f)\rho(\mathcal{E}_f) \tag{2.5}$$

where H_{int} is the interaction Hamiltonian, $\rho(\mathcal{E}_f)$ is the density of states per unit energy of the final wavefunction, and energy conservation is enforced by the presence of the Dirac delta function. Note that the states to which we refer are all-encompassing in the sense that they contain the photon and the entire atom.

To calculate $T_{if}^{(\mathrm{abs})}$, we examine the form of the interaction Hamiltonian in Equation 2.5,[1] given by[84,94]

$$H_{\mathrm{int}} = \sum_i \left(\frac{e}{m_e c} \boldsymbol{p}_i \cdot \boldsymbol{A}(\boldsymbol{r}_i, t) + \frac{e^2}{2m_e c^2} \boldsymbol{A}(\boldsymbol{r}_i, t) \cdot \boldsymbol{A}(\boldsymbol{r}_i, t) \right) \tag{2.6}$$

[1] Scattering from the nucleus is negligible.

where $\boldsymbol{p}_i$ and $\boldsymbol{A}(\boldsymbol{r}_i, t)$ are the momentum and vector potential operators, respectively, and the sum is over each electron, i. Note that relativistic terms in Equation 2.6, which govern the spin interaction, have been omitted since their magnitude scales as $\hbar\omega/mc^2$, which is negligibly small for soft x-rays.[94] With the electromagnetic field in quantized notation, we have

$$\boldsymbol{A}(\boldsymbol{r}, t) = A_0 \sum_{j,\boldsymbol{k}} \frac{1}{\sqrt{k}} \epsilon_j \left(a_{k,j}(t) e^{i\boldsymbol{k}\cdot\boldsymbol{r}} + a^\dagger_{k,j}(t) e^{-i\boldsymbol{k}\cdot\boldsymbol{r}} \right) \tag{2.7}$$

where $a^\dagger_{k,j}(t)$ and $a_{k,j}(t)$ are creation and annihilation operators, respectively, of photons with wavevector $\boldsymbol{k}$ and polarization vector $\boldsymbol{\epsilon}$. The prefactor

$$A_0 = \sqrt{\frac{2\pi\hbar c}{V}} \tag{2.8}$$

is a constant where V the volume of the quantization box.

Substitution of Equations 2.6 and 2.7 into Equation 2.5 yields the result of the interaction. However, simplifications can first be made using some physical restraints. The second term in Equation 2.6 is quadratic in $\boldsymbol{A}$ and therefore contains even numbers of annihilation and creation operators. In other words, this term changes the number of photons in the system by 0 or ± 2. The first term, which is linear in annihilation and creation operators, must therefore be responsible for all single-photon absorption and emission events, and we may neglect the second term. We thus find that the absorption process is governed by

$$H^{(\mathrm{abs})}_{\mathrm{int}} = A_0 \frac{e}{m_e c} \sum_{i,j,\vec{k}} \frac{1}{\sqrt{k}} a_{k,j}(t) (\boldsymbol{\epsilon} \cdot \boldsymbol{p}_i) e^{i\boldsymbol{k}\cdot\boldsymbol{r}}. \tag{2.9}$$

The exponential factor can then be expanded in a Taylor series to obtain

$$H^{(\mathrm{abs})}_{\mathrm{int}} = A_0 \frac{e}{m_e c} \sum_{i,j,\boldsymbol{k}} \frac{1}{\sqrt{k}} a_{k,j}(t) \left[(\boldsymbol{\epsilon} \cdot \boldsymbol{p}_i) + i(\boldsymbol{\epsilon} \cdot \boldsymbol{p}_i)(\boldsymbol{k} \cdot \boldsymbol{r}) + \ldots \right]. \tag{2.10}$$

The first term in brackets in Equation 2.10 governs dipole transitions, the second term quadrupole transitions, and so on. With a few notable exceptions,[1] all transitions of interest are dominated by the dipole interaction,[81] and we need only retain the first term. This is known as the dipole approximation, and it is valid when the wavelength of the photon is large compared to the size of the electronic orbitals which it perturbs. Specifically, $r \ll 1/k$, and the electric field vector is approximately constant across the system at any

[1] Pre-edge peaks in the K-edges of $3d$ metals and L-edges of rare earths.[81]

instance of time. For soft x-ray scattering, the wavelengths are of the order ~ 1 nm, and the size of say, an initial-state core $2p$ orbital is on the order of 0.01 nm. So we have an r at least an order of magnitude smaller than $1/k$, and the condition is well satisfied.

We now introduce the absorption cross-section, which is defined as the probability of an interaction event per unit time per unit flux of the incident beam,

$$\sigma^{(\mathrm{abs})} = \frac{T_{if}^{(\mathrm{abs})}}{\Phi_0}. \tag{2.11}$$

Combining Equations 2.5 and 2.10, this leads to[84]

$$\sigma^{(\mathrm{abs})} = 4\pi^2 \alpha_{\mathrm{f}} \hbar\omega |\left\langle f|\boldsymbol{\epsilon}\cdot\boldsymbol{r}|i\right\rangle|^2 \delta(\mathcal{E}_i - \mathcal{E}_f)\rho(\mathcal{E}_f) \tag{2.12}$$

where $\alpha_{\mathrm{f}} \approx 1/137$ is the fine structure constant. The absorption spectrum can be calculated by performing an integral of this cross-section over energy, and we arrive at our final goal:

$$I^{(\mathrm{abs})} = 4\pi^2 \alpha_{\mathrm{f}} \hbar\omega |\left\langle f|\boldsymbol{\epsilon}\cdot\boldsymbol{r}|i\right\rangle|^2. \tag{2.13}$$

Thus, we have a method for calculating the x-ray absorption that explicitly takes into account the electronic properties of the system and the details of the photoabsorption process.

An alternative way to define $\sigma^{(\mathrm{abs})}$ is as the average number of absorbed photons per atom exposed to the beam, normalized to the number of incident photons per unit area. From Equation 2.1, the number of absorbed photons as the beam travels an infinitesimally short distance $\mathrm{d}x$ through the sample is $\mu I(x)$, and so if we denote the number density of atoms in the sample as n, then we have the simple relation

$$\mu = \sigma^{(\mathrm{abs})} n. \tag{2.14}$$

An equivalent method for calculating the absorption is thus given by

$$I^{(\mathrm{abs})} \propto I_0 e^{-\mu x}, \tag{2.15}$$

which becomes an equality in transmission mode.

The amplitude of the matrix element in Equation 2.13 is determined by the degree of overlap between the initial and final quantum states $|i\rangle$ and $|f\rangle$, modulated by $\boldsymbol{\epsilon}\cdot\boldsymbol{r}$. The overlap becomes very strong when the energy of the two states match precisely, i.e. when the photon's energy is exactly the difference between the two orbitals. This condition is called resonance, and it greatly enhances the absorption at that specific energy.

Therefore, an absorption edge is comprised of not just a step increase, as predicted in semi-classical models, but also a sharp peak with a strictly quantum mechanical origin (Figure 2.3). Furthermore, as explained in Section 2.1.2, the fine structure of an XAS spectrum near an absorption edge correlates with the material's unoccupied density of states such that the spectrum will contain a series of resonant peaks that identifies the energies of each unoccupied state, and the largest peak, indicating the nominal position of the edge, corresponds to the energy required to eject electrons into unbound vacuum states.

The photon's energy is not the only tunable parameter that affects the amplitude of the absorption. The orientation of the incident photon is also important, specifically through the polarization dependence of $\boldsymbol{\epsilon} \cdot \boldsymbol{r}$. The unoccupied electronic orbitals can be spatially asymmetric, and in such cases they overlap to a greater or lesser extent with the atom-plus-photon initial state depending on the relative orientation of the eletromagnetic oscillations of the photon. Basically, if the photon's polarization is parallel to an antinode of the unoccupied state, then the oscillations couple well to that final state and increase the strength of the excitation. If it is parallel to a node, however, then the coupling is weak. Therefore, resonant XAS spectra are, in general, polarization-dependent. This sets resonant studies apart from nonresonant, where the intensities of absorption spectra are determined only by the step-increases at absorption edges and are independent of polarization.

Finally, we should also note that the well-known dipole selection rules apply to these transitions.[81,84,85] Specifically, resonant peaks occur only if the transition between the initial and final states ensures that the change in orbital angular momentum $\Delta\ell = \pm 1$, change in magnetic quantum number $\Delta m_\ell = 0, \pm 1$, and the change in spin $\Delta m_s = 0$.

2.2 X-Ray Diffraction

When a collimated beam of x-rays interacts with the periodic lattice of a crystal, the beam will diffract and experience constructive interference along discrete directions determined by the well-known Bragg's law[22,95]

$$2d \sin\theta = n\lambda \tag{2.16}$$

where d is the distance between atomic planes, θ is the angle the atomic planes make with the incident beam, λ is the beam's wavelength, and n is a positive integer indicating the order of the diffraction. Of course, this is equivalent to the Laue condition

$$e^{i(\vec{k}-\vec{k}')\cdot\vec{R}} = 1 \tag{2.17}$$

where $\vec{k} = 2\pi/\lambda$ is the incident beam's wavevector, $\vec{k}'$ is the wavevector of the emitted beam, and $\vec{R}$ is any vector in the crystal's Bravais lattice.

These elementary forumlae predict the location of Bragg peaks in a crystal's reciprocal space, but they say nothing about the intensity and shape of such peaks. In fact, they assume a measurement of infinitely large, perfectly aligned crystals at zero temperature made up of atoms that behave like point scatterers, and thus they predict peaks that are infinitely sharp and bright. To understand the real profiles of diffraction peaks measured in experiment, the convention is to begin with the intuitively constructed formula[96]

$$I = I_0 n \Delta\Omega \left(\frac{d\sigma}{d\Omega} \right) \tag{2.18}$$

where I_0 is the intensity of the incident beam, n is the number of scatters (usually the number of unit cells) per unit area, $\Delta\Omega$ is the solid angle subtended by the detector, and the last term, $d\sigma/d\Omega$, is the modulation of the efficiency at which a crystal scatters the beam toward the detector. This quantity is called the differential cross-section, and it is defined as the intensity of the scattered beam as a function of angle, normalized to the power per unit area of the incident beam (i.e. normalized to the incident beam's irradiance). The interesting physics of the material are found in this final term alone, and the others, which are particular to the setup of each individual experiment, are typically normalized out or otherwise ignored when the data is analyzed. To understand the results of a scattering experiment, then, is to effectively understand the nature of the differential cross-section, and we do so by exploring its origin in the following sections.

2.2.1 Scattering from Electrons

The expression for the differential cross-section can be derived from a simple model of atoms in a crystal exposed to an x-ray beam. To begin, we briefly review the classical description of scattering off a single electron and how that model can be extended to many electrons.

The incident x-ray beam can be described as an electromagnetic field of the form

$$\vec{E}(\vec{r}, t) = \vec{\epsilon}\, E_0 e^{-i(\omega t - \vec{k}\cdot\vec{r})} \tag{2.19}$$

where $\vec{\epsilon}$ is a unit vector pointing along the direction of polarization. This field causes the electron to oscillate along $\vec{\epsilon}$ at frequency ω, at which point it will then emit another

electromagnetic wave of its own, given by[197]

$$\vec{E}'(\vec{r}', t) = -\frac{e^2}{4\pi\epsilon_0 m_e c^2} \frac{e^{ik'r'}}{r'} \left(\vec{k}' \times \vec{E}(t)\right) \times \vec{k}' \tag{2.20}$$

where the " $'$ " indicates emission, $\vec{p}(t)$ is the electron's dipole moment, and $\vec{E}(t)$ is evaluated at the location of the electron. From here, it is conventional to define the scattering length and its square, the scattering area. In the classical picture of particles bouncing off one another like billiard balls, the introduction of these quantities makes intuitive sense. Though that's less the case for the modern picture, they persist in the formalism for their mathematical convenience. For our purposes, the scattering length is defined as

$$f(\vec{\epsilon}, \vec{\epsilon}') = -\frac{re^{-i\vec{k}'\cdot\vec{r}}}{E} \vec{E}' \cdot \vec{\epsilon}', \tag{2.21}$$

and the differential cross-section is defined as the scattering area,

$$\left(\frac{d\sigma}{d\Omega}\right) = |f(\vec{\epsilon}, \vec{\epsilon}')|^2. \tag{2.22}$$

Note that if the incident wave takes the form $e^{i\vec{k}\cdot\vec{r}}$, then the scattered wave is $\propto f e^{i\vec{k}\cdot\vec{r}}$.[94]

For the case of scattering from a single-electron, we find

$$f_{1e}(\vec{\epsilon}, \vec{\epsilon}') = r_0 \, \vec{\epsilon} \cdot \vec{\epsilon}', \tag{2.23}$$

and

$$\left(\frac{d\sigma}{d\Omega}\right)_{1e} \propto r_0^2, \tag{2.24}$$

where $r_0 = e^2/4\pi\epsilon_0 m_e c^2$ is the classical electron radius, also referred to as the Thomson scattering length.

For a system with multiple electrons, the elementary rules of Bragg diffraction apply; the emitted waves from each electron will superimpose, with the constructive or destructive nature of that superposition determined according to their relative phases. The phase, in turn, is calculated from the difference in each wave's path-length and the π phase shift[2]

[1] Note that a complete treatment should also include a term in Equation 2.20 from spin scattering by the magnetic field of the incident wave. However, it can be shown[84] that the this effect is only about 0.1% as large as the intensity from charge scattering at the soft x-ray energies of interest here, and it is safe to neglect.

[2] Note the minus sign in Equation 2.20.

imparted at the scattering event. The effect on the final intensity of the scattered beam at the detector is accounted for by the introduction of a form factor given by

$$F(\vec{Q}) = \sum_i e^{i\vec{Q}\cdot\vec{r}_i}, \tag{2.25}$$

where $\vec{Q} = \vec{k} - \vec{k}\,'$ is the momentum transfer of the scattering event, and $\vec{r}_i$ is the location of electron i. $F(\vec{Q})$ can be interpreted as the unitless Fourier transform of the electronic positions, and thus it encodes the local geometric structure.

The scattering length for this system then becomes

$$f = r_0\, \vec{\epsilon}\cdot\vec{\epsilon}\,' F(\vec{Q}), \tag{2.26}$$

and the differential cross-section becomes

$$\left(\frac{d\sigma}{d\Omega}\right) = r_0^2\, |\vec{\epsilon}\cdot\vec{\epsilon}\,'|^2 |F(\vec{Q})|^2, \tag{2.27}$$

which is the general form for these quantities in all systems for non-resonant scattering processes.

2.2.2 Scattering from an Atom

These basic concepts can now be extended to model scattering from an atom. Implicit in our free-electron model was that the electrons exist at single points in space, but electrons around an atom of course exist in spatially distributed wavefunctions. We thus modify Equation 2.25 as follows:[22,84,95]

$$F(\vec{Q}) = -\frac{1}{e}\int \rho(\vec{r}) e^{i\vec{Q}\cdot\vec{r}}\, dr \tag{2.28}$$

where $\rho(\vec{r})$ is the charge density of the electrons around the atom. This equation applies when dealing with either a classical electrostatic density or a quantum probability wavefunction for $\rho(\vec{r})$, and inserting this form factor into Equations 2.18 and 2.27 immediately generates the scattering intensity.[1]

[1] Note that although photons scatter off any charge density they encounter, scattering from the nucleus can be neglected. For x-ray energies, the heavy nucleus doesn't oscillate appreciably in the short time that it interacts with the photon's electromagnetic field, and thus any added intensity to the detected signal from nuclear scattering is negligibly weak.

Clearly, Equation 2.28 is simply the continuous version of the discrete Equation 2.25, and the case of discrete electrons can still be accounted for simply by choosing an appropriate form of $\rho(\vec{r})$:

$$\rho(\vec{r}) = \delta(\vec{r} - \vec{r}_i) \tag{2.29}$$

where $\delta(\vec{r} - \vec{r}_i)$ is the Dirac delta function that is nonzero at the electron positions $\vec{r}_i$.

It is the intent of this section to provide a simple and general explanation for the origin of the atomic form factor, for which Equation 2.28 fits the bill. However, the reader should be aware that calculating an accurate $F(\vec{Q})$ can often be a complicated problem of quantum chemistry, as the nature of the atomic orbitals—particularly for materials with strong electronic correlations such as the high-T_c superconductors—may only be known with modest precision. Luckily, the results of an x-ray scattering experiment, even for the case of resonant scattering (see Section 2.3), rarely requires such an in-depth knowledge. Instead, as will be explained later, only the underlying symmetry of the form factor (and thus the differential cross-section) may be of interest, and for that we need only begin with a solid understanding of the physical meaning of these quantities, which Equation 2.28 provides.

2.2.3 Scattering from a Lattice

Extending our model larger again, we now consider scattering from a collection of atoms. Like the case of multiple electrons, we consider our atoms to be point scatterers arranged at positions $\vec{r}_i$. The complications and subtleties of the wave-like nature of the atomic orbitals are safely contained in Equation 2.28, and we lose nothing by ignoring them at this stage.

In analogy to Equation 2.25, we can thus write our form factor as

$$S(\vec{Q}) = \sum_i F_i(\vec{Q}) e^{i\vec{Q}\cdot\vec{r}_i}. \tag{2.30}$$

The exponential factor in the sum is identical to what is seen in Equation 2.25 and accounts for the interference due to the atoms' relative positions. The prefactor $F_i(\vec{Q})$ is newly introduced, and it effectively weights the sum with atomic form factors. In so doing, the additional interference effects from the local distribution of charge around each atom is taken into account.

The choice of "collection" of atoms from the material under investigation can take any form and usually depends on convention. When studying crystal media, it is most often

taken to be the crystal's unit cell. To determine I in Equation 2.18, another form factor must then be employed to account for the relative positions of the unit cells and their effect on the interference pattern,

$$S^{(2)}(\vec{Q}) = \sum_j \vec{S}(\vec{Q}) e^{i\vec{Q}\cdot\vec{R}_j}. \tag{2.31}$$

If more structure exists in the material, additional form factors can again be employed—*ad infinitum*—until the entire sample, or at least the entirety of the x-ray beam spot, is taken into account. The modularity of this mathematical framework is thus apparent: The intensity of scattering from a fundamental element, the electron,[1] must be calculated. But thereafter, the addition of only a simple geometrical form factor is required to calculate the scattering from the local structure, and then another factor for the wider structure, etc., until the scattering is calculated for the material as a whole. Additionally, since the scattering from a single electron is the same regardless of the material under study, the unique physics of the material must be entirely contained within these form factors. Discovering the nature of these factors is therefore the ultimate objective of a scattering experiment.

In practice few form factors are needed to fully describe a crystal, and a distinction in terminology is made between two important "levels" of form factors based on what one can learn from each: the atomic form factor, $\vec{F}(\vec{Q})$; and the wider-structure-related form factors, $\vec{S}(\vec{Q})$, collectively referred to as just the structure factor. A natural delineation exists between the two categories, with the atomic form factor being more complicated to calculate and directly determined by the element and bonding environment of each atom, and the structure factor being more simple to calculate and containing only geometrical information about the crystal's lattice. The level of structure—unit cell, lattice, etc.—being considered when discussing the structure factor is usually made clear through context, or often it is unimportant and left ambiguous to simply imply the effects of the atomic positions while neglecting the subtleties of the electronic orbitals.

Finally, we note that to calculate the scattered intensity in a lattice, the form factor $F(\vec{Q})$ in Equations 2.26 and 2.27 is simply replaced with the structure factor $S(\vec{Q})$.

2.3 Resonant X-Ray Scattering

The process of scattering with the energy of the incident beam tuned to an x-ray absorption edge of the material is known as resonant x-ray scattering (RXS). Unlike the process

[1] Or more precisely, an infinitesimal element of electric charge.

described in the previous section, scattering on resonance involves the virtual absorption of the diffracting photon. The process is inherently quantum mechanical in origin, and although the classical quantities derived previously will continue to be used to characterize the intensity of a diffraction peak, their origins must be redefined in a quantum context.

2.3.1 A Quantum Treatment of Scattering

Being a quantum mechanical process involving the absorption of a photon, we begin our description of resonant scattering at the same point as we did for x-ray absorption. However, we must note that Fermi's Golden Rule (Equation 2.5) is the result of solving Schrödinger's Equation with a time-dependent perturbation up to first order. While that is sufficient for describing XAS, resonant scattering requires terms up to second order be kept. We thus find that the probability per unit time that an electron will interact with a photon and transition from an initial state $|i\rangle$ to a final state $|f\rangle$ is given by[93,98]

$$T_{if} = \frac{2\pi}{\hbar}\left|\langle f|H_{\text{int}}|i\rangle + \sum_n \frac{\langle f|H_{\text{int}}|n\rangle\langle n|H_{\text{int}}|i\rangle}{\mathcal{E}_i - \mathcal{E}_n}\right|^2 \delta(\mathcal{E}_i - \mathcal{E}_f)\rho(\mathcal{E}_f) \tag{2.32}$$

where H_{int} is the interaction Hamiltonian and $\rho(\mathcal{E}_f)$ is the density of states per unit energy of the final wavefunction. The sum is over all possible states $|n\rangle$, including "virtual" states that would break energy conservation. However, the conservation of energy is ultimately preserved by the presence of the Dirac delta function. The first term in the sum represents a direct transition between states and is known as a first-order process, while the second term involves the occupation of many intermediate states and is known as a second-order process. We proceed with the same interaction Hamiltonian, repeated here from Equation 2.6,

$$H_{\text{int}} = \sum_i \left(\frac{e}{m_e c}\boldsymbol{p}_i \cdot \boldsymbol{A}(\boldsymbol{r}_i, t) + \frac{e^2}{2m_e c^2}\boldsymbol{A}(\boldsymbol{r}_i, t)\cdot\boldsymbol{A}(\boldsymbol{r}_i, t)\right) \tag{2.33}$$

where we again have

$$\boldsymbol{A}(\boldsymbol{r}, t) = \sqrt{\frac{2\pi\hbar c}{V}}\sum_{j,\boldsymbol{k}}\frac{1}{\sqrt{k}}\epsilon_j\left(a_{k,j}(t)e^{i\boldsymbol{k}\cdot\boldsymbol{r}} + a^\dagger_{k,j}(t)e^{-i\boldsymbol{k}\cdot\boldsymbol{r}}\right), \tag{2.34}$$

and solve with perturbation theory.

Like the case of XAS, we can first simplify our system with some physical arguments. For a scattering process, we seek to have the same number of photons before and after the

interaction. Therefore, we need only consider terms with equal numbers of $a^\dagger$ and a. All other terms involve net x-ray absorption or emission. To first order in H_{int}, the $\boldsymbol{p}\cdot\boldsymbol{A}$ term is singular in $a^\dagger$ and a and thus does not contribute to scattering. The $\boldsymbol{A}\cdot\boldsymbol{A}$ term, however, is quadratic in $a^\dagger$ and a, with some of its consituent terms creating and annihilating equal numbers of photons. Thus, we get a $\langle f|H_{\text{int}}|i\rangle \sim \langle f|\boldsymbol{A}\cdot\boldsymbol{A}|i\rangle$-like interaction contributing to the scattering signal. In addition, terms of second-order in H_{int} are found to be comparable in magnitude to first-order terms[94] and should also be considered. At this level, $\boldsymbol{p}\cdot\boldsymbol{A}$ dominates and some of the terms from its square preserve photon numbers. Therefore, a $\langle f|H_{\text{int}}|n\rangle\langle n|H_{\text{int}}|i\rangle \sim \langle f|(\boldsymbol{p}\cdot\boldsymbol{A})^\dagger|n\rangle\langle n|\boldsymbol{p}\cdot\boldsymbol{A}|i\rangle$-like interaction must also be included in the scattered signal. This second set of terms are of the form[84,96,99–101]

$$M^{(2)} \sim \langle\psi_1|\,\boldsymbol{p}\cdot\boldsymbol{\epsilon}\,e^{i\boldsymbol{k}\cdot\boldsymbol{r}}\,|\psi_2\rangle\,. \tag{2.35}$$

We can now expand $e^{i\boldsymbol{k}\cdot\boldsymbol{r}}$ and once again employ the dipole approximation to get

$$\begin{aligned}\langle\psi_1|\,\boldsymbol{p}\cdot\boldsymbol{\epsilon}\,e^{i\boldsymbol{k}\cdot\boldsymbol{r}}\,|\psi_2\rangle &= \langle\psi_1|\,\boldsymbol{p}\cdot\epsilon\,(1+i\boldsymbol{k}\cdot\boldsymbol{r}+\ldots)|\psi_2\rangle &(2.36)\\ &\simeq \langle\psi_1|\,\boldsymbol{p}\cdot\boldsymbol{\epsilon}\,|\psi_2\rangle &(2.37)\\ &= im_e\omega\,\langle\psi_1|\,\boldsymbol{r}\cdot\boldsymbol{\epsilon}\,|\psi_2\rangle\,. &(2.38)\end{aligned}$$

Putting this all together, we find a differential cross-section (for only the scattering channel of interactions)[94]

$$\left(\frac{d\sigma}{d\Omega}\right)_S = r_0^2\left|\vec{\epsilon}\cdot\vec{\epsilon}\,'\,\langle\psi|F(\vec{Q})|\psi\rangle + \sum_n \frac{\langle\psi|(\vec{\epsilon}\,'\cdot\sum_j \boldsymbol{p}_j)^\dagger|n\rangle\,\langle n|\vec{\epsilon}\cdot\sum_j \boldsymbol{p}_j|\psi\rangle}{\hbar\omega-(\mathcal{E}_n-\mathcal{E}_i)+\frac{i}{2}\Delta_n}\right|^2 \tag{2.39}$$

where Δ_n is the full-width at half-maximum of the distribution of the $|n\rangle$ states' energies, equivalent to the lifetime of $|n\rangle$; state $|i\rangle$ and $|f\rangle$ have been replaced with $|\psi\rangle$ to indicate that the scattering ultimately leaves the electron's state unchanged; and the sum over j includes every electron. Clearly, the first term is just the nonresonant scattering differential cross-section obtained in Equation 2.27, and the second term is the modification due to resonance.

By definition, recall that the square of the scattering length gives the differential cross-section (Equation 2.22), and thus Equation 2.39 can be arranged to take the form

$$\left(\frac{d\sigma}{d\Omega}\right)_S = |f+f^R|^2 \tag{2.40}$$

where f is the nonresonant scattering length from Equation 2.26 and f^R is the resonant scattering length just derived. Thus, the effect of scattering at an energy close to resonance

is simply to add an energy-dependent correction to the scattering length. Furthermore, the effect of the resonance increases a typical scattering intensity by roughly four orders of magnitude,[84] and we can make the approximation[1]

$$\left(\frac{d\sigma}{d\Omega}\right)_S^R \approx |f^R|^2 + \Delta_{f^R}. \tag{2.41}$$

Therefore, on resonance, the measured intensity of a diffraction peak approximates to the scattering due solely to the resonant scattering length, plus a small, slowly-varying background intensity that comes from nonresonant processes.

It is recognized in the literature[8,9,94] that the resonant term in Equation 2.39 behaves such that we can write

$$f^R \sim \boldsymbol{\epsilon}'^{\dagger} \cdot \hat{\mathcal{M}} \cdot \boldsymbol{\epsilon}. \tag{2.42}$$

We exploit the matrix formalism of quantum mechanics here—the typical choice when calculating real diffraction intensities—so that we have $\boldsymbol{\epsilon}$ being a unit 3-vector representing the incident polarization, $\boldsymbol{\epsilon}'^{\dagger}$ a covector of the emitted polarization, and $\hat{\mathcal{M}}$ a 3×3 tensor. Adopting this approximation, it is then clear that the resonant scattering length can be written akin to that of nonresonant scattering by defining a resonant structure factor tensor $\hat{S}(\vec{Q}) \propto \hat{\mathcal{M}}$. And then finally, we get

$$\left(\frac{d\sigma}{d\Omega}\right)_S^R \sim \left|\boldsymbol{\epsilon}'^{\dagger} \cdot \hat{S}(\vec{Q}) \cdot \boldsymbol{\epsilon}\right|^2, \tag{2.43}$$

which closely approximates the resonant contribution to the intensity of a scattering peak.

We finish our discussion with a final note. In the one-electron method of Section 2.1.2, the implied chronological progression of the photoabsorption process—where (1) the photon is absorbed and the electron is promoted, followed by (2) the electron decays back down, sometimes releasing another photon—is too simple to account for all of the nuances of the quantum process, though it indeed can be helpful for conceptual understanding. Resonant scattering, for example, is thought of as a one-step process of a photon instantaneously diffracting off the atom upon encountering it. The combined photon/multi-electron

[1] The resonant differential cross-section is also commonly written as[84,94]

$$\left(\frac{d\sigma}{d\Omega}\right)_S^R = \frac{\alpha_f^2 \hbar^2 \omega^4}{c^2} \left| \sum_n \frac{\langle i| \boldsymbol{r} \cdot \boldsymbol{\epsilon}_f^{\star} |n\rangle \langle n| \boldsymbol{r} \cdot \boldsymbol{\epsilon}_i |i\rangle}{\hbar\omega - (\mathcal{E}_n - \mathcal{E}_i) + \frac{i}{2}\Delta_n} \right|^2$$

where $\alpha_f = e^2/4\pi\epsilon_0\hbar c$ is a dimensionless quantity known as the fine structure constant.

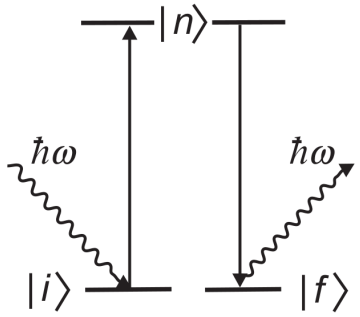

Figure 2.5: Schematic of an elastic resonant scattering event. The electron is excited out of its core state, $|i\rangle$, into an intermediate state of higher energy, $|n\rangle$, before de-exciting into its final state, $|f\rangle$, with the same energy as $|i\rangle$ and re-emitting the photon. In reality, the steps in this process happen simultaneously in a quantum mechanical framework. (Figure adapted from Ref. 84.)

wavefunction virtually explores all accessible paths of evolution, whereupon the photoabsorption channel resonates and is strongly enhanced in the probability-amplitude spectrum, before the photon moves on with a momentum profile that has been modified by the interaction. Truly, the resonant scattering process is a strictly quantum phenomenon, with the semi-classical picture serving mostly as a "cartoon" to guide us through its full complexity.

2.3.2 Comparison with Nonresonant Diffraction

It is helpful at this stage to be reminded of our ultimate goal: to understand the origins of a diffraction peak and how the underlying physics of a material changes its intensity (Equation 2.18). As is always the case for quantum phenomena, the mathematics of resonant scattering can quickly accelerate in complexity, and in practice it can be quite challenging to perform an exact calculation. Therefore, it is important to remember some key points when interpreting experimental results.

Neglecting experimental details, the intensity of a diffraction peak, whether on or off resonance, goes like the differential cross-section,

$$I \sim \left(\frac{d\sigma}{d\Omega}\right). \tag{2.44}$$

For nonresonant diffraction, the differential cross-section goes like the square of the struc-

ture factor,

$$\left(\frac{d\sigma}{d\Omega}\right) \propto |S(\vec{Q})|^2, \tag{2.45}$$

which is a weighted sum of atomic form factors $F_i(\vec{Q})$. In addition, the cross-section will be modulated by a polarization prefactor, which is controlled during an experiment.

Using a quantum formalism, the differential cross-section can also be written as proportional to the transition matrix,

$$\left(\frac{d\sigma}{d\Omega}\right) \propto T_{if}, \tag{2.46}$$

the equation for which is known but can be difficult to calculate analytically. To a good approximation, the scattering signal on resonance is such that

$$\boxed{\left(\frac{d\sigma}{d\Omega}\right)_S^R \propto \left|\vec{\epsilon}'^{\dagger} \cdot \hat{S}(\vec{Q}) \cdot \vec{\epsilon}\right|^2,} \tag{2.47}$$

with an additional, slowly-varying background intensity originating from nonresonant effects.

We highlight Equation 2.47 to emphasize it's importance. In the literature,[8,9,102] this relation is often given as the starting point for analyses of resonant x-ray scattering data. From here, interesting physics of a system under study can be revealed by considering the form and symmetry of $\hat{S}(\vec{Q})$ and its constituent matrix elements. Since the absolute intensity of a diffraction peak is dependent on experimental factors[1]—including geometry, vacuum conditions, and the quality of the sample's surface—scattering signals are typically recorded in arbitrary units that allow spectra to be scaled and offset; the ultimate value residing in how the shape and size of spectra compare relatively to one another. Therefore, exact calculations are not always required, but the proportionality in Equation 2.47 and an understanding of the symmetry of $\hat{S}(\vec{Q})$ suffice.

2.3.3 Element and Orbital Specificity

As previously discussed, hidden inside Equation 2.47 is the virtual transition of a core electron to an intermediate, excited state above the Fermi energy. This is responsible for several important effects not seen in classical scattering. The resonant component of the

[1]For soft x-ray energies, high absorption coefficients amplify this dependence.

scattering signal comes only from whichever pair of states resonate at the incident beam's energy, and since the energy separation between states is specific to each element, resonant scattering can select particular elements in a material for study. For example, in the high-T_c superconductor $YBa_2Cu_3O_{6+\delta}$, scattering at an energy of 931.3 eV resonates with the Cu L-edge and will reflect the periodicity of charge in that sublattice of atoms.

In addition, the matrix elements that generate Equation 2.47 imply that a strong scattering intensity requires a substantial overlap between the initial and excited states, not unlike what is seen in resonant XAS. The initial core state sits in a full shell with complete spherical symmetry, but the excited state is empty and often has an anisotropic angular dependence. For example, the L-edge scattering mentioned above lifts an electron from a filled $2p$ shell to, say, an empty $3d_{x^2-y^2}$ state with lobes that stretch out mainly along the x- and y-axes. Recall that the states in question contain not just the atomic orbitals but also the passing photon. This implies that the polarization of the incident beam is important when calculating the overlap, and in fact it significantly modulates the scattering intensity. The form in which the polarization vectors appear in Equation 2.47 confirms this intuition. In the classical framework of Equation 2.27, the polarization and the form factor are independent, and the inherent intensity of a diffraction peak only depends on the intensity of the form factor.[1] In the quantum formalism, however, the symmetry and orientation of the form factor tensor relative to the polarization vector are also critical to the scattering intensity. As well, the polarization of the x-ray beam can even be rotated during diffraction by off-diagonal terms in the form factor tensor, such as occurs in magnetic materials.

Continuing the example, the resonant L-edge structure factor for a Cu atom with an empty $3d_{xy}$ state could take a form like

$$\hat{S}_0(\vec{Q}) = \begin{bmatrix} s_{xx} & s_{xy} & s_{xz} \\ s_{yx} & s_{yy} & s_{yz} \\ s_{zx} & s_{zy} & s_{zz} \end{bmatrix} \approx \begin{bmatrix} s_{xx} & 0 & 0 \\ 0 & s_{xx} & 0 \\ 0 & 0 & s_{zz} \end{bmatrix}, \tag{2.48}$$

with $s_{xx} \gg s_{zz}$, and the dependence of the peak intensity on polarization would be

$$I \sim \left| \vec{\varepsilon}' \cdot \begin{bmatrix} s_{xx} & 0 & 0 \\ 0 & s_{xx} & 0 \\ 0 & 0 & 0 \end{bmatrix} \cdot \vec{\varepsilon} \right|^2. \tag{2.49}$$

Clearly, an incident polarization parallel to the c-axis results in minimal intensity, while a polarization parallel to either the x- or y-axes would show a strong scattering signal.

[1] The intensity of the peak will depend on polarization if measured with a polarization discriminating detector. But as is common for real RXS setups, we assume a polarization integrating detector.

Therefore, by tuning the incident beam's polarization, the amount of scattering from the $3d_{xy}$ state can be controlled by the experimenter. More generally, we can conclude that scattering from specific orbitals can be selected in an RXS experiment by the choice of beam polarization, and thus resonant scattering exhibits specificity not just to an element in the material (Cu), but also to an individual electronic state (Cu $3d_{xy}$).

Yet another important aspect of resonant scattering stems from the significant enhancement of the peak intensity. The magnitude of the atomic form factor is comparable to the number of electrons in the atom, Z, and thus a nonresonant diffraction peak has an intensity $\sim (nZ)^2$ for n atoms in a unit cell. One might naively assume, then, that a nonresonant peak, which scatters off electrons in just one electronic state in one element of the material, would have a far weaker intensity, ~ 1. However, as mentioned in Section 2.3.1, the resonance increases the efficiency of the scattering event by multiple orders of magnitude. Inspection of Equation 2.32 makes this intuitive, as the denominator of the second term, goes to zero when the beam's energy is tuned to a resonance. Therefore, one of RXS's most important applications is the study of ordering phenomena that involve few electrons. Returning to the example, charge-density wave order manifests in the Cu-O bonds in the plane-layers of $YBa_2Cu_3O_{6+\delta}$ below a critical temperature. While this modulation of charge is weak compared to the dramatic "charge-landscape" associated with the lattice, it can be targeted and easily resolved by resonant scattering off the appropriate orbitals. The signal from nonresonant scattering, on the other hand, is negligibly weak for this charge density wave.

In essence, resonant scattering combines the best of both worlds of x-ray absorption and conventional x-ray scattering. Like with any scattering technique, it is fundamentally a probe of a material's structure. But by resonating with the material's absorption edges, it gains the element and orbital selectivity, as well as the intensity enhancement, of resonant x-ray absorption that allows it to be used to study a material's electronic structure with high precision and sensitivity.

2.4 X-Ray Photoemission Spectroscopy

X-ray photoemission spectroscopy (XPS) is very similar to the TEY measurement method of XAS discussed in Section 2.1.3. An incident photon is absorbed and excites an electron into a higher-energy, free-electron-like state above the vacuum level. The electron then travels through the sample and experiences some probability of undergoing an interaction that will cause it to lose some or all of its energy; a probability that increases the longer it travels. If the electron was generated near the surface, there is an appreciable chance that

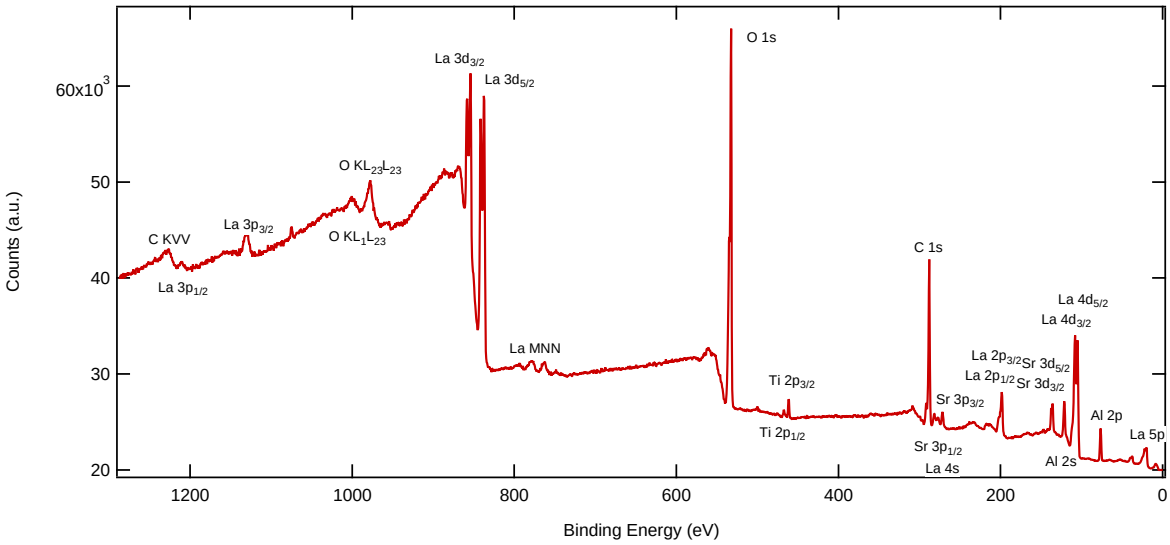

Figure 2.6: XPS spectrum of 9 unit cells of $LaAlO_3$ on top of a $SrTiO_3$ substrate using an Al K-α source. Note the presence of surface adsobants seen in the O 1s and C 1s peaks.

it will reach the edge of the sample still in an unbound state above the vacuum energy and be able to travel to the detector for measurement. Unlike in TEY, however, the measured electrons in XPS are discriminated by their energies, most often using a hemispherical analyzer. Therefore, while XPS can be performed with a tunable x-ray source such as a synchrotron, it is often performed with a far more convenient fixed-energy source, such as the K-α edge (1486.7 eV) of aluminium produced from Bremsstrahlung radiation and monochromated by reflection off the $<1010>$ surface of a quartz crystal. It is therefore not a resonant technique in the same sense as resonant XAS or scattering which require precise tuning of the incident energy. However, since the measurement is only sensitive to free-electron final states, which exist as a continuous function of energy, every excitation is resonant with an available unoccupied state, and resonant peaks similar to the ones in XAS are also seen in XPS spectra (Figure 2.6). In addition, the smooth variation in the density of unoccupied states implies that the sharp features in an XPS spectrum originate only from the contribution of the occupied density of states to the transition matrix (Equation 2.5). In that way, XAS and XPS, though originating from the same physical process, provide complimentary information about the material's unoccupied and occupied density of states (respectively) below the vacuum energy.

The details of the XPS process and the analysis of its results are deep, well-developed subjects. Again, we aim to provide only a brief overview here to prepare the reader for

discussion of data in later chapters, but there are a few important points to mention about features found in XPS spectra. For the same reasons as for TEY measurements of XAS, XPS is surface sensitive and is therefore subject to charging distortions on insulating samples, as well as the need to be performed in vacuum. Surface sensitivity is also the source of dramatic, unexpected peaks at the Cu and O edges, as seen in Figure 2.6, that appear due to the unavoidable presence of adsorbed water and hydrocarbon contaminants. To minimize these features, samples are often cleaned, cleaved, or even grown in the same chamber as the XPS apparatus to facilitate a quick subsequent measurement that doesn't break vacuum. Another notable feature is an increasing background level of counts that grows dramatically with binding energy. As mentioned above, the photoelectron can interact with the sample during its travel time between the initial excitation and its exit from the surface. Each absorption edge, therefore, will consist of a main line that represents electrons that avoided such interactions and escaped with their full energy, followed by an increasing tail of lower-energy electrons, known as secondaries, that did not.[1] With the onset of each new possible excitation channel, the trail of secondaries superimpose in the spectrum and produce an ever-growing background that for the lowest measured kinetic energies (highest binding energies), is comparable to the brightest resonant peaks. Finally, the phenomenon of satellite peaks is particularly well-pronounced in XPS. As discussed in Section 2.1.4, the semiclassical model ignores many complexities of the absorption process that are better captured through many-electron quantum mechanical wavefunctions, including especially the effects from the presence of the core hole. Without getting into many details—which depend to a large extent on the particular system being measured—multiple excitations of the many-electron configuration are often available with similar energies in the vicinity of an absorption edge. While one pathway tends to dominate in probability and forms the main line, one or more other pathways still occur with measurable intensity and create smaller resonant peaks that consistently appear in the vicinity of the mainline across the spectra of a material family.[2] Since they appear to shadow (or orbit) the main line, the term "satelite" was coined to refer to all of these peaks, even though the absorption pathways from which they originate can be quite diverse. For a (much) more thorough discussion of the theory and practical considerations of XPS, we refer the reader to Refs. 81 and 85.

[1] The secondary electrons can be the original photoexcited electrons that have lost some of their energy, or they can be newly excited electrons that were liberated from the sample through the absorption of some or all of the original electrons' energy (an Auger process). From a practical perspective, the distinction rarely matters.

[2] Typically, satelites exist at higher binding energy; sometimes at a fixed distance from the mainline, and sometimes at a fixed absolute energy.

Chapter 3

Symmetry of the Charge Density Wave Orbital Form Factor Studied with Resonant X-Ray Scattering

The electronic structures of transition metal oxides harbour many interesting properties, including the famous and intensely studied phenomenon of high-T_c superconductivity. In the family of underdoped cuprates, it has been established that the existence of a charge density wave (CDW)—characterized by a periodic spatial-dependence of charge or related microscopic quantity[67,102] in the orbitals of the CuO_2 planes—residing within the pseudogap region of the phase diagram generically coexists and competes with superconductivity, and understanding the properties of the CDW may lead to important insights about the interplay of the various correlations that generate this family's intricate phase diagram.[61,66,71,103–107] At present, specific knowledge for many materials of interest about the location and local symmetry of charges in the unit cell that participate in the CDW remains largely incomplete and an open area of research.

Recent theoretical studies of the cuprates have predicted CDW order with d-symmetry that in addition to the typical transfer of charge between unit cells (inter-unit cell symmetry breaking) also exhibits charge tranfer between atoms in a single unit cell (intra-unit cell symmetry breaking).[108–116] As shown in Figure 3.1, d-wave charge modulations are expected to occur predominantly on the O sites of the CuO_2 plaquettes, with modulations on sites cooridinated with the Cu-O-Cu bond direction along the a-axis out of phase with those along the b-axis such that the environment surrounding the Cu atom is quadrupolar.[8,109] The presence of such a symmetry has been verified with scanning tunneling microscopy

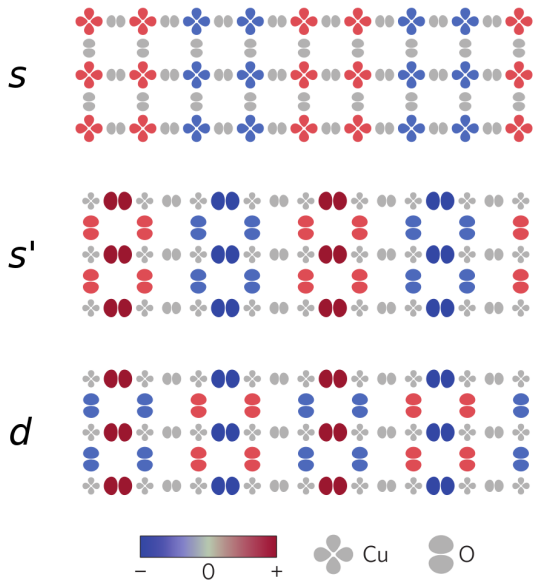

Figure 3.1: The CuO_2 plane layer in a cuprate viewed along the c-axis showing CDW order for a bond-centred, commensurate wave that runs along the horizontal crystallographic axis. Colour indicates charge density (or equivalent parameter). (top) A CDW with s-symmetry shows charge modulations primarily on the Cu orbitals, (middle) s'-symmetry primarily on the O orbitals, and (bottom) d-symmetry on the O orbitals with a π-phase shift between orbitals oriented along the horizontal and vertical axes. (Figure adapted from Ref. 8.)

(STM) and resonant soft x-ray scattering (RSXS) measurements in the hole-doped materials $Bi_2Sr_2CaCu_2O_{8+\delta}$ (Bi-2212)[106,117] and $Bi_2Sr_{2-x}La_xCuO_{6+\delta}$ (Bi-2201),[105] as well as in electron-doped $Ca_{2-x}Na_xCuO_2Cl_2$ (Na-CCOC).[117] Additionally, a recent study has reported a mix of symmetries with dominantly d-character in $YBa_2Cu_3O_{6+\delta}$ (YBCO), but the ability of this experiment to distinguish between dominantly d- and s- or s'-symmetry was close to the experimental accuracy.[7] Thus, the case for d-wave CDW order as a generic feature of the cuprates is beginning to materialize, and it is now imperative that further experimental evidence from a wider spread of materials be collected to supply a reliable confirmation or rejection of its universality.

The symmetry of charge ordering in the La-based cuprates is an important piece of this puzzle. CDW order in this canonical branch of the cuprate family tree shares many similarities with that in other branches such as the enhancement of the CDW transition temperature at 1/8 doping and competition of the CDW with superconductivity.[67,102,117–119]

However, it also exhibits some unique features like the doping dependence of its incommensurability with the lattice (see Figure 1.6).[104,105,118–123] In addition, it is the only cuprate to experience static spin density wave (SDW) order commensurate with CDW order (so-called stripe order), which could be of critical importance to the charge ordering symmetry.

In this chapter, we examine a sample of 1/8-doped $La_{2-x}Ba_xCuO_4$ (LBCO) using RSXS measurements at the Cu L_3 and O K edges to determine the charge ordering symmetry in the plane-layer orbitals. In contrast to previously studied cuprates, we find that the CDW order possesses a mix of symmetries with a majority s'-component; defined as inter-unit cell symmetry breaking, centred on the O sites. This result is derived using a model of the resonant scattering tensor to which our data is fit unambiguously. The implications of our result are discussed in the context of the unique stripe phase phenomenon, a perspective that has not been presented in previous studies.

In addition, we perform complimentary RSXS measurements of YBCO, another important and well-studied branch of the cuprates, at the Cu L_3 edge using an alternative geometry than used in previous studies where the effects of the CDW's symmetry on the shape of the spectra are more dramatic and thus more beneficial in distinguishing between symmetries. We study two single-crystal samples doped at $\delta = 0.75$ (YBCO-6.75) and $\delta = 0.67$ (YBCO-6.67). In contrast to the previous report,[7] we find very limited evidence for d-symmetry in either sample. Like the case of LBCO, the data is instead consistent with a scattering tensor having predominantly s'-symmetry, or perhaps a nontrivial mixture of d-, s'-, and s-symmetry (the last defined as inter-unit cell symmetry breaking, centered on the Cu sites). We again determine the components of the resonant scattering tensor, and we find a stark difference in the symmetry when the CDW is measured along the crystal's a-axis (the H-peak) versus the b-axis (the K-peak). This bolsters the hypothesis of there existing twin domains of unidirectional order in YBCO instead of omnipresent checkerboard order.[68,104,124] Furthermore, we find some evidence to support the plausibility of non-zero off-diagonal terms—a case not previously considered using this experimental technique—in the tensor describing the CDW along the a-axis that may support the existence of broken inversion symmetry. Finally, we note that there is little dependence of the symmetry on temperature or doping.

3.1 Experiment

Following a technique similar to that used in previous studies,[7,8] RSXS measurements were taken at a constant scattering wavevector Q corresponding to the CDW ordering peak while the incident beam's polarization and the sample were rotated to vary the orientation of

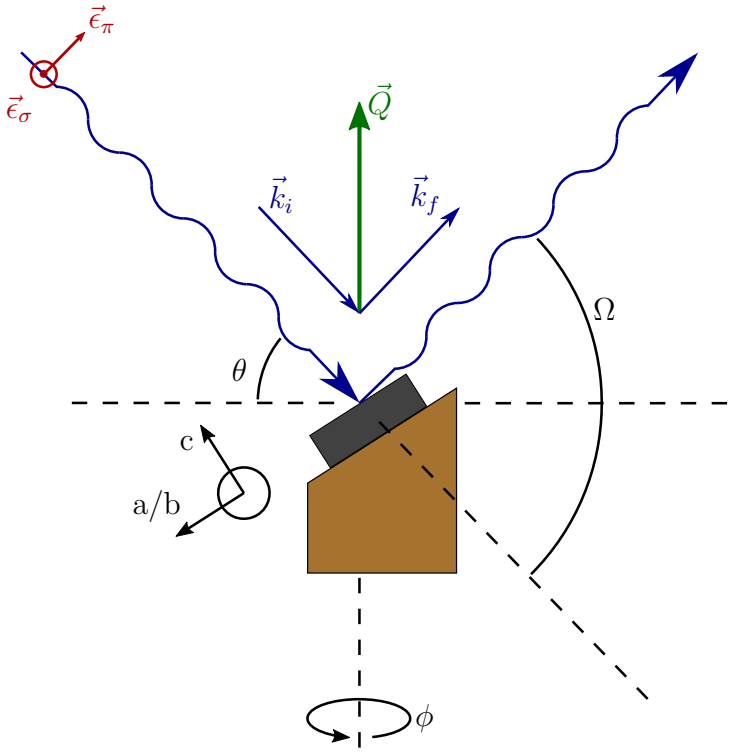

Figure 3.2: Schematic of the experimental geometry as seen from above showing the orientation when $\phi = 0°$. As ϕ is rotated, the scattering vector $\vec{Q}$ remains unchanged.

the $\vec{E}$-field relative to the crystallographic axes. As illustrated in Figure 3.2, the samples were mounted with UHV-compatible epoxy on a copper plug whose surface was carefully machined to a particular angle such that azimuthal rotation (ϕ) around an axis parallel to the central axis of the plug left the scattering vector $\vec{Q}$ unchanged. The crystal was mounted so that the a-axis was in the scattering plane and the CDW's H-peak, with $\vec{Q} = (H\,0\,L)$, was incident on the detector when $\phi = 0°$. Two measurements of the CDW peak were then recorded, one each for σ- and π-incident polarization, by rocking the scattering angle θ. Next, ϕ was rotated manually via an in-vacuum screwdriver to a series of values spanning a full 2π rotation, and the two measurements of the peak were repeated at each value. For YBCO, the samples were also remounted for a second round of measurements with the b-axis in the scattering plane and the CDW's K-peak, $\vec{Q} = (0\,K\,L)$, on the detector when $\phi = 0°$, and the procedure was repeated.

The LBCO sample was grown using the travelling solvent floating zone method and the YBCO samples by the self-flux method using high-density $BaZrO_3$ crucibles.[125,126] A

verification of their crystallographic integrity and orientation was performed before the samples were sent to the synchrotron. Immediately before starting the experiment, a fresh surface of LBCO was exposed by a top-post cleave[1] in air. The YBCO samples were mechanically polished in air down to a grit size of 0.05 μm and gently cleaned in organic solvents to remove surface residues. Once loaded into the vacuum chamber, the experiment was performed in a pressure of approximately 10^{-10} Torr.

The experiment was performed in the RSXS endstation of the REIXS beamline, described in detail at the time of its commissioning in Ref. 127. Samples there are manipulated with an in-vacuum, four-circle diffractometer capable of a wide range of motion along θ (better than $0° \leftrightarrow 180°$), as well as limited motion along χ and ϕ ($\sim \pm 4.5°$) for tweaking the sample's crystallographic alignment *in situ*. Motion along x, y, and z is also possible to optimize the detection position and allow for multiple small samples to be mounted simultaneously. The detector array sits in the horizontal plane parallel to the θ-circle and is capable of measuring at positions spanning $0° < \Omega < 176°$.[2] It houses a microchannel plate (MCP), a single-channel electron multiplier (Channeltron), and a photodiode. The MCP is capable of collecting a wide-area measurement (25 mm diameter) that is spatially resolved[3] and useful when initially searching for Bragg peaks. It and the Channeltron are highly-sensitive, capable of detecting single photons, but only the photodiode can be exposed to the direct beam or high-intensity Bragg peaks without incurring damaged. A variety of slits and filters are built into a wheel in front of the Channeltron and photodiode that can be rotated to narrow the detection area and shield out photoelectrons, respectively. The polarization of the incident beam can be freely rotated between σ- and π-orientations by adjusting the undulator, as well as tuned to left- or right-circular polarization. The beam's energy resolution is affected by the adjustable spot size, but is $\Delta E/E \simeq 10^{-4}$ for a typical spot of 250×150 μm (horizontal×vertical). The flux, which depends on spot size, energy, and beam current, is typically better than 10^{12} s^{-1}/0.1% bandwidth.

[1] A top-post cleave is performed by gluing a small object—often a screw or other piece of clean hardware lying around the laboratory—to the surface of the sample. Ideally, the connected surfaces should be roughly equal in size and shape to produce the best cleave. The top-post is then struck abruptly from the side with the hope that the shearing, torquing force at the connection point breaks the sample along a simple crystallographic plane approximately parallel to the glued surfaces. In some cuprates, top-post cleaving is highly successful, especially when exposing the *ab*-plane since the bond along the *c*-axis between unit cells is comparatively weak. Ultimately, though, the quality of the cleave is never guaranteed in any material, and is not uncommon to have to repeat the procedure two or more times before the sample is ready for measurement.

[2] Wider motion is possible, but the beam is usually cutoff by equipment on the detector arm outside of this range.

[3] Only spatially-integrated data was able to be recorded for the experiments in this thesis. At the time of writing, recording of spatially-resolved data is under development.

After entering the vacuum chamber, the sample was moved into the diffractometer's center of rotation, and a fine calibration of the rotation motors to correct errors in mounting was performed using multiple Bragg peaks as references. Two of the strongest and most easily accessible peaks were the (0 0 2) and (±1 0 3). For the dimensions of the unit cells in the cuprates, the (0 0 2) peak can be found near the Cu L edge where the beamline's energy is reliably calibrated. However, the (±1 0 3) needs energies above ~ 2 keV, and the beam required a secondary calibration at this energy.[1]

The samples were assumed to have lattice parameters $a = b = 3.787$ Å and $c = 13.24$ Å for LBCO and $a = 3.84$ Å, $b = 3.88$ Å, and $c = 11.74$ Å for YBCO, which were taken from the literature and consistent with Laue diffraction data that we recorded to assist in orientation and mounting.[8,9,118,128–133] The necessary angle at which to cut the plugs was calculated using the formula

$$\tan \xi = \frac{Hc}{La}, \tag{3.1}$$

which puts the $(H\,0\,L)$-plane perpendicular to the incident beam when $\theta = 0$. Aligning the diffractometer to a scattering vector $\vec{Q} \propto (H\,0\,L)$[2] then causes the azimuthal axis of rotation, which is parallel to $\vec{Q}$, to divide the angle between the incident and detected beams in half, and thus rotating ϕ leaves the scattering vector unchanged. The LBCO sample was measured on a plug whose surface was cut at an angle of 53° for data at the O K edge and another plug cut to 34° for the Cu L edge. The YBCO samples, only measured at the Cu L edge, were mounted on plugs cut to 32.5° and 35.5° to facilitate observations at the centre of the CDW peak with respect to H and multiple values of L.

As illustrated in Figure 3.3, the measured data consists of the CDW peak on top of a unique, slowly-varying fluorescent background that depends on the particular surface geometry and the instantaneous values of ϕ and θ. The background was fitted outside of the peak region for each spectrum with a fifth-degree polynomial, and after subtraction, the remaining peaks were fit to Lorenztians to determine their amplitudes and other properties. Variations in the details of the fitting procedure were explored and showed little effect on the final result. The ratios of intensity when using σ- and π-polarization were then plotted and fit with a least-squares regression to determine the components of the scattering tensor (see below and Section 2.3).

[1] Contact the author for further details.

[2] Recall that the magnitude of $\vec{Q}$ is proportional to the photon energy and thus remains a tunable parameter at this geometry.

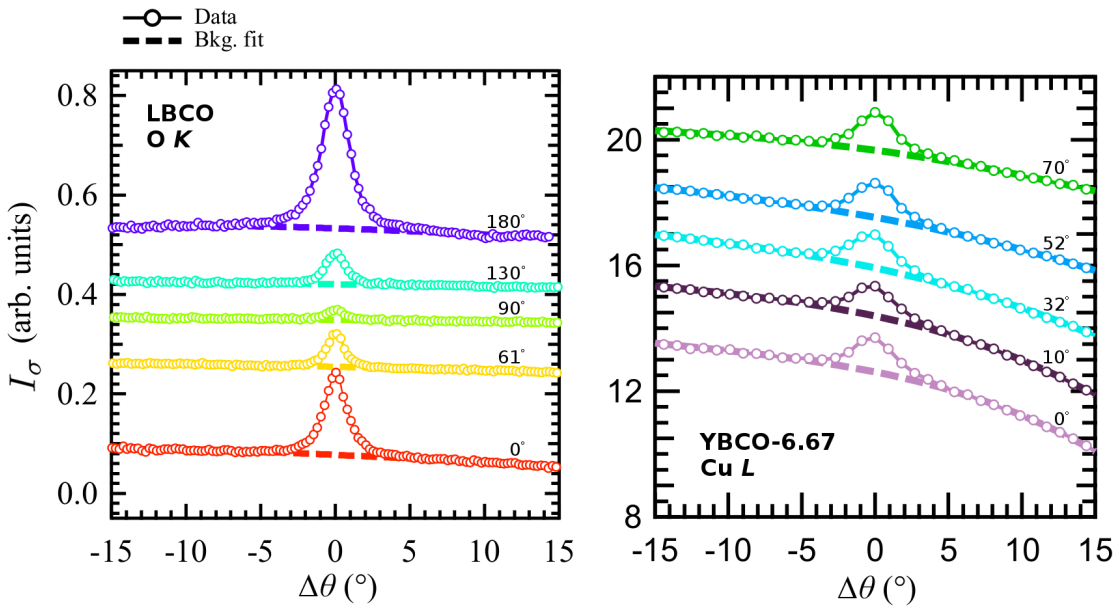

Figure 3.3: Direct measurement of the CDW H-peak in (left) LBCO at the O K edge centred at the reciprocal space location $(-0.232\,0\,0.611)$ and (right) YBCO-6.67 at the Cu L edge centred at $(0.31\,0\,1.321)$ at some example values of ϕ (labelled). Spectra are vertically offset for clarity. Background regions excluding the peaks are fit with polynomials (dashed lines) and later subtracted to isolate the peaks. Spectra are plotted relative to their ideal scattering angle, $\Delta\theta = 0$. Notice the larger maximum amplitude and larger variation with ϕ of the CDW peak at the O edge relative Cu, a pattern seen across the materials in this study. This is consistent with stronger modulations of charge in the O orbitals due to the dominant presence of s'- or d-symmetry.

3.2 Modelling the Form Factor

The peak intensities as a function of azimuthal angle were modelled using elementary resonant diffraction theory (see Ref. 94, for example). As discussed in Chapter 2.3, the intensity of a resonant diffraction peak is approximately proportional to the square of the scattering tensor:

$$I(\hbar\omega) \propto \left|\vec{\epsilon}' \cdot \hat{F}(\vec{Q}, \hbar\omega) \cdot \vec{\epsilon}\right|^2 \tag{3.2}$$

where $\vec{\epsilon}$ and $\vec{\epsilon}'$ are the incident and scattered polarization vectors, respectively. The proportionality prefactor, as well as any nontrivial effect from the sample's surface that isn't otherwise accounted for, is not dependent on the incident polarization,[1] and thus it can be eliminated by choosing to calculate the ratio of intensitites measured using σ- and π-polarization, I_σ/I_π, as the final result. Such a procedure was also performed in previous works.[7,8] After adjusting for self-absorption effects (see Chapter 2.1), the ratio could be modelled exactly in terms of the beam energy, experimental geometry, and the nine scattering tensor components f_{ij}. Since the energy and geometry is known experimentally to high precision, the tensor components remain the only unknowns and could be fit with a least squares regression.

To interpret the meaning of the tensor components as they relate to the symmetry of the CDW, we follow the approach from Refs. 7 and 108. When charges order in the CuO_2 planes, the charge density takes the form of a constant background, ρ_0, with an additional periodic modulation function, $\Delta\rho(\vec{r})$. The latter can be decomposed into components representing the charge in the $3d$-like environment around Cu "sites,"

$$\Delta\rho_{\text{sites}}(\vec{r} - \vec{r}_i) = \frac{\Delta q}{2V}\Delta(\vec{r}_i, \vec{r}_i)|\psi_{3d_{x^2-y^2}}(r - r_i)|^2, \tag{3.3}$$

and the charge in the $2p$-like environment around the O "bonds" that join the Cu ions along a and b,

$$\Delta\rho_{\text{bonds}}(\vec{r} - \vec{r}_i) = \frac{\Delta q}{2V}\sum_j \Delta(\vec{r}_i, \vec{r}_j)\left|\psi_{2p_j}\left(\vec{r} - \frac{\vec{r}_i + \vec{r}_j}{2}\right)\right|^2; \tag{3.4}$$

where $\Delta(\vec{r}_i, \vec{r}_j)$ is the real-space order parameter, $\vec{r}_i$ is the location of the Cu ion, $\vec{r}_j$ is the location of a neighbouring O ion, V is the volume of the unit cell, and the sum is over

[1] This statement is a little too general when talking about surface effects. Reflection, for example, is polarization-dependent, as is accidental scattering from resonant edges of adsorbed compounds. In practice, however, these effects are rarely significant for this kind of calculation.

nearest neighbours sitting at coordinates $(\pm\frac{1}{2}a, 0)$ and $(0, \pm\frac{1}{2}b)$. The Fourier transform of the order parameter can then be written,

$$\Delta_{ij} = \frac{1}{V} \sum_{\vec{Q}_{\mathrm{CDW}}, \vec{k}} e^{i\vec{k}\cdot(\vec{r}_i - \vec{r}_j)} \Delta(\vec{k}, \vec{Q}_{\mathrm{CDW}}) e^{i\vec{Q}_{\mathrm{CDW}} \cdot \frac{(\vec{r}_i + \vec{r}_j)}{2}} \tag{3.5}$$

where $\vec{Q}_{\mathrm{CDW}}$ is the reciprocal space vector(s) of the CDW. This can in turn be decomposed into contributions from individual symmetry modes—Δ_s, $\Delta_{s'}$, and Δ_d—such that we can write[108]

$$\Delta(\vec{k}, \vec{Q}_{\mathrm{CDW}}) = \Delta_s + \Delta_{s'}(\cos k_a a + \cos k_b b) \pm \Delta_d(\cos k_a a - \cos k_b b) \tag{3.6}$$

where the $+$ and $-$ in front of Δ_d is determined by whether the H or K CDW peak is being measured, respectively.

The relative sensitivity of a scattering measurement to each of these symmetry order parameters Δ_x varies depending on the absorption edge being probed, and therefore the mapping between them and the tensor components f_{ij} also varies. At the O K edge, the measurement is primarily sensitive to the s' and d order parameters that describe modulations in the $2p$ orbitals around O ions. It can be shown [8, supplemental] that

$$\begin{aligned} f_{aa}^{(\mathrm{O})} &= \Delta_{s'} + \Delta_d \\ f_{bb}^{(\mathrm{O})} &= \Delta_{s'} - \Delta_d \,, \\ f_{cc}^{(\mathrm{O})} &= 0 \end{aligned} \tag{3.7}$$

where f_{cc} has been set to zero due to the vanishing out-of-plane contribution from the O $2p_x$ and $2p_y$ orbitals. At the Cu L edge, the measurement is conversely more sensitive to s-symmetry that corresponds to modulations in the $3d$ orbitals around the Cu ions. It can similarly be shown [7, supplemental] that

$$\begin{aligned} f_{aa}^{(\mathrm{Cu})} &= \delta_s + (\delta_{s'} + \delta_d)\cos(\vec{Q}_{\mathrm{CDW}} \cdot \frac{a}{2}\hat{a}) \\ f_{bb}^{(\mathrm{Cu})} &= \delta_s + \delta_{s'} - \delta_d \\ f_{cc}^{(\mathrm{Cu})} &= \gamma\delta_s \end{aligned} \quad , \tag{3.8}$$

where γ is an empirically-derived scaling factor (estimated to be $\simeq 0.1$ for YBCO, for example[7]). To avoid the trivial solution, pseudo symmetry order parameters δ_x have been introduced that approximate the actual order parameters with an error that depends on the extent of the heightened sensitivity to s-symmetry. Unfortunately, the precise way to

quantitatively map $\delta_x \rightarrow \Delta_x$ remains an open question, but we can say that the comparative ratios $\delta_s/\delta_{s'}$ and δ_s/δ_d are overestimations to some degree of the CDW's s-character. Regardless, exploring their relative magnitudes still provides useful information about the mixture of CDW-symmetries in the material.[7]

Finally, we introduce a notational convention and redefine the three diagonal tensor components in terms of their relation to the CDW $\vec{Q}$-vector: the in-plane component along $\vec{Q}$, $f_\parallel$; the in-plane component perpendicular to $\vec{Q}$, $f_\perp$; and the out-of-plane component, f_{cc}. For measurements of the H-peak, we have $(f_\parallel, f_\perp) = (f_{aa}, f_{bb})$, and for the K-peak, $(f_\parallel, f_\perp) = (f_{bb}, f_{aa})$. Since we ultimately seek a ratio of measured scattering intensities, the absolute magnitude of the tensor components is an extraneous degree of freedom; only the relative magnitude of each component affects the fit. We thus normalize the tensor with respect to $f_\perp$, and ultimately reduce the original nine unknown tensor components to only $f_\parallel/f_\perp$ and $f_{cc}/f_\perp$ as parameters in our fit.

3.3 Results and Discussion

3.3.1 LBCO

A sample of 1/8-doped LBCO was measured at the CDW's H-peak at the O K and Cu L resonances, and the resulting data is summarized in Figure 3.4. Spectra with backgrounds removed are showcased in the top row (3.4(a)) for π and σ incident polarizations, organized as a function of azimuthal angle ϕ (defined in Section 3.1). The O spectra are centered at a reciprocal space vector of $(-0.232\ 0\ 0.611)$, and the Cu at $(-0.236\ 0\ 1.192)$. An oscillating ϕ-dependence is immediately apparent at both edges that is out of phase between the two polarizations. This is due in large part to geometric effects whereby the angle of the electric field vector $\vec{E}$ varies with respect to the hole-states, whose wavefunctions run mainly along the a and b crystal axes. In addition, the π spectra achieve weaker maximum intensities than σ because $\vec{E}$ has a nonzero component along the c axis with this polarization, and can thus never be fully parallel to the antinodes of the hole states.

A fit to each peak reveals maximum intensities plotted as points in the upper row of Figure 3.4(b) (blue and green), and their ratios I_π/I_σ are plotted in the lower row (black). Performing a least squares fit of the O data (left column) using the model of Equation 3.7, as well as correcting for absorption effects (see Chapter 2.1.3), yields tensor parameters $f_\parallel/f_\perp = 0.612 \pm 0.035$ and $f_{cc}/f_\perp = 0.034 \pm 0.021$.[1] Plotting the results of this fit provides

[1] For details concerning the calculation of the uncertainty limits, see Ref. [8, supplemental].

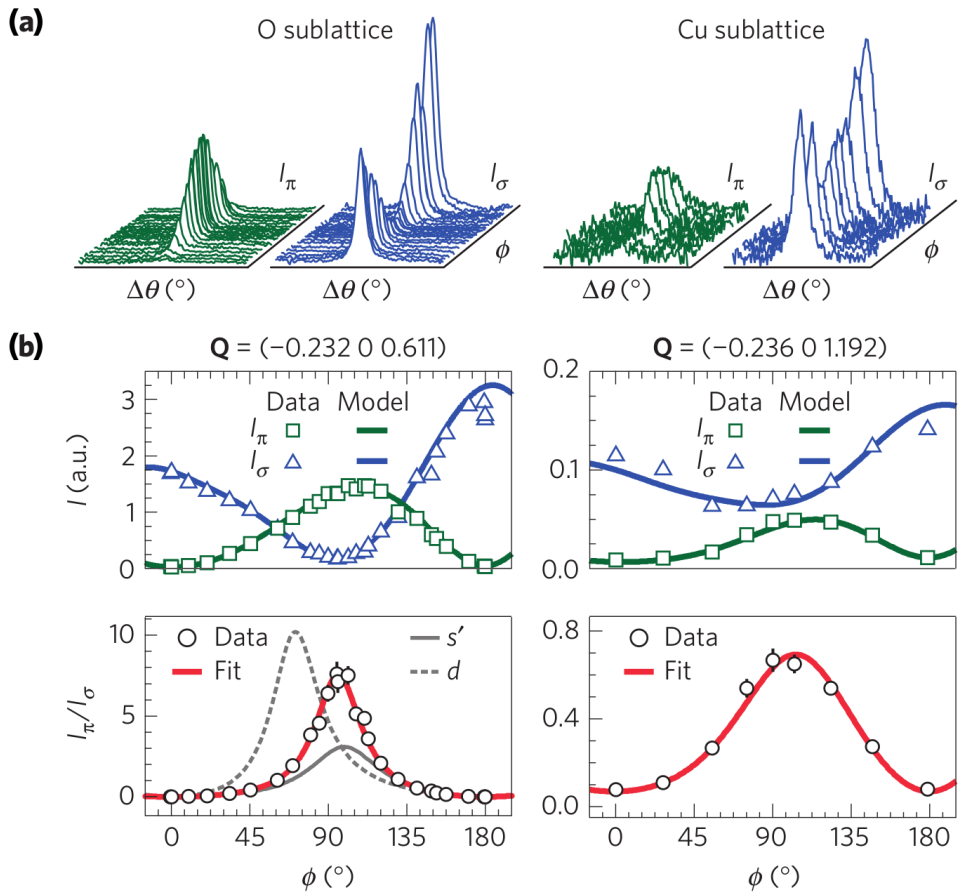

Figure 3.4: (a) Recorded spectra of the CDW H-peak with backgrounds removed for π (green) and σ (blue) incident polarizations. Scans were taken by varying the sample's scattering angle θ about the optimal position $\vec{Q}$. Data is presented for the O K (left) and Cu L_3 (right) absorption edges. (b) Peaks were fit and their amplitudes plotted as a function of ϕ (top). Similarly, the ratio of σ to π polarization was also plotted (bottom). The red curves were modelled using resonant diffraction theory and fit to the data. Example curves resulting from purely (solid) s'- and (dashed) d-symmetry are shown as grey curves for comparison.

a close match to the data, as shown by the red curve in the lower row. Satisfyingly, the individual peak amplitudes are also captured well by these parameters as demonstrated by the blue and green curves in the upper row that were generated using the fit parameters and one additional vertical scaling factor. We interpret this as evidence that our model has successfully taken all necessary experimental effects into account.

The ratio of $f_{\parallel}/f_{\perp} \simeq 0.6$ indicates a significant breaking of C_4 rotational symmetry in the O $2p$ orbitals with substantially smaller modulations along $f_{\parallel}$, which here corresponds to the a axis. While some anisotropy in the scattering tensor is expected due to differences in the hopping parameter between the a and b axes caused by the presence of the low-temperature tetragonal structural phase in LBCO (see Chapter 4), such an effect has been shown to be only about 3%.[134] Therefore, almost the entirety of the symmetry breaking appears to be attributable to the CDW. In addition, the ratio of the in- and out-of-plane components, $f_{cc}/f_{\perp}$, indicates a small modulation along the c axis, as expected, but one that is nonzero within the calculated uncertainty range.

Substituting these values from the fit back into Equation 3.7, we find $\Delta_d/\Delta_{s'} = -0.241$, where the negative value implies that the d- and s'-symmetry modes exist out of phase. This result indicates that the modulation has a mix of the two symmetries, but the s'-component is over four times stronger than d. This stands in sharp contrast to previous reports on other cuprates[7,105,106,117] where a dominant d-character was observed using STM and RSXS. For comparison, model curves of the intensity ratios with exclusively d- and s'-symmetry are plotted in Figure 3.4 (grey; solid and dashed, respectively), and each alone demonstrates a poor representation of the measurement.

Similarly, fitting the Cu data (right column) using Equation 3.8 gives $f_{\parallel}/f_{\perp} = 0.991 \pm 0.015$ and $f_{cc}/f_{\perp} = -0.067 \pm 0.015$, and plots generated with these parameters again fit both the ratio data (red and black) and peak amplitude data (blue and green) quite well. Unlike at the O edge, we now observe an in-plane modulation that is almost isotropic. However, it is interesting to note that the small presence of broken symmetry again favours a weaker modulation along the a axis. The out-of-plane component, f_{cc}, is once again small but nonzero.

As discussed in Section 3.2, calculating the symmetry mode order parameters is more challenging at the Cu edge. Resonant absorption at this energy is primarily sensitive to the s-symmetry mode, which to first order produces a trivial solution to the scattering tensor. Including higher-order terms incorporates the other symmetry modes, but it also introduces the difficult problem of understanding the relative sensitivity of the measurement to the neighbouring O orbitals. In other words, the measurement is dependent on the amount of mixing that occurs between the Cu and O valence states, as well as any influence the CDW's

presence may have on the energy and shape of neighbouring orbitals—properties that strike at the heart of the study of strongly correlated electronic structures. Furthermore, the three-dimensional nature of the Cu $3d$ states invalidates the approximation used for the O data that the CDW exists only in the two-dimensional plane cutting through the CuO_2 plaquettes, and this necessitates the introduction of the γ scaling parameter.

To confront these challenges, we proceed by first attempting to solve Equation 3.8 for γ. Eliminating δ_s from the system of equations, γ can be expressed with only a dependence on the parameters from our fit and the ratio $\delta_d/\delta_{s'}$. Assuming the sensitivity of our measurement is approximately equal for the d- and s'-symmetry modes, which one would expect from the symmetry of the O $2p_x$ and $2p_y$ states, then we can assume the ratio calculated for the O edge is still approximately correct for the case of Cu (i.e. $\delta_d/\delta_{s'} \simeq \Delta_d/\Delta_{s'} = -0.241$). We then find that $\gamma = -0.068$, which is of the expected magnitude,[1] and $\delta_{s'}/\delta_s = 0.0212$ and $\delta_d/\delta_s = -0.00210$. Given the heightened sensitivity to s-symmetry, it is not surprising that the magnitude of these last two ratios is so much smaller than $\Delta_d/\Delta_{s'}$, and we cannot say to what extent s-symmetry prevails in this material. However, the three ratios together paint the picture of a predominantly monopolar CDW.

The symmetry of the CDW can also be examined by directly comparing the results of fitting the Cu data to expectations about the form of the scattering tensor. A simple sinusoidal modulation of charge density in the planar orbitals corresponding to a monopolar CDW should produce a scattering tensor with the same symmetry as the average electronic structure ($\vec{Q} = 0$) of the states being probed. At the Cu L_3 edge, the holes reside primarily in $d_{x^2-y^2}$ orbitals that have roughly D_{4h} symmetry, and thus the resulting scattering tensor should have $f_{aa} \simeq f_{bb}$ and $f_{cc} \ll f_{aa}$. Alternatively, a quadrupolar CDW whose modulations in the O $2p_x$ and $2p_y$ are out of phase should have $f_{aa}/f_{bb} < 0$. Clearly, the former prediction more accurately represents the data, and the evidence again supports a primarily monopolar CDW.

As seen across the cuprates, the CDW in LBCO has a short correlation length along the crystal's c-axis, and therefore the scattering peak is broad in L. In Figure 3.5, the ratio of I_π/I_σ was measured for $\phi = 0$ by rotating the incident polarization and varying the value of L. This data was also included in the fitting procedure to obtain the parameters reported above. Again plotting our model in red, we find satisfying agreement at both energies.

Assuming previous reports of majority d-symmetry in other cuprates[105,106,117,117] were not influenced by an unaccounted-for heightened sensitivity to that mode in their respective measurements, then symmetry could be another property of the CDW that uniquely

[1] Specifically that $|\gamma| \ll 1$.

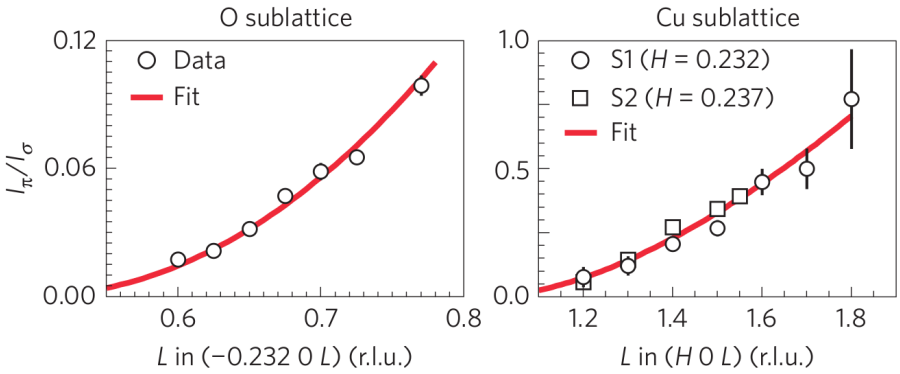

Figure 3.5: L-dependence of the ratio of π to σ polarizations measured at the O K (left) and Cu L (right) absorption edges. Red curves are fit using the same parameters as Figure 3.4. Note that two samples of LBCO were measured at the Cu edge at slightly different values of $\vec{Q}$.

separates the La-based cuprates from other families. Only in the La-based cuprates is a static spin-density wave (SDW) found with a lattice incommensurability that is half that of the CDW.[8,61,118,128] This is typically explained using a model where the local charge correlates with ferromagnetic ordering. For example, in areas where the amplitude of the CDW is above the average charge density, neighbouring Cu sites align ferromagnetically and antiferromagnetically elsewhere.[8,61,135,136] If this phenomenon is unique to the La-based cuprates, so too could be the symmetry of its CDW.

This kind of correlation between charge and spin ordering should favour monopolar charge symmetry. Specifically, a CDW with s'-symmetry exhibits in-phase modultations of nearby $2p_x$ and $2p_y$ orbitals. This would generate a behaviour in the SDW where the spin density on the Cu sites modulates according to the charge density on its surrounding O bonds, which is consistent with the stripe order model associated with the La-based cuprates.[61,137] A CDW with d-symmetry, on the other hand, has local $2p_x$ and $2p_y$ orbitals modulating out of phase, reducing the average charge modulation around Cu sites. Such a landscape would seem incompatible with the observed SDW if the proposed spin-charge correlation is correct. Therefore, it may be that the preference in the La-based cuprates for s'-symmetry is what allows for their unique SDW. Or conversely, the presence of the SDW may encourage an s'-symmetry of the CDW. Indeed, a theory of electronic order in the cuprates that predicts static SDW and CDW order has found a dominantly s'-symmetry.[138] Multiple theories that have predicted d-symmetry, however, have not found the simultaneous presence of static SDW and CDW order.[108,109,112,139,140]

The symmetry of the CDW may also have a role to play in the strength of the supercon-

ducting phase. It is believed that CDW order competes with superconductivity generically across the cuprates, but the mechanism by which this occurs is a topic of debate. The model of the strip phase with s' CDW+SDW order in the La-based cuprates predicts an optimal doping of 1/8,[61] which is of course also approximately where T_c is found to be maximally suppressed and the CDW is the strongest. Furthermore, while the 1/8 anomaly occurs in many materials, it is especially intense in the La-based cuprates, particularly in LBCO (see Figure 4.5). Therefore, it may be that a CDW with s'-symmetry, which may be especially favourable in the La-based cuprates due to the stripe phase, is more detrimental to superconductivity than d-symmetry. And since d-symmetry order parameters couple primarily to antinodal quasiparticles, this mechanism of competition may be especially apparent in the nodal region.

3.3.2 YBCO

Two samples of YBCO were studied with doping levels at $\delta = 0.75$ (YBCO-6.75) and $\delta = 0.67$ (YBCO-6.67). This corresponds to a carrier concentration of about $p = 0.13$ with a low-temperature oxygen ordering structural phase of OIII[1], and $p = 0.12$ with OVIII, respectively.[133,141] Repeating the procedure employed for LBCO, measurements were taken at the Cu L_3 edge with an in-plane component of the scattering vector $\vec{Q}$ of 0.31 that corresponds to the maximum of the CDW peak. As before, the backgrounds were fit with polynomials and removed, and the resulting spectra were fit with Lorentzian functions to determine their peak intensity. Finally, the ratio of the peak intensities for σ and π polarization was calculated for each value of ϕ and fit to a scattering tensor. Example data are given in Figure 3.6 for the YBCO-6.75 sample in the K-peak orientation and an out-of-plane component of $L \simeq 1.33$.

The results for all samples and orientations, as well as the calculated curves for fitted tensors, are summarized in Figure 3.7. Data for the H- and K-peaks using a measurement geometry with $\Omega \simeq 170°$ ($L \simeq 1.5$) are shown in the upper panels 3.7(a) and 3.7(b), respectively, and similarly for $\Omega \simeq 134°$ ($L \simeq 1.3$) in the lower panels 3.7(c) and 3.7(d). In addition, data from Comin *et al.*[7] for the K-peak of YBCO-6.75 with $\Omega \simeq 170°$ is reproduced in 3.7(b). Of course, the precise value of L in these measurements varies as the the dimensions of the unit cell changes with doping. Thus, YBCO-6.75 was measured with $L \simeq 1.48$ and $L \simeq 1.33$, and YBCO-6.67 was measured at $L \simeq 1.32$.

[1]The structural phase of neither sample was verified in this study, but both have been confirmed previously in related studies. These are the expected phases in which samples at these dopings would exist in thermal equilibrium at low-temperature. For more, see Ref. 10.

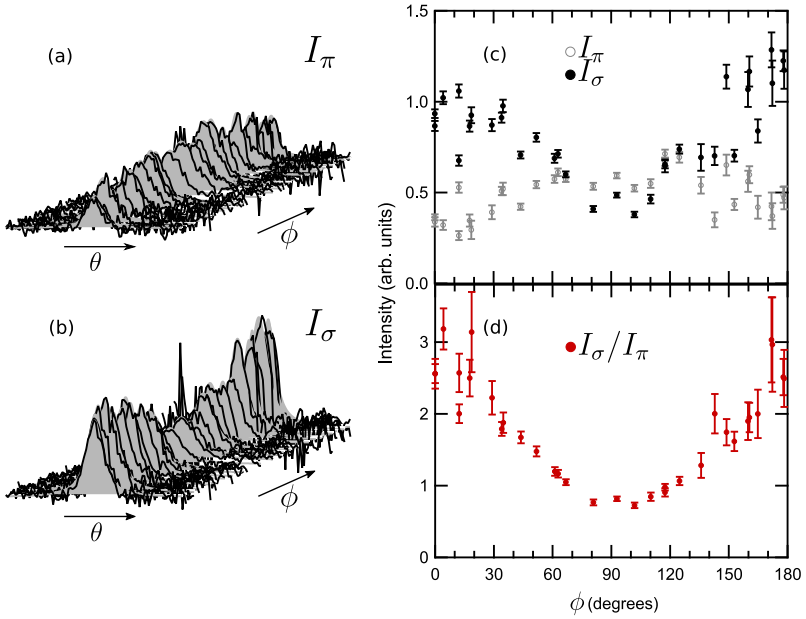

Figure 3.6: Intensity measurements of the CDW peaks for YBCO-6.75 in the K-orientation. (a) The peak profiles with fluorescent backgrounds removed as a function of θ and ϕ for π- and (b) σ-polarizations. Lorenztian fits to each peak are shown as grey shading. (c) The amplitude of each fit plotted against azimuthal angle. (d) The ratio of the two data sets.

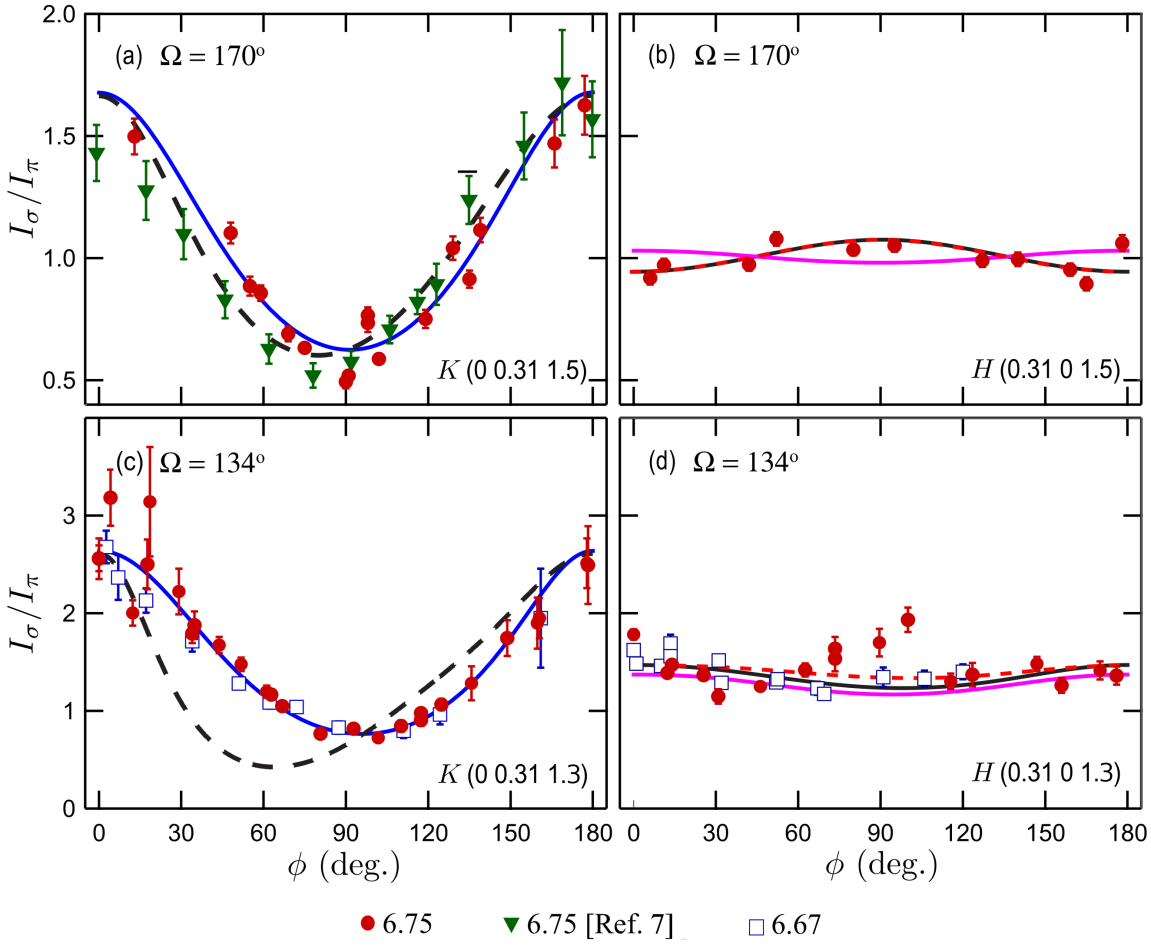

Figure 3.7: Ratio I_σ/I_π of measured intensities for the (0.31 0 L) CDW H-peak (a, c) and (0 0.31 L) K-peak (b, d). The upper row (a, b) shows data taken close to the peak's maximum at $L \simeq 1.5$, while the bottom row (c, d) shows $L \simeq 1.3$ where peak-intensity is reduced but the data is more sensitive to the symmetry of the CDW. (Exact L values are indicated.) The solid lines are fits to a model assuming only diagonal components of the scattering tensor are nonzero. The fit for the H-peak (black line in (a) and (c)) and K-peak (grey line in (b) and (d)) data were performed separately as no single tensor fit both data sets simultaneously. In panels (b) and (c), the green triangles and dashed line are the data and fit, respectively, reproduced from Ref. 7. The blue dash-dotted line in (a) and (c) is a fit to a model allowing the off-diagonal tensor component f_{ac} to be nonzero, which requires breaking of inversionsymmetry.

Fit	Line	$f_{\parallel}/f_{\perp}$	$f_{cc}/f_{\perp}$	$f_{ac}f_{\perp}$
K-peak	———	0.998	0.049	0
K-peak from Ref. 7	- - -	-1.022	0	0
H-peak	———	1.42	-0.15	0
H-peak	———	1	0	-0.225
H-peak	- - -	1.32	0.065	$\pm$0.116

Table 3.1: Optimized parameters for the fits plotted in Figure 3.7.

A striking difference between measurements of the H- and K-peaks is immediately apparent, with the K-peak data exhibiting substantially larger oscillations. We could find no scattering tensor (see below) whose components realistically reflect the symmetry of the crystal structure and generate a satisfactory fit to both peaks simultaneously. We take this as compelling evidence to support the existence of two distinct domains—with consequently different orbital symmetries—of unidirectional CDW order coexisting in YBCO. We thus proceeded to calculate separate parameter sets for the H- and K-peaks, which are summarized in Table 3.1.

The same model of the scattering tensor as described above for LBCO (Equation 3.8) was used to fit the ratio data. Measurements at all values of L were fit simultaneously, as well as the data for both doping levels as the results show little variation between $\delta = 0.75$ and $\delta = 0.67$. The K-peak data produced a ratio of in-plane components close to unity, $f_{\parallel}/f_{\perp} = 0.998 \pm 0.020$, with a small out-of-plane contribution, $f_{cc}/f_{\perp} = 0.049 \pm 0.041$. The fact that the scattering tensor again follows the predicted form of $f_{aa} \simeq f_{bb} \gg f_{cc}$ is strong evidence for a predominantly monopolar CDW. Notably, this is incompatible with the report of dominantly d-character by Comin *et al*, and at most the evidence could be consistent with a mix of symmetries that has a small quadrupolar contribution.

We further explore this result by examining the data from Comin *et al.* of the K-peak in YBCO-6.75 superimposed on our own data in Figure 3.7(b) and (d). The fit parameters reported, $f_{\parallel}/f_{\perp} = -1.022$ and $f_{cc}/f_{\perp} = 0$, produce a similar curve to our own for the $L \simeq 1.5$ data, as expected. However, the measurement gains significant sensitivity to the symmetry of the CDW when L is decreased due to the change in how ϵ and ϵ' access the crystallographic axes as ϕ is rotated. Thus, changes to the tensor components induce more obvious variations in the shape of the fitting curve. Clearly, the given tensor values no longer provide a satisfactory fit to the measurement at $L \simeq 1.3$, and differences between the two fits that were subtle at $L \simeq 1.5$ have now become dramatic. The resultant effect on the calculated symmetry components, as stated above, is also substantial in both quantitative and qualitative terms, and we therefore advocate for a change in practice when conducting

this type of experiment. While it often seems advantageous to measure the CDW peak at its maximum, especially given how weak the peak's intensity can be at some dopings, a measurement at an off-peak L-value should be considered as it can vitally improve the precision of the results.

Fitting the H-peak data revealed a ratio for the in-plane components of $f_{\parallel}/f_{\perp} = 1.42$. This substantial departure from unity indicates a significant breaking of four-fold rotational symmetry characterized by an in-plane anisotropy whose modulations are stronger in the orbital's projection along the a-axis than along the b-axis. Some anisotropy might be expected due to the orthorhombic nature of YBCO's unit cell, but that would produce an inverse relationship for $f_{\parallel}/f_{\perp}$ between the H- and K-peaks. This isn't the case here, which suggests the dichotomous behaviour arises from electronic effects. In addition, the fit shows a not-insignificant out-of-plane modulation, with $f_{cc}/f_{\perp} = -0.15$. The possibility of this outcome has previously been neglected with f_{cc} often assumed to be zero, but our results suggest that this should not be taken for granted. Finally, we note that the measurements at $L \simeq 1.5$ and $L \simeq 1.3$ are consistent with the same scattering tensor, as evidenced by the ability of one fit to match both datasets.

With $f_{aa} > f_{bb}$, the scattering tensor does not reflect the point group symmetry of the CuO_2 planes. This is evidence that in addition to charge ordering, orbital ordering is also present. A contribution from the Cu-O chain layer that runs along the crystal's b-axis could potentially affect the symmetry of the scattering tensor in this way. However, the orbitals in the chain layer resonate at higher energy than in the plane, and studies exploring the energy dependence of the CDW peak haven't observed any such contributions.[65,102] Furthermore, the structure of the chains is sensitive to doping and temperature, but we have found no evidence that these properties affect the peak's azimuthal dependence (Figures 3.7 and 3.8, respectively). Instead, it would seem that the orbital ordering exists in the CuO_2 plane, alongside the charge ordering.

An Alternative Model of the Form Factor

By loosening the restrictions on our fitting model to explore solutions that include more nonzero f_{ij} components, we discovered additional fits that provide a similarly satisfying match to our H-peak data. In particular, we found favourable tensors with nonzero f_{ac} $(= f_{ca})$ components, which mix scattering with polarizations along the a- and c-axes. Such tensors (examples listed in Table 3.1 and plotted in Figure 3.7) imply the breaking of mirror symmetry around Cu sites along the ab- and bc-planes. One possible explanation for the origin of this properties could be a CDW in which unoccupied Cu $3d$ orbitals rotate about the b-axis. Following the work by Forgan *et al.*, who used non-resonant hard x-ray

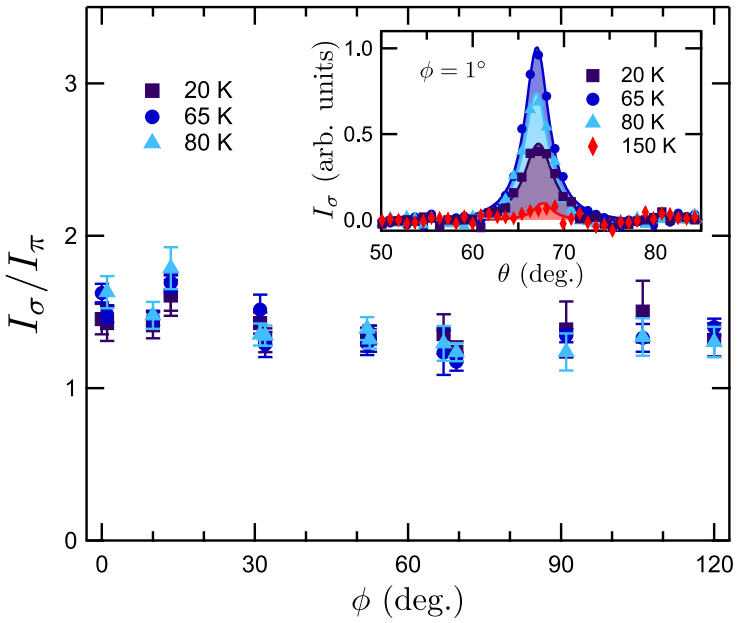

Figure 3.8: Measurement of the H-peak in YBCO-6.67 with $L = 1.32$ for a series of temperatures and azimuthal rotations, ϕ. The data overlaps within uncertainty and show no sign of a temperature dependence in the form factor. Inset: example CDW-peaks at $\phi = 1°$. At 150 K, the peak has faded into noise.

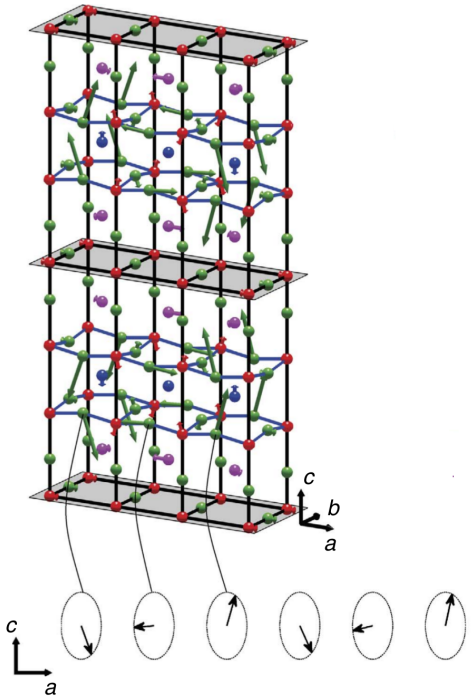

Figure 3.9: A model of ionic displacements caused by the CDW in YBCO, derived from hard x-ray scattering. Note the eliptical pattern as a function of distance along the a-axis. (Figure adapted from Ref. 142.)

scattering to measure small ionic shifts in YBCO (Figure 3.9), we propose a model CDW where ions are displaced by vectors that follow an elliptical pattern as a function of position along the a-axis (Figure 3.10). These shifts could cause a rotation of the Cu orbitals in response to the "kinking" of the CuO_2 plane, and they could induce charge modulations due to the changing distance that ions in the plane layer are from the reservoir of charge in the chain layer. These effects together may even produce a kind of orbital order as modulations in the environment around Cu affect the shape, or even occupied configuration, of the $3d$ orbitals, and thus this type of CDW shows potential for explaining a lot of the properties observed in our data. However, it is also important to note that more measurements are needed before the symmetry of the H-peak's scattering tensor can be uniquely determined.

Regardless of which tensor accurately describes the H-peak, the most curious aspect of our results is why the CDW order has a different symmetry at all along the a- and b-axes. In most aspects, the H- and K-peaks behave similarly. For example, they have a similar intensity, correlation length, temperature dependence, energy dependence, and pattern of

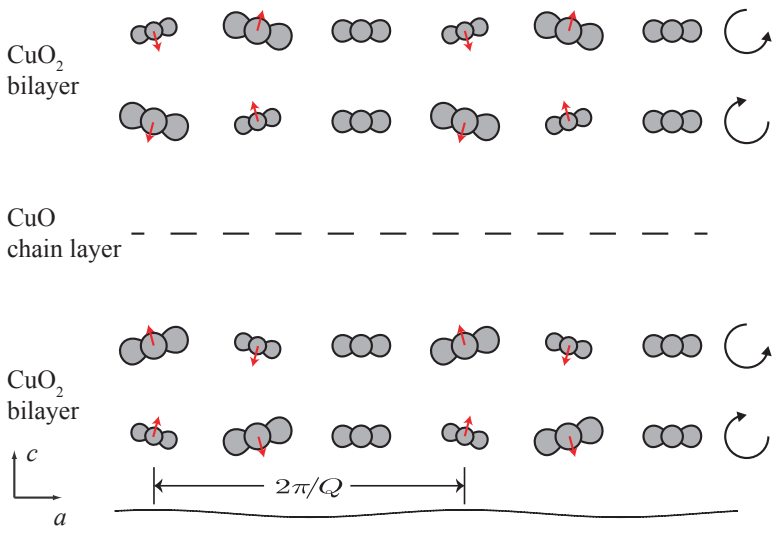

Figure 3.10: A proposed model of a CDW in YBCO that results in nonzero $f_{ac} = f_{ca}$ terms in the scattering tensor. Red arrows represent (exaggerated) ionic displacements, and the size of the orbitals correspond to the amount of charge on the ion. The orbitals change orientation in response to their ion's displacement, and they gain (lose) charge when pushed closer to (farther from) the chain layer, which acts as a charge reservoir. The displacements follow a rotating elliptical pattern with distance along the a-axis, which changes direction between neighbouring plane layers. (Figure adapted from Ref. 143.)

lattice displacement.[102,104,124,142] However, they also show a different relationship between intensity and doping,[104,124] and they respond differently to magnetic fields.[144] To understand these connections, more studies like our own are required that can further improve the accuracy of the CDW's symmetry in these and other cuprate samples.

3.4 Summary

The case for a universal d-symmetry of the CDW in the cuprates is gaining momentum from both theoretical studies and experimental evidence, but the symmetry is still unknown in many materials. Here, we have presented measurements from a novel resonant soft x-ray scattering experiment on three important cuprates: 1/8-doped LBCO and two dopings of YBCO. Contrary to expectations, we found that the CDW has a dominantly monopolar symmetry in LBCO, likely centred on the O sites of the CuO_2 plane. This was observed at both the O absorption edge and Cu. Specifically, we found at O $f_\parallel/f_\perp = 0.612$, $f_{cc}/f_\perp = 0.034$, and $\Delta_d/\Delta_{s'} = -0.241$. At Cu, we found $f_\parallel/f_\perp = 0.991$, $f_{cc}/f \perp= -0.067$, and estimations of the ratios of symmetry components that were definitively monopolar. We argued that this affinity for an s-like CDW may be related to the unique stripe order in the La-based cuprates. Specifically, in a case where ferromagnetism correlates with charge density, an SDW would be incompatible with a quadrupolar CDW. Furthermore, we discussed how a monopolar CDW may show greater competition with superconductivity than quadrupolar, as evidenced by the enhanced suppression of T_c in 1/8-doped LBCO.

In YBCO, two distinct symmetries were observed at the Cu edge. Examining the K-peak that corresponds to CDW order along the b-axis, we again observed a dominantly monopolar symmetry with $f_\parallel/f_\perp = 0.998$, $f_{cc}/f_\perp = 0.049$. We contrasted our experiment with a previous study that reported different conclusions but suffered from more ambiguity due to a less favourable geometry. At the H-peak, we were surprised to find anisotropy in the in-plane components of the scattering tensor that does not reflect the expected symmetry surrounding the Cu ions and suggests the presence of orbital order. We also noted that other models of the scattering tensor, specifically with nonzero $f_{ac} = f_{ca}$ components, could provide satisfying fits to the data. We proposed a novel CDW, based on hard x-ray scattering, that fit this tensor symmetry by exhibiting ionic displacements. However, our measurements could not uniquely determine the correct form of the tensor, and we argued for more measurements on these and other samples to investigate the questions left unanswered.

Chapter 4

Observing Electronic Nematic Order in the La-based Cuprates with Anisotropic Tensor Scattering

A characterizing feature of strongly-correlated fluids is a diverse array of phases that originate from broken symmetries. Superconductivity, charge-density wave (CDW) order, and spin-density wave (SDW) order—which break gauge, spatial, and time-reversal symmetry, respectively—are widely prevalent throughout the strongly-correlated electronic structure of hole-doped cuprates, but it is unknown if other, yet-to-be-discovered phases generically populate the common phase diagram of this material family. It has been predicted that spontaneous C_4 rotational symmetry-breaking of the electronic structure, refered to as electronic nematic ordering, may be one such missing phase.[72] This claim was bolstered by the discovery of electronic nematicity in the $4d$ perovskite and strongly-correlated superconductor $Sr_3Ru_2O_7$.[145] Since that time, electronic nematicity has also been observed in numerous Fe-based superconductors,[146–150] the topological superconductor $Cu_xBi_2Se_3$,[151,152] and at the interface between $LaAlO_3$ thin films and $SrTiO_3$ substrates,[153] which all suggests that electronic nematicity may be a common partner of unconventional superconductivity.

Some measurements of electronic nematicity in the cuprates have already been reported. In 2002, Ando *et al.* measured anomalous anisotropy in the in-plane[2] resistivity of $YBa_2Cu_3O_{6+\delta}$ (YBCO) and LSCO.[154] Some anisotropy is expected to occur in both of these materials due to weak orthorhombicity of their unit cells, as well as the presence

[2]Here, we use *in-plane* to refer to the a-b plane of the crystal's unit cell, which is parallel to the CuO_2 plane.

of conducting CuO chains running parallel to the b-axis in YBCO. However, the authors observed a striking temperature dependence that could not be explained simply by crystal structure. Furthermore, the anisotropy in YBCO exhibited a negative correlation with increasing oxygen content in the chain layer;[1] a surprising result since oxygen content increases the conductivity (and thus the contribution to the anisotropy) of the CuO chains. The authors concluded that the likely explanation for the origins of this behaviour comes out of electronic correlations, which could be consistent with the presence of an electronic nematic phase. Shortly thereafter, a body of neutron scattering measurements revealed in-plane anisotropy in YBCO in the vicinity of the pseudogap that could be explained by the existence of an electronic nematic phase with a transition temperature well above T_c.[155–158] Subsequent measurements of the Nernst effect in YBCO[159] and STM measurements of Bi2212[113] also supported this possibility. Most recently, Cyr-Choinière *et al.* performed a careful analysis of transport in YBCO and found compelling evidence for an electronic nematic phase, distinct from the anisotropic CDW phase, residing at dopings below the peak of the CDW phase boudary, $p < 1/8$, and with transition temperatures reaching as high as 250 K.[160] It now remains to be determined if such a phase can be reliably observed with other experimental techniques in these and other cuprates, at which doping and temperature ranges in the phase diagram it resides, and if the phase is generic to all cuprates or a special phenomenon in some specific materials.

4.1 The Electronic Nematic Phase

Before we continue, it is instructive to establish more precisely what it means for a material to posses an electronic nematic phase. The term *nematic* is borrowed from the theory of liquid crystals describing fluids composed of interacting particles that exhibit correlated structural phases somewhere between traditional solids and liquids. The simplest example of a liquid crystal is a system containing long, thin, rod-shaped molecules. At high temperature, the molecules exist in a state of liquid disorder with random positions and orientations. As the system is cooled and forced to condense, space is saved and free energy minimized through the loss of rotational freedom so that the molecules line up with their long axes parallel to one another. The system thus acquires a net average orientation, but it remains fluid such that the positions of the molecules remain completely uncorrelated.[2]

[1] At low temperatures, below a doping of $\delta \simeq 0.55$.

[2] The molecules are also able to rotate freely about their long axes. This is an important point for molecules lacking symmetry in the perpendicular plane. If there is sufficient asymmetry, the system can sometimes transition at a lower temperature into a second nematic phase where the 2D-projection of the

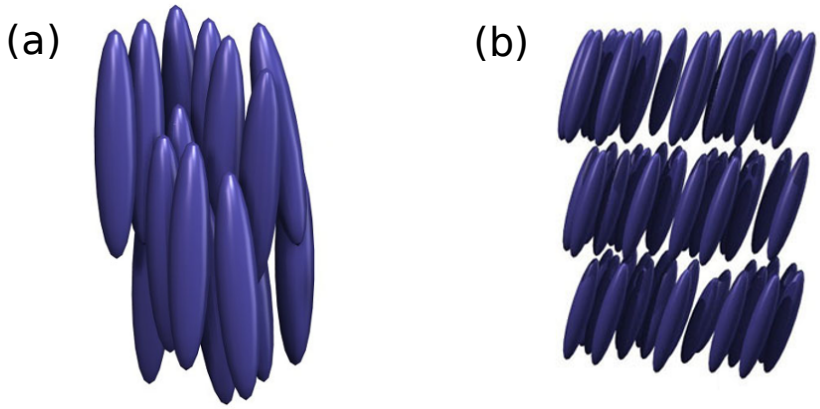

Figure 4.1: A fluid comprised of asymmetric particles, such as rod-shaped molecules, can align along a preferential axis below a threshold temperature to exhibit rotational order while maintaining spatial disorder in what is known as a nematic phase, (a). At lower temperatures, the particles can transition into a smectic phase where they arrange into layers with both rotational and spatial order, (b), shown here with a finite canting parameter. (Figures adapted from Wikipedia.)

This is known as a nematic phase and is illustrated in Figure 4.1(a). Clearly, some properties of a system in this state could differ when measured along the axis of alignment versus a perpendicular direction. A common example from daily life is a liquid crystal display (LCD). The fluids in these devices are opaque when disordered but become transparent along the direction of their aligned molecular axes when they enter the nematic state, which can be induced on-demand through the application of an electric potential.

As the system is cooled further, it can enter other ordered states. The smectic phase is realized when the molecules lose some spatial freedom and arrange themselves into layers perpendicular to the alignment axis, Figure 4.1(b). The system in this state has both rotational and spatial order defined by a single direction, but the molecules are still free to move and rotate in the perpendicular plane in which they remain disordered.

Electrons in solids are often treated like the particles of a fluid, and it is therefore perhaps unsurprising that the ordered phases of liquid crystals would be considered candidate states for some systems. However, even for classical fluids, the details surrounding the microscopic mechanisms that facilitate the formation of a nematic phase are challenging to quantify and generalize, and it is not immediately obvious how this theory,

system in the perpendicular plane will order for the same reasons as it did for the first nematic phase. Now, the system will have a fully-constrained average orientation but still have no spatial order.

which depends on polyatomic molecules with asymmetric structure, can be applied to electrons in a quantum mechanical context. One approach is to imagine the creation of a nematic phase from the melting of a stripe phase, such as CDW order.[72,161,162] Stripe order is classified as an electronic smectic phase, being a periodic structure that breaks rotational and spatial symmetry along a preferential axis. While transitioning out of this phase by increasing temperature, the stripes develop topological defects, i.e. dislocations in the CDW's 2D "crystal" of electrons, that break long-range spatial order. The initial macroscopic stripe pattern breaks apart into a sea of microscopic domains of local stripe order. At higher temperatures, the domains may be randomly oriented without any large-scale organization, but at moderate temperatures just above melting, the domains remain mostly aligned with one another. Thus, the melting occurs in such a way as to maintain an average rotational alignment of the stripe domains while their positions disorder due to the randomly-dispersed dislocations, and the CDW (smectic) order will have transitioned into an electronic nematic phase.

An alternative construction can be built from the perspective of the matieral's momentum structure. At high temperature, the material may be in a metallic state where disorder ensures a momentum distribution that only reflects the point group symmetry of the lattice. As pointed out by Pomeranchuk in 1958, if some of the Landau parameters describing the system are negative and sufficiently large to overcome the Fermi pressure, then the electrons will experience an instability and spontaneously lower their symmetry.[163,164] Precisely how the system evolves from this instability is complicated and depends on the details of the particular material, but in a simple case of a rotationally-symmetric (i.e. circular) 2D Fermi surface, the instability will cause an elliptical distortion.[165] Thus, when the temperature is lowered, the system will spontaneously break the symmetry of its momentum structure down to C_2 and develop anisotropy in properties that depend on orientation but not location. This is by definition an electronic nematic phase.

Identifying the presence of an electronic nematic phase from a measurement displaying asymmetry can be nontrivial. As implied above, anisotropy can arise from a number of other sources, such as an orthorhombic unit cell, asymmetric superstructures like 1D CuO chains, and the presence of other electronic phases like CDW order. Any of these will produce an orientation-dependence in a measurement like resistivity, but none meet the definition of electronic nematicity. One must therefore be careful that observed anisotropy is not attributable to other causes before making claims in this regard. To do so, a thorough knowledge of the crystal's structural and other electronic phases, as well as a clever measurement that avoids ambiguity, is often required. For example, one may need to find an anomalous dependence on doping or temperature,[154] or be able to carefully account for all other known sources of anisotropy.[160] Because of these stringent criteria, unfortunately,

the literature contains many credible reports of rotational symmetry breaking in the electronic structure of the cuprates that are ambiguous toward the observation of an electronic nematic phase (see Ref. 166, for example).

Finally, we note that many theoretical studies of nematic phases arising from Pomeranchuk instabilities in the cuprates and other correlated quantum materials have been performed over the past two decades.[167–177] For a thorough overview of electronic nematicity in strongly-correlated electronic systems, we refer the reader to Refs. 135 and 165.

4.2 The La214 Cuprates

The undoped parent cuprate is a Mott insulator that, upon doping, exhibits charge and spin correlations arising from a competition between Coulomb repulsion and kinetic energy as the extra charge carriers hop across the underlying antiferromagnetic lattice. How strongly structure, stoichiometry, and disorder in the lattice affects these correlations is of critical importance to understanding the emergence of ordered electronic states. Indeed, structural studies have always been of interest in the cuprates since the early proposal that Jahn-Teller polarons may be involved in an electron-phonon mechanism of high-T_c superconductivity.[178] While a lack of evidence for isotope effects in optimally doped cuprates now instead supports an electron-electron mechanism,[179] structural details have remained an important topic in cuprate studies.

Very relevant to the connection between lattice structure and electronic order is the La-based cuprates (known as La214), whose unit cell is organized in the K_2NiF_4 structure with CuO_2 planes separated by LaO rocksalt bilayers (Figure 4.2).[180,181] At high temperatures, the CuO_2 layers are parallel to the *ab*-plane of the unit cell, but a mismatch between the Cu-O and La-O bond lengths cause strain that is alleviated by structural distortions at lower temperatures. The undistorted state is known as the high-temperature tetragonal (HTT) phase, and upon cooling, the crystal can undergo a second-order transition into the low-temperature orthorhobmic (LTO) phase where the O octahedra coordinated around the Cu sites rotate about a vector 45° between the *a*- and *b*-axes.[131,180] As illustrated in Figures 4.3 and 4.4, neighbouring octahedra necessarily rotate in opposite directions to facilitate corner sharing, which produces a corrugation of the CuO_2 layers, and adjacent layers alternate their rotation vectors between the orthogonal but crystallographically-equivalent $[1\,1\,0]$ and $[\bar{1}\,1\,0]$ directions. Decreasing the temperature further, the crystal can then undergo another structural transition, this time first-order, into what is known as the low-temperature tetragonal (LTT) phase.[131,180,182] In this phase, the vector about which the octahedra rotate is now parallel to an in-plane crystallographic axis, alternating

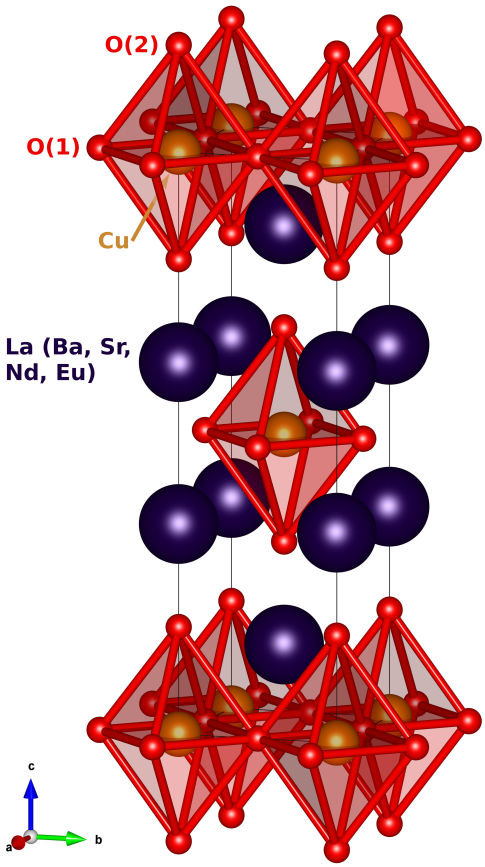

Figure 4.2: Crystal structure of the La214 cuprates. The unit cell is outlined in black, and the O octahedra surrounding the Cu ions are schematically framed in red. Bonds between atoms are not shown.

between a and b in adjacent layers. The magnitude of the tilt angle, usually defined as Φ, serves as a vectorial order parameter for both low-temperature phases, and while its magnitude increases as the HTT phase transitions into the LTO phase, only its direction changes substantially as the system changes into the LTT phase.

In the LTT phase, the fourfold rotational symmetry of the lattice in each ab-plane is reduced to twofold, and the structural distortion is known to correlate with the presence of static charge- and spin-stripe order in the CuO_2 planes.[61,118,129,183] Just like the structural rotations, the direction of the stripes run parallel to crystallographic axes, switching between a and b from one layer to the next. Indeed, in the infamous pseudogap doping region around 1/8 where the stripe order is the most robust and the superconducting dome is

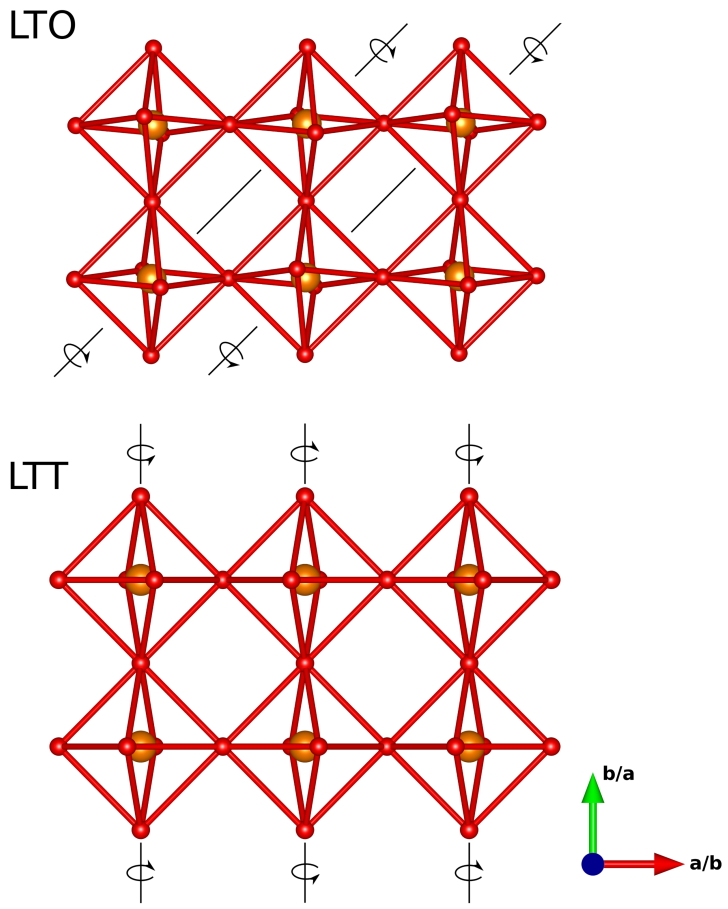

Figure 4.3: The CuO_2 plane layer of La214 in a "top-down view" along the perspective of the c-axis. In the higher-temperature LTO phase (top), the octahedra comprised of O ions coordinated around each Cu ion tilt along the [1 1 0] (or equivalent) crystal vector, with the direction of rotation (clockwise/counterclockwise) reversing between nearest neighbours. In the lower-temperature LTT phase (bottom), the rotation vector is along an in-plane crystallographic axis. For both phases, the tilting vector rotates 90° between planes neighbouring along the c-axis.

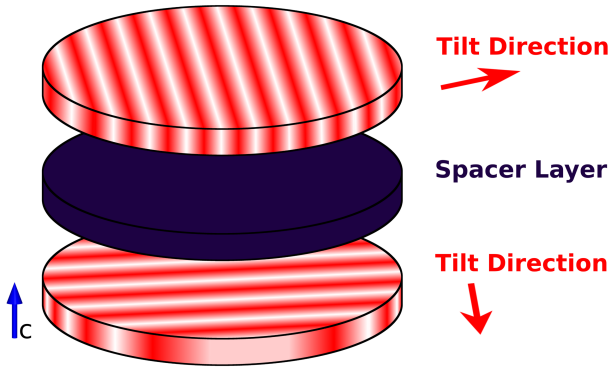

Figure 4.4: The orientations of the structural distortions in the low-temperature phases of La214 change orientation by 90° between adjacent layers. The charge- and spin-stripe order, which is thought to be stabilized by the in-plane anisotropy of the LTT phase, does the same.

maximally suppressed, the onset of long-range charge ordering is coincident with the LTT transition in LBCO (Figure 4.5), suggesting that the structurally-provided anisotropy may encourage—or at least permit—the formation of electronic stripe order.[118] However, the structure can be reverted back into the HTT phase at low temperature through the application of pressure, and the presence of charge ordering has been observed to persist.[184] Thus, the link between structurally-provided anisotropy and stripe order remains an open and interesting problem. With both a structural distortion and a charge-density wave providing a manifestation of C_4-symmetry breaking, the La214 family of cuprates should be a particularly strong candidate for the observation of an electronic nematic phase. Furthermore, with the variety of available dopants—Ba and combinations of Sr plus rare earths[183]—that can be used to tune parameters like the LTT, CDW, and superconductivity onset temperatures, we expect it to provide a rich playground for exploring the interplay of electronic and structural nematic phases.

We finish this section by briefly noting that the structural phase diagram of the La214 cuprates is actually more complicated than the description just provided. As shown in Figure 4.5 for LBCO, doping plays an important role in deciding if and at what temperatures the crystal will transition, and phases other than the ones described above are also possible. For example, the low-temperature less-orthorhombic (LTLO) phase, sometimes referred to as the LTO2 or Pccn phase to reflect its symmetry, can exist as an intermediate state between LTT and LTO where the octahedra are rotated intermediately between the two structures.

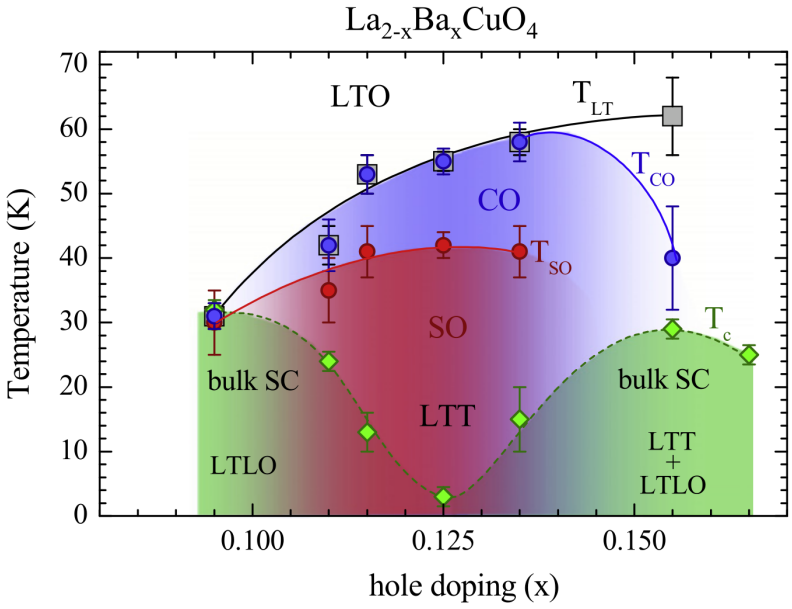

Figure 4.5: Phase diagram of La214 doped with Ba in the vicinity of the 1/8 anomaly. (Figure is adapted from Ref. 118.)

4.3 ATS Scattering

As shown in Figure 4.2, the unit cell of the La214 cuprates contains two CuO_2 layers, one at $z = 0$ and one at $z = 0.5$ (r.l.u.). The 0.5 layer is offset by $(x, y) = (0.5, 0.5)$, but the layers are otherwise equivalent in the HTT phase. Thus, the (0 0 1) Bragg reflection, which depends only on the ionic positions in z, will consist of identical reflections from the two layers, but with the $z = 0.5$ layer π out of phase with $z = 0$. As a consequence, the two reflections will interfere completely destructively, and the Bragg peak is said to be forbidden. However, the situation changes when C_4-symmetry is broken in the LTT phase, and a significant (0 0 1) signal can be observed when the measurement is tuned to atomic resonances.[185,186] As explained in Section 2.3, RSXS provides the ability—via careful selection of the energy and polarization of the incident beam—to acquire near-exclusive sensitivity to a particular orbital in the unit cell, and thus it changes the focus of the measurement from the periodicity of the ionic lattice to periodicity in the electronic structure. For example, measuring at the K edge of the apical O sites (O bonded to Cu above and below the CuO_2 plane), Fink *et al.* demonstrated that the non-zero intensity of the resonant (0 0 1) peak can be used to measure the presence of the LTT structural distortion and examine its onset below the LTO phase.[129]

The permission of the (0 0 1) peak on resonance arises from anisotropy in the local bonding environment surrounding each atom. The shift in ionic positions due to the tilted octahedra, which occurs on the order of a couple degrees,[187,188] slightly compresses and extends bond lengths throughout the unit cell. While this has a very small effect on the intensity of conventional diffraction, it induces local anisotropy in the electronic structure between the two in-plane crystallographic directions that can easily be detected in resonance studies. Since the orientation of the structural tilt rotates by 90° between layers, the profile of the anisotropy is similarly rotated for a translation of $z \pm 0.5$ in the unit cell. Thus, a scattering signal measuring the projection of an anisotropic orbital along an in-plane direction—selected by pointing the incident beam's polarization parallel to the crystal's *a*- or *b*-axis—differs significantly between layers, and the condition of total destructive interference is removed. Since this phenomenon arises from an anisotropic symmetry of the resonant scattering tensor, it is referred to as an example of Anisotropic Tensor Scattering (ATS).[186]

We can explicitly calculate the intensity of the (0 0 1) peak from the presence of in-plane anisotropy. Particularly instructive is the case of Cu, whose ionic positions don't change between the three structural phases. The structure factor for Cu is given by

$$S(0\,0\,1)_{Cu} = F(z=0) + e^{i\pi}F(z=0.5) \tag{4.1}$$

where

$$F(z) = \begin{bmatrix} f_{aa}(z) & 0 & 0 \\ 0 & f_{bb}(z) & 0 \\ 0 & 0 & f_{cc}(z) \end{bmatrix} \tag{4.2}$$

is the average atomic scattering form factor for Cu atoms with $z \in \{0, 0.5\}$. For conventional scattering, $F(z=0) \simeq F(z=0.5)$, and the structure factor vanishes. On resonance, however, the elements of the form factor become dominated by the local environment, as described in Section 2.3.1. We define a new quantity

$$\eta = f_{aa}(z=0) - f_{aa}(z=0.5). \tag{4.3}$$

Noting that the symmetry of the rotation between layers implies $f_{bb}(z=0) = f_{aa}(z=0.5)$ and $f_{bb}(z=0.5) = f_{aa}(z=0)$, we thus have

$$\eta = f_{aa}(z=0) - f_{bb}(z=0), \tag{4.4}$$

and clearly η represents the degree of in-plane anisotropy for the Cu $3d$ orbitals. We can then also write

$$I(0\,0\,1)_{Cu} \propto \left| \vec{\epsilon}'_f \begin{bmatrix} \eta & 0 & 0 \\ 0 & -\eta & 0 \\ 0 & 0 & 0 \end{bmatrix} \vec{\epsilon}_i \right|^2, \tag{4.5}$$

and therefore the square root of the intensity of the (0 0 1) peak measured at the Cu edge, with polarization of the incident beam along the a- or b-axis, directly measures the anisotropy factor η (up to a proportionality prefactor) and quantifies the amount of electronic nematicity in that orbital in the sample.

4.4 Experimental Results and Discussion

ATS scattering of the (0 0 1) Bragg peak was measured in a collection of La214 cuprates over a series of experimental runs at the REIXS beamline of the Canadian Light Source synchrotron in Saskatoon (described in Section 3.1). The samples were grown using the travelling solvent floating zone method, and a brief verification of their crystallographic integrity and orientation was performed on each before being sent to the synchrotron. Before starting each experiment, a fresh surface was exposed by a top-post cleave[1] in air shortly before loading the sample into the vacuum chamber, and the experiment was performed in a pressure of approximately 10^{-10} Torr.

Each sample was mounted with conductive, UHV-compatible silver epoxy such that the a/b-plane was parallel to the surface of the sample holder and the c-axis was antiparallel with the incident beam when $\theta = 0°$. Its in-plane axes, which are equivalent in the La214 structure, were positioned parallel and perpendicular to the scattering plane (horizontal and vertical in the laboratory frame, respectively). After entering the vacuum chamber, the samples were moved into the diffractometer's center of rotation, and a fine calibration of the rotation motors to correct errors in mounting was performed using multiple Bragg peaks as references. Two of the strongest and most easily accessible peaks were the (0 0 2) and ($\pm$1 0 3). For the dimensions of the unit cells in the La214 cuprates, the (0 0 2) peak can be found near the Cu L edge where the beamline's energy is reliably calibrated. However, the ($\pm$1 0 3) needs energies above $\sim$ 2 keV, and the beam required a secondary calibration. The experiment was subsequently performed primarily using π-polarization (vertical $\vec{E}$-field) to ensure maximum overlap with the projection of orbital components along an

[1] A top-post cleave is performed by gluing a small object—often a screw or other piece of clean hardware lying around the laboratory—to the surface of the sample. Ideally, the connected surfaces should be roughly equal in size and shape to produce the best cleave. The top-post is then struck abruptly from the side with the hope that the shearing, torquing force at the connection point breaks the sample along a simple crystallographic plane approximately parallel to the glued surfaces. In materials like the cuprates, top-post cleaving is highly successful, especially when exposing the ab-plane since the bond along the c-axis between unit cells is comparatively weak. Ultimately, though, the quality of the cleave is never guaranteed in any material, and is not uncommon to have to repeat the procedure two or more times before the sample is ready for measurement.

in-plane crystallographic axis, as using σ-polarization would mix the overlap with c-axis components for $\theta > 0°$.

4.4.1 Group I Samples

Our samples were measured periodically over the course of a few years and, for the convenience of our narrative, can be divided into two groups. The first group contains three samples: $La_{1.875}Ba_{0.125}CuO_4$ (LBCO(i)) that is critically doped to the peak of the pseudogap at $p = 1/8$; $La_{1.475}Nd_{0.4}Sr_{0.125}CuO_4$ (LNSCO(i)) also with $p = 1/8$; and $La_{1.65}Eu_{0.2}Sr_{0.15}CuO_4$ (LESCO) with $p = 0.15$. The first two differ from the last by carrier concentration, and all three differ in ionic spacing due to the varying diameters of the dopants. Note that in $La_{2-x-y}RE_ySr_xCuO_4$, Sr dopes holes while the rare earth (RE) only affects inter-atomic spacing. Consequently, the samples have different LTO-to-LTT and CDW transition temperatures (T_{LTT} and T_{CDW}, respectively) as verified in our results below, making them interesting subjects for our experiment. The locations of the Bragg peaks were recorded assuming lattice parameters $a = b = 3.787$ Å and $c = 13.24$ Å for LBCO(i) and LNSCO(i), and $a = b = 3.79$ Å and $c = 13.14$ Å for LESCO, which were taken from the literature and correspond to the unit cells of the HTT phase.[9,118,128–131]

The presence of the (0 0 1) peak in each sample was verified and examined. As expected, the peak was found to appear only at low temperature and to have decayed into background noise before the sample was heated to 150 K. In addition, the peak only appeared on resonance with an absorption edge. To illustrate this second property, Figure 4.6 provides energy scans taken through the O K and Cu L_3 edges at a constant scattering vector $\vec{Q} = (0\,0\,1)$ in LBCO(i) at high (red) and low (blue) temperatures. The extra intensity at low-temperature can be isolated by taking the difference (green), and it is roughly attributable to the presence of ATS scattering. It should be noted that due to the large variation in the refractive index as a function of energy when passing through an absorption edge, the green spectrum is also significantly influenced by changes in the position of the (0 0 1) peak that are unaccounted for here and effectively misalign the detector. A more precise determination of the energy dependence would involve optimizing the peak's position at every data point, such as was preformed in Ref. [9, supplemental]. However, this exercise still provides an approximate energy profile that is sufficient for demonstration here and is often used in practice used for preliminary sample calibration.

As can be seen in Figure 4.6, ATS intensity is present throughout the pre-edge region for both elements, with a strong, single peak present just below the XAS resonance peak for Cu. For O, the complexity of the K edge XAS is mirrored by a more complicated

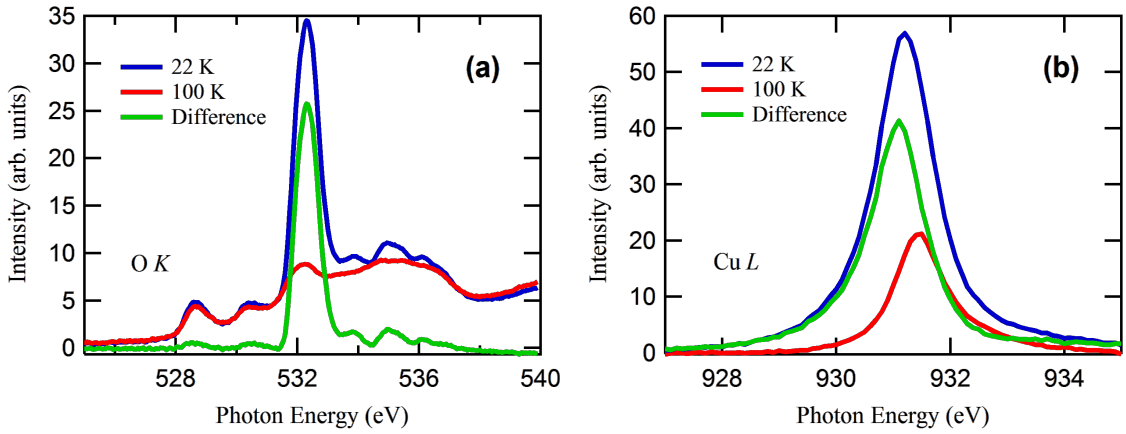

Figure 4.6: Energy dependence of the (0 0 1) peak at the O K (a) and Cu L (b) edges in LBCO(i). Measurements were taken at 22 K (blue) and 100 K (red). The difference (green) crudely approximates the ATS scattering signal (see main text for details). Note that the background intensity has been removed from all spectra with a constant offset for clarity.

ATS signal with a dominant peak between 532 and 533 eV and minor peaks distributed throughout the rest of the edge. For our purposes, we need only take note from the literature that unoccupied states composed of in-plane O $2p_{x(y)}$ orbitals hybridized with Cu $3d_{x^2-y^2}$ orbitals dominate the XAS intensity of the O K edge at 528.5 eV (the mobile carriers near ε_F), and apical O states hybridized with spacer-layer orbitals dominate the intensity at 532.2 eV.[129,189] We therefore recorded the ATS peaks at these two energies in the O edge to explore the nematicity of the in-plane and apical orbitals, respectively.

We then began a careful series of measurements of scattering intensity as a function of reciprocal space position for a range of temperatures. Specifically, we tuned our beam energy to each of the accessible absorption edges of interest in the material and rotated our system along L through the (0 0 1) peak. This is achieved with a so-called "θ-2θ" scan, whereby the ratio of the sample angle θ and detector position 2θ are held constant. At a (0 0 L) peak, the Bragg condition is satisfied simultaneously with specular reflection ($\theta = \frac{1}{2} \cdot 2\theta$), and a θ-2θ scan is required to separate the two signals. Count rates were recorded in most cases with the Channeltron to avoid detector broadening that resulted with the MCP. Example series are shown in Figures 4.7 and 4.8 for the La M_5 and Cu L_3 edges in LESCO, respectively. For each temperature in the series, the background—which varied due to the effect of the changing θ and 2θ angles on the XAS signal (see Section 2.1.3)—was subtracted by fitting the spectrum in the regions above and below the peak with a polynomial. A

fifth-degree polynomial was used in most cases because of its favourable profile, but we note that other choices ranging from third to sixth produced nearly identical results. As demonstrated in Figure 4.7, typical background spectra showed small variations relative to the lowest-temperature (0 0 1) peak, and thus to a good approximation, the primary effect of the background subtraction was the removal of a constant offset.

Post background subtraction, the data was fit to a Lorenztian (Figure 4.8(a)) of the form

$$\mathcal{L}(x) = y_0 + \frac{A}{1 + 4\left(\frac{x - x_0}{\mathrm{FWHM}}\right)^2} \tag{4.6}$$

where A is the peak's amplitude, $y_0 (\approx 0)$ its vertical offset, x_0 the location of the peak, and FWHM its full-width at half-maximum. These parameters, as well as the calculated area of the peak, were recorded and used to characterize the influence of beamline fluctuations and other perturbing effects on the accuracy of the results.

It was found in the course of our measurements that jitter and drift in the beamline's parameters during normal operation produced various small but significant anomalies in the spectra. This was due in part to the difference in the energy-positions of the ATS and XAS peaks that meant our measurement was necessarily sitting on the sloping shoulder of one peak or the other regardless of the targeted energy value we chose to use. Thus, a small change in a parameter like the position of the beamspot on the monochromator, for example, could result in a significant change in the sample's background fluorescence. We therefore needed to implement a rigorous calibration procedure that was performed between each recorded spectrum in the series where the sample's position, orientation, and EY energy-profile was corrected to an initially defined setpoint. While this stabilized the amplitude and shape of the peak, and thus greatly improved the experiment's accuracy, it also produced a small problem. As seen in Figure 4.7, and to a lesser extent Figure 4.8(a), a secondary peak of lower intensity laid hidden under every (0 0 1) peak. This was determined to be the non-forbidden (0 0 2) reflection resulting from second-order light (twice the setpoint energy) that is unavoidably produced in the undulator and is not filtered out by the monochromator. The relative intensity of this peak changed with the setpoint energy—the strongest peak appearing at the O edge. Due to the large fluctuations in a crystal's refractive index near resonance (Section 2.1), the first- and second-order beams refract differently at the sample's surface and thus appear at slightly different detector positions. Unfortunately, our calibration procedure could not always immediately determine which peak position corresponded to the (0 0 1) and sometimes added erroneous drift to our record of L_0; particularly at temperatures where the (0 0 1) is comparable in size to the (0 0 2). This proved quite annoying during the experiment, and though post-experiment

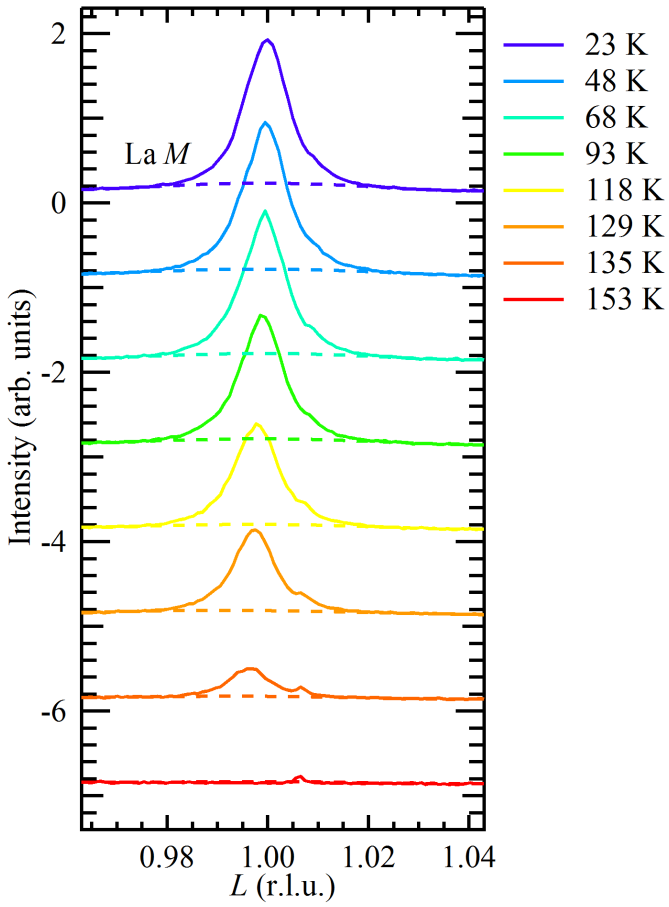

Figure 4.7: Temperature dependence of the (0 0 1) peak at the La M edge in LESCO (solid lines). Backgrounds have been fit with a polynomial (dashed lines). Notice the appearance of the smaller (0 0 2) peak due to second-order light from the undulator as the (0 0 1) dies away. The refractive index varies strongly at resonances, which causes the (0 0 2) to appear as if it occurs at a different point in reciprocal space.

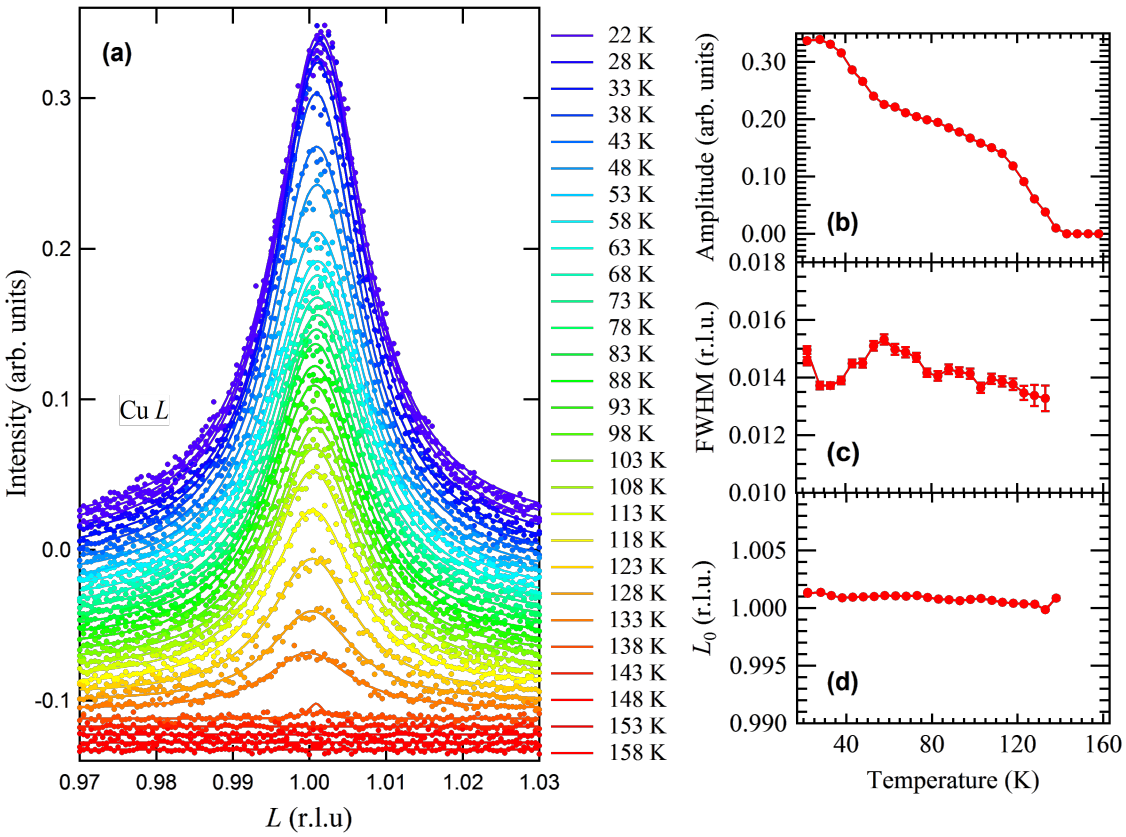

Figure 4.8: Temperature dependence of the (0 0 1) peak at the Cu L edge in LESCO. (a) Peak profile in reciprocal space after the backgrounds have been removed. Data (dots) are fit to a lorentzian (lines). The intensity (b), full-width at half maximum (c), and peak location (d) of the fit are shown. L_0 is corrected for refraction. Nonsensical points were omitted once the intensity fell below noise.

analysis on the data set as a whole could account for it, some small errors may still persist at one or more data points in the vicinity of the "cross-over."

It should be noted that while the FWHM of the CDW peak is inversely proportional to the correlation length of the CDW order (see below), this is not the case for the (0 0 1) peak and the LTT order. The intensity of the reflection can be modelled in the dynamical diffraction framework as[9,96]

$$I(\vec{Q}) = \frac{|\hat{S}(\vec{Q}\,')|^2}{(\frac{\pi L}{B} - \mathrm{Re}[\hat{S}(0)])^2 - \mathrm{Im}[\hat{S}(0)]^2} \tag{4.7}$$

where B is a constant related to the geometry of the unit cell, $\hat{S}(\vec{Q}\,')$ is the structure factor at wavevector $\vec{Q}\,'$ calculated inside the material (differing from $\vec{Q}$ in vacuum due to the refractive index), and $\hat{S}(\vec{Q} = 0)$ corresponds to diffraction at the low-angle limit. Both factors in the denominator are proportional to the absorption coefficient, μ, and

$$I(\vec{Q}) \propto \frac{|\hat{S}(\vec{Q})|^2}{\mu^2} \tag{4.8}$$

and

$$\mathrm{FWHM} \sim \mu \tag{4.9}$$

in the strong-absorption limit. We would therefore expect our measurements of the FWHM to stay constant as a function of temperature. As verified in Figure 4.8(c), this was essentially the case across our measurements, with some small modulations from noise and beamline fluctuations.

Figure 4.9 shows a summary of our results for the intensity of the (0 0 1) peak as a function of temperature in our first group of samples at various edges: Cu L_3, Eu M_5, La M_5,[1] in-plane O K (528.5 eV), and apical O K (532.3 eV). The spectra for each material have been normalized to an intensity of 0 and 1 in their limits of high and low temperature, respectively, so that the absolute intensity of each peak, which depends on the resonant form factor, can be ignored. The most obvious pattern that emerges is the dichotomous behaviour between the edges that correspond to the CuO_2 planes (Cu and in-plane O) and the edges associated with the $(La,M)_2O_2$ spacer layer. The LBCO(i) data (4.9(a)) provides the clearest example. The La and apical O curves collapse onto one another with striking similarity and exhibit an abrupt, first-order increase in intensity at T_{LTT}, followed by a gradual increase with decreasing temperature. This behaviour tracks conventional

[1]Substantial intensity from ATS scattering was available for a broad range of energies surrounding the La edge. To minimize noise and second-order light, spectra were taken 10 eV below the XAS edge.

hard x-ray measurements of the (1 0 12) Bragg reflection that is directly sensitive to the LTT/LTO structural distortion,[190] and is consistent with other conventional x-ray and neutron measurements near the transition.[118,128,191] It therefore appears as though the intensity at these edges is proportional to the extent of the structure-induced anisotropy, as expected. The in-plane Cu and O edges, on the other hand, initially exhibit a similar behaviour with an abrupt increase in intensity as the temperature falls below T_{LTT}, but the subsequent increase as the temperature continues to fall is remarkably slower. Changes to the ATS peak intensity due to the structural shift is expected to affect all of the edges identically (up to a proportionality factor), but we instead see a clear distinction arise between edges based on their location in the unit cell. Thus, we must conclude that the origin of the dichotomy is not structural but intrinsically electronic, and we assert that this is compelling evidence for the presence of an electronic nematic state forming in the orbitals of the CuO_2 plane.

Comparing Figure 4.9(a) with (b) and (c), we see a similar pattern in LESCO and LNSCO(i), respectively. Again, the strength of the spectra from edges associated with the CuO_2 planes lag behind those from the spacer layer after the initial onset at T_{LTT}. In LESCO, we see that the La and apical O edges match one another closely, as do the Cu and in-plane O edges with some deviations that are likely attributable in whole or in part to beamline instability. However, Eu stands out from the other spectra with an even more first-order-like dependence that sees its intensity rise to a maximum shortly below T_{LTT}. The origin of this unique behaviour is not immediately clear, but we note that it still shares the qualitative description of exhibiting a faster rise below T_{LTT} than seen in the in-plane elements. In LNSCO(i), the dichotomy is clearly apparent between Cu and apical O in solidarity to the other samples. However, time constraints limited our data collection to these two spectra only, and we therefore cannot comment on their correlation with other edges in the material.

It should be noted here that our choice of temperatures at which the spectra were normalized, especially the low temperature, was somewhat arbitrary. The data is not meant to be presented in such a way as to imply that the degree of anisotropy converges as $T \to 0$. On the contrary, it may be the case, for example, that the anisotropy is comparable for all edges in the transition region around T_{LTT} where structural contributions dominate, after which the spectra of the plane layer exceed those of the spacer layer as the temperature decreases and anisotropy develops from strong electronic correlations. This scenario is supported by the intuition that the electronic nematic phase would become more robust with decreasing temperature, and thus the ATS intensity in the plane layer would diverge monotonically from those of the spacer layer. However, one might then also expect the plane layer and spacer layer curves to overlap well at the transition with proper scaling,

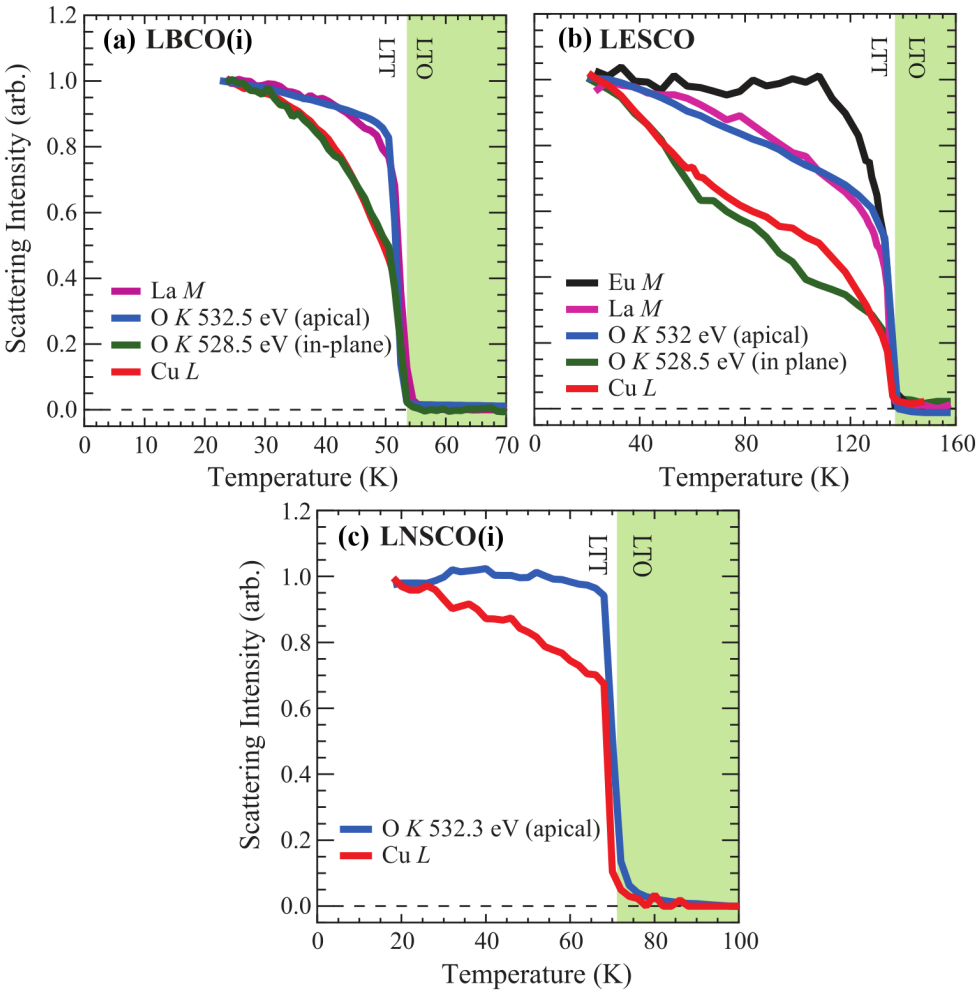

Figure 4.9: Temperature dependence of the ATS scattering intensity in (a) LBCO(i), (b) LESCO, and (c) LNSCO(i) at various resonant edges. While the edges associated with the spacer layer follow the trend of the structural transition, those associated with the CuO_2 planes exhibit additional anisotropy originating from electronic interactions. We believe this is strong evidence for the presence of an electronic nematic phase. (Data is normalized at high and low temperature to 0 and 1, respectively. Figure is adapted from Ref. 9.)

which they arguably do not. Whatever the case, however, the most important insight revealed by these measurements is the clear difference in shape between the two categories of spectra; a difference that cannot be understood as a direct consequence of the structural transition, but rather seems to arise out of electronic interactions.

For further confirmation that the features in our data are indeed the result of electronic anisotropy, we modelled the intensity of the (0 0 1) peak at the Cu L_3 edge that the expected nematic scattering form factor in Equation 4.5 would produce and compared it to our results. To remove the complicating effects of absolute intensity, experimental aberrations, and scattering geometry, we followed a similar procedure to the one outlined for the experiments in Chapter 3 and recorded the ratio of intensities using σ- and π-polarized incident beams. As shown by the red curve in Figure 4.10, the ratio from the nematic form factor is expected to oscillate as a function of azimuthal angle, ϕ, due solely to geometric effects. Since the measurement along either in-plane crystallographic axis is expected to be proportional to the square of the anisotropy—a constant—then the ratio should vary as ϕ is rotated and the crystallographic projection of each polarization changes. When the crystallographic axes are square with the laboratory frame, then σ-polarization is parallel to the vertical crystal axis, while π-polarization is at some angle to the horizontal axis due to a finite θ, and the ratio experiences its minimum. Later, when the crystal is rotated $\pm 45°$, the two polarizations are maximally misaligned and produce comparable intensity, and the ratio experiences its maximum close to unity. Our data closely matches this model (black dots), which is especially convincing when one considers that the fitting model contains no free parameters to optimize. For comparison, we also included two other relevant models of the Cu edge. [9, supplemental] The green curve would result from in-plane modulations of the position of charges in neighbouring CuO_2 planes, represented by the scattering form factor

$$I(0\,0\,1)_{Cu} \propto \left| \vec{\epsilon}'_f \begin{bmatrix} 1 & 0 & 0 \\ 0 & 1 & 0 \\ 0 & 0 & 0.1 \end{bmatrix} \vec{\epsilon}_i \right|^2 \tag{4.10}$$

where we have assumed an occupation ratio of the $3d_{3z^2-r^2}$ to $3d_{x^2-y^2}$ orbitals of 10%; and the blue curve would result from antiferromagnetic ordering of the magnetic moment projected along the c-axis, represented by

$$I(0\,0\,1)_{Cu} \propto \left| \vec{\epsilon}'_f \begin{bmatrix} 0 & 1 & 0 \\ -1 & 0 & 0 \\ 0 & 0 & 0 \end{bmatrix} \vec{\epsilon}_i \right|^2 . \tag{4.11}$$

Of the three models, clearly only the nematic scattering form factor accurately represents our results, and does so convincingly.

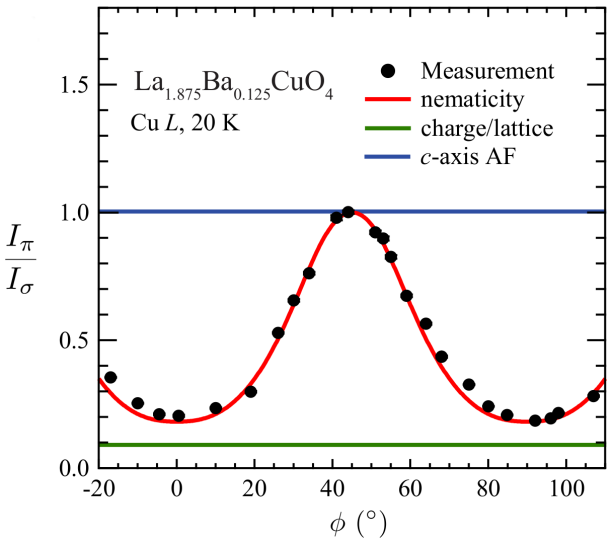

Figure 4.10: The ratio of the ATS peak intensity measured with π- and σ-polarization ($\vec{E}$-field parallel and perpendicular to the scattering plane, respectively) is plotted with black dots. The intensity is modelled using the nematic scattering form factor from Equation 4.5 (red line), as well as two alternative candidates for the form factor from Equations 4.10 and 4.11 that describes charge modulations (green line) and antiferromagnetic ordering (blue line). (Figure is adapted from Ref. 9.)

The Charge Ordering Peak

The CDW peak was examined using a similar procedure as for the (0 0 1). The peak is known to occur at $\vec{Q} = (\pm 2\delta\ 0\ \ell \pm 0.5)$ and $(0\ \pm 2\delta\ \ell \pm 0.5)$ where 2δ depends on doping (x), and ℓ is an integer. It has been empirically determined that δ roughly follows x below the pseudogap maximum of $x = 1/8$. However, while it was once thought that 2δ then saturated at 1/4—the most obvious periodicity for the stripe order model[61]—more detailed neutron and x-ray diffraction studies now often report a slightly different value; one that depends on the material and continues to change modestly as x increases past 1/8.[8,9,67,123,129,192,193] In LBCO, for example, Hücker *et al.* have reported that across the doping range $0.095 \leq x \leq 0.155$, 2δ shifts monotonically from 0.205 to 0.245.[118] For our measurements, the $(H\,0\,L)$-peak was found to occur at $H = 2\delta = -0.238, 0.264, 0.236$ for LBCO(i), LESCO, and LNSCO(i), respectively.

The peak's profile in energy and reciprocal space was checked for consistency against past experiments.[8,67,129] As illustrated in Figure 4.11, the peak was seen at the Cu L and O K resonant edges with a maximum in its energy dependence slightly below (< 1 eV) that of the XAS, as expected. The peak's L-dependence was similarly examined from the difference in spectra taken at high and low temperature. As seen by the rough profile in Figure 4.12(a), the maximum occurred near the expected value of $L = 1.5$. A more precise profile was also measured by scanning through the peak along H at a series of fixed L values, Figure 4.12(b). The backgrounds (dashed lines) were fit to the regions surrounding the peak and subtracted to remove the effects of the changing geometry, and the same location for the maximum was found at 1.5. Using either approach, the data clearly indicates that the peak is broad in L and does not require a precise alignment along that reciprocal space coordinate. All of these features are hallmarks of the CDW ordering peak in the La214 cuprates, and verify our expectations.

A temperature series was collected at the Cu resonance in each sample, with individual measurements consisting of scans of the θ-motor position while the detector remained stationary. Unlike the measurements of the ATS peak that cut only along L, this procedure recorded a shallow arc through the H/L-plane of reciprocal space that provided a wide, stable cut along H with a modest, monotonic spread along L. Measurements were recorded with the MCP which, due to its larger collection area, significantly increased count rates and reduced noise levels when compared to the Channeltron. The background was again removed by fitting a polynomial to the regions outside the peak; this time improving the isolation of the peak far more dramatically than the case of the ATS measurements, as the maximum peak-intensity was far smaller compared to the varying background (Figure 4.12(b)). The resulting data was then fit with a Lorentzian of the same form and

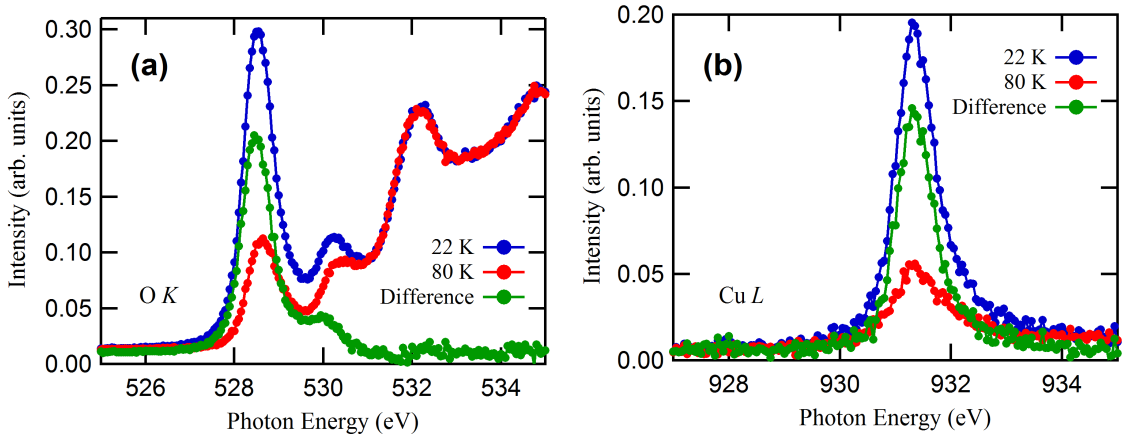

Figure 4.11: Energy dependence of the CDW peak at the O K (a) and Cu L (b) edges in LBCO(i). Scans were taken at 22 K (blue) and 100 K (red). The difference (green) is an estimate of the CDW peak intensity with the resonant XAS effects removed. Scans have been aligned vertically for clarity.

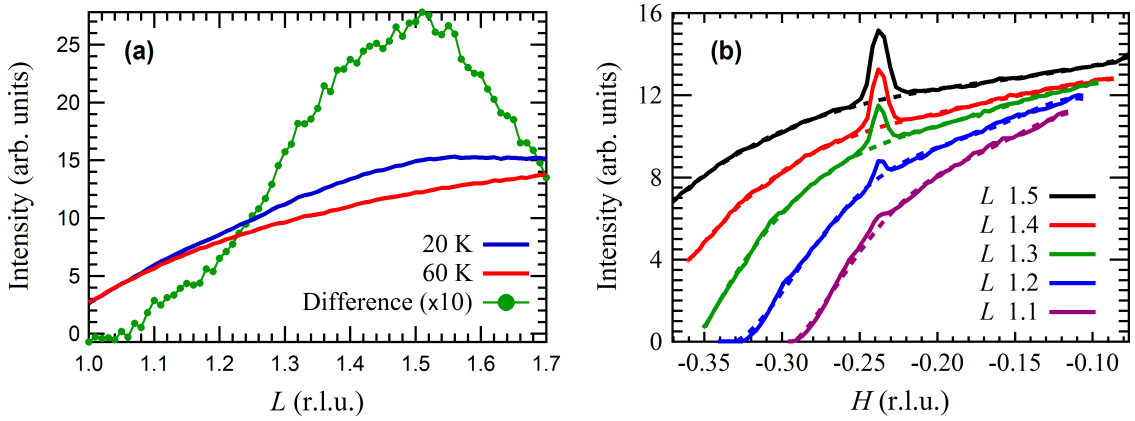

Figure 4.12: The L dependence of the CDW peak was measured at the Cu L edge in LBCO(i). (a) A set of scans at constant $(H, K) = (-0.238, 0)$ and varying L were measured at 22 K (blue) and 60 K (red), and the difference (green) was taken to provide an approximate, continuous profile of the peak with the fluorescent background removed. (b) θ-scans were taken at varying values of L (solid lines) to obtain a higher-quality profile. Backgrounds were fit to a polynomial (dashed lines).

characterizing parameters as before.

Example results for LBCO(i) with the measured amplitude, FWHM, and peak location along H are shown in Figure 4.13. The markedly weak intensity—typical of CDW peaks in La214—resulted in modest error bars, but the fits still matched the data closely and unambiguously for temperatures below T_{CDW}. Consistently across the three samples, we found an intensity that decayed with temperature through a second-order transition. In addition, the peak's position H_0 remained extremely stable with temperature, erroneously drifting only as the peak became lost in the background noise. Finally, the FWHM began with a constant value at low temperature where the peak was likely broadened by the detector before moderately increasing as the sample warmed. This trend was expected as the CDW order should become less stable, reduce its correlation length, and thus increase the width of its diffraction peak as the sample transitions toward the high-temperature symmetric state.

Figure 4.14 presents the intensity of the CDW peak for each sample as a function of temperature alongside our measurements of the in-plane ATS peak-intensity, all taken at the Cu L edge. The spectra were again normalized to values of 0 and 1 at high and low temperature, respectively, to enable a direct comparison. In essence, this figure depicts the relationship between the intra- (ATS) and inter-unit cell (CDW) symmetry breaking in the Cu $3d_{x^2-y^2}$ orbitals. As discussed in Section 4.2, there is generally a strong connection between the two symmetries in La214. It is empirically well-established that the first-order LTT/LTO transition often coincides with the onset of the second-order CDW transition, as it does here for LBCO(i) and LNSCO(i). Furthermore, it has been witnessed at some dopings that the CDW order undergoes a coincidental first-order transition at T_{LTT} before resuming its typical, gradual climb in intensity with decreasing temperature. This suggests that the CDW order would persist at higher temperatures if the LTT structure did as well, and it may not be present at all without it.[118,194] All of this evidence seems to support a hypothesis that the two phases are cooperatively related, and conditions producing the presence of one in a material could boost the onset temperature or intensity of the other. This line of thinking is furthered by our results for LESCO where the interesting case exists of CDW order onsetting well below the LTT/LTO transition. Strikingly, the in-plane ATS peak experiences an increase in its slope as the temperature is lowered past T_{CDW}, indicating a significant increase of the electronic anisotropy.

At this point, it should be noted that the effect of the electronic nematic phase on the in-plane ATS scattering intensity is unknown. In other words, the electronic nematicity may enhance the anisotropy that the structural transition imposes, or it may reduce it. Of course, the fact that the intensity of the in-plane spectra increases with lowering temperature suggests a reinforcing effect since the electronic nematic phase would likely grow

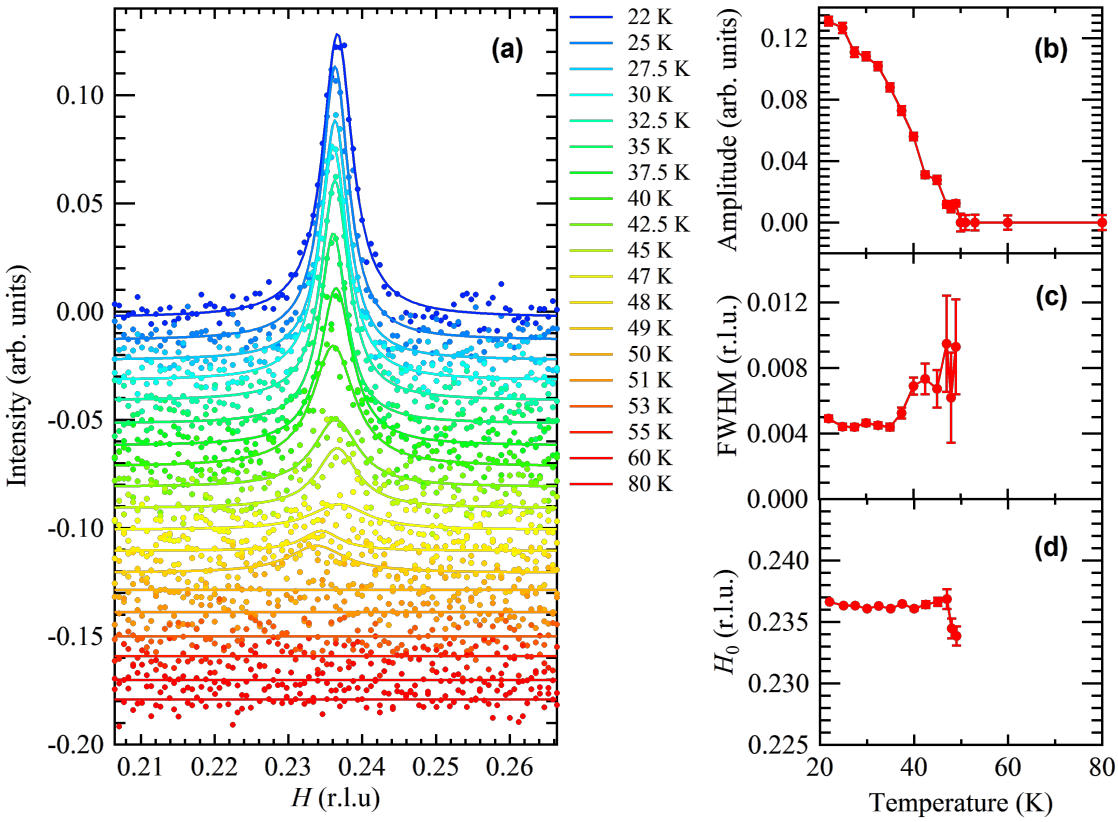

Figure 4.13: Temperature series of the CDW peak at the Cu L edge of LBCO(i). (a) After backgrounds were removed, data (dots) was fit with a Lorentzian (lines). Peak amplitude (b), full-width at half maximum (c), and peak centre (c) were recorded. H_0 was corrected for refraction. Data for nonsensical fits after the peak faded into noise are omitted.

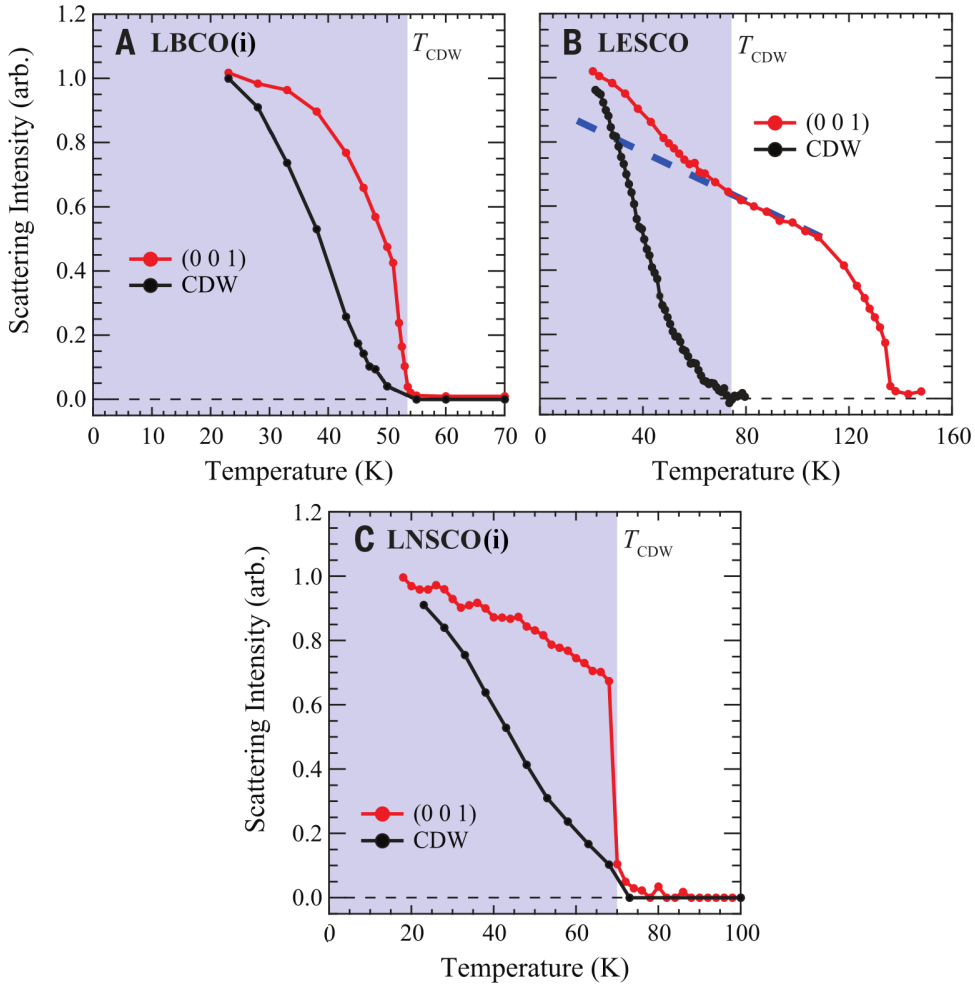

Figure 4.14: Comparison of CDW peak intensity with the ATS scattering strength, both at the Cu L edge, for (a) LBCO(i), (b) LESCO, and (c) LNSCO(i). For LESCO, notice the substantial change in the ATS curve's slope at the CDW onset temperture near 75 K that suggests CDW order may enhance electronic nematicity in this sample. (Data is normalized at high and low temperature to 0 and 1, respectively. Figure is adapted from Ref. 9.)

more stable as temperature decreases. In this case, the anomaly in the LESCO spectrum would then suggest that the CDW phase also cooperates with intra-unit cell symmetry breaking from electronic nematicity, and not just from the structural transition. Indeed, the way in which the onset temperature of the LTT phase correlates with the onset of the CDW phase shows a strong qualitative similarity with how we observed it to correlate with the electronic nematic phase; namely a coincident onset and a behaviour that suggests the electronic nematicity would exist at higher temperatures if not "cut-off" by the structural transition. It is not unreasonable to think, then, that the three symmetry-breaking phases may all strengthen one another. However, if the opposite case is true and electronic nematicity actually reduces the anisotropy from the structural transition (which is less likely, but cannot be ruled out), then the upturn in the LESCO spectrum would instead imply that CDW order competes with the electronic nematic phase, as it does with superconductivity, despite the fact that the two phases both correlate with the LTT structure.

Finally, when examining Figure 4.9, the reader may wonder if a different choice of normalization could have the spectra of the plane layer and the spacer layer all overlap in LESCO in the region with temperatures above T_{CDW}. The nematic divergence would then be present only in the anomalous region below the "upturn" that correlates with the CDW phase. If that were true, then the electronic nematic state would only be found alongside CDW order in all three samples, further strengthening the correlation of the two phases. Unfortunately, such an overlap is not found. By far, the most convincing overlap between any of the spectra is already showcased in Figure 4.9, and we take this as evidence to support our interpretation. Namely, as temperature is decreased, a first-order rise in anisotropy occurs at the LTT/LTO transition temperature. This is immediately followed by the development of electronic nematicity in the plane layer, which is enhanced at the onset temperature of CDW order in LESCO.

4.4.2 Group II Samples

Our second group of samples consisted of $La_{1.42}Nd_{0.4}Sr_{0.18}CuO_4$ (LNSCO(ii)) doped at $p = 0.18$ with atomic parameters provided by the crystal growers of $a = b = 3.75$ Å and $c = 13.2$ Å; and $La_{1.905}Ba_{0.095}CuO_4$ (LBCO(ii)) at $p = 0.095$ with $a = b = 3.778$ Å and $c = 13.157$ Å. Unique dopant concentrations, both in respect to each other and to all the samples in the first group, were intentionally selected to provide new onset temperatures for the LTT structural phase and CDW order in the hopes that new insight would be gained about their relationship with electronic nematicity.

Measurements of LNSCO(ii) were taken using the same procedure as for the earlier samples. After cleaving the sample and aligning it in the diffractometer, the (0 0 1) ATS peak was observed at the expected values of reciprocal space and energy. Our detailed alignment procedure (described above) was again implemented between temperatures, and count rates were recorded with the photodiode. This choice of detector was made for us due to unfortunate technical problems affecting the other detectors at the time. While the photodiode suffers from a lower quantum efficiency and sensitivity to ambient low-energy photons, the intensity of the ATS scattering proved sufficient to generate impeccable signal-to-noise ratios with proper modifications to the experimental setup (including blacking-out the chamber's windows). However, dealing with the technical issues did substantially reduce the amount of productive time on our experimental run, resulting in the acquisition of complete data sets for only Cu and apical O.

The data, along with the calculated FWHM and peak location L_0, is presented in Figure 4.15. The relative intensity of the second-order peak was far more intense at the O edge (4.15(b)) than at the Cu (4.15(a)), a feature that was consistently seen in every sample. As expected for the ATS peak, the FWHM remained relatively stable below $T_{\mathrm{LTT}} \approx 80$ K. Above the transition, the Cu peak is lost to noise and the O spectrum is dominated by the (0 0 2), whose FWHM is a little under half as large as the (0 0 1). In addition, the peak position in reciprocal space remained constant at both edges, with any deviation likely arising from errors in our procedure to correct for refraction and beamline drift.

The temperature dependence of the ATS intensity at each edge is plotted together in Figure 4.16, normalized as before. The behaviour of each curve is consistent with the results from the first group of samples. As the temperature decreases, there is a first-order gain in intensity indicating the LTT/LTO structural transition that greatly increases the in-plane orbitals' anisotropy throughout the sample. Subsequently, both curves continue to rise, but the apical O does so at a markedly slower pace. This once again reinforces the narrative of a distinction between orbitals associated with the CuO_2 plane and the spacer layer that cannot be explained by structural effects alone. Rather, the Cu orbitals exhibit behaviour of an electronic origin, suggesting the presence of an electronic nematic phase.

An attempt was made to characterize the temperature dependence of the CDW ordering peak for comparison with the (0 0 1), but the peak could not be found. As shown in Figure 4.17, our search at both the Cu and O edges showed little variation between scans taken at high temperature and at our apparatus' base temperature. This was true for both positive and negative regions of reciprocal space. Previous studies of other dopings, and indeed our own results on the other samples, have shown a distinctly recognizable peak (albeit a very broad one) at these coordinates, beam-energies, and levels of background

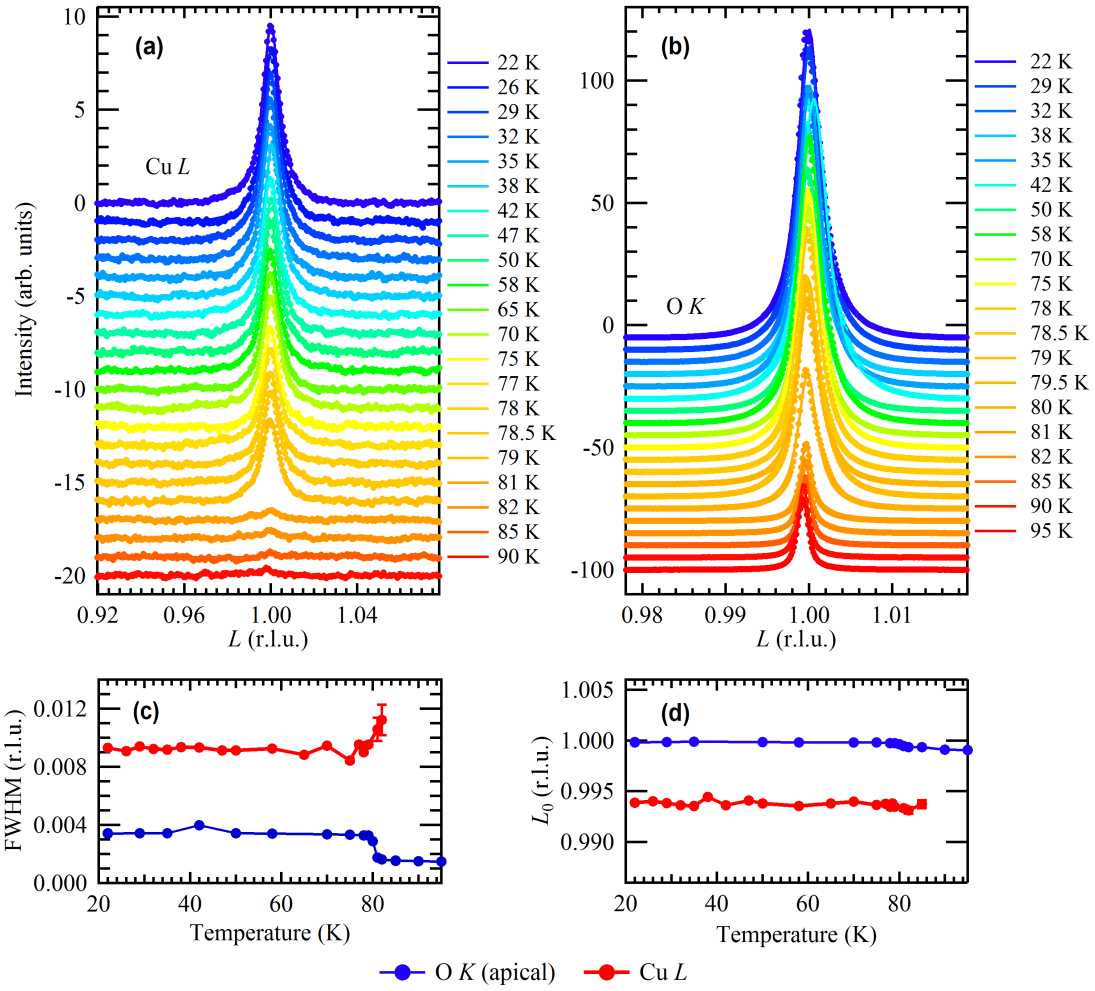

Figure 4.15: Temperature series of the (0 0 1) peak profile at the (a) Cu L and (b) O K edges in LNSCO(ii). Backgrounds have been removed through a subtraction of a polynomial fit, and each spectrum (dots) has been fit with a Lorentzian (lines). Clearly the (0 0 2) peak is much stronger at O. Note that the spacing in temperature between spectra is not linear. The full-width at half maximum (c) and peak centre (d) are plotted for each edge.

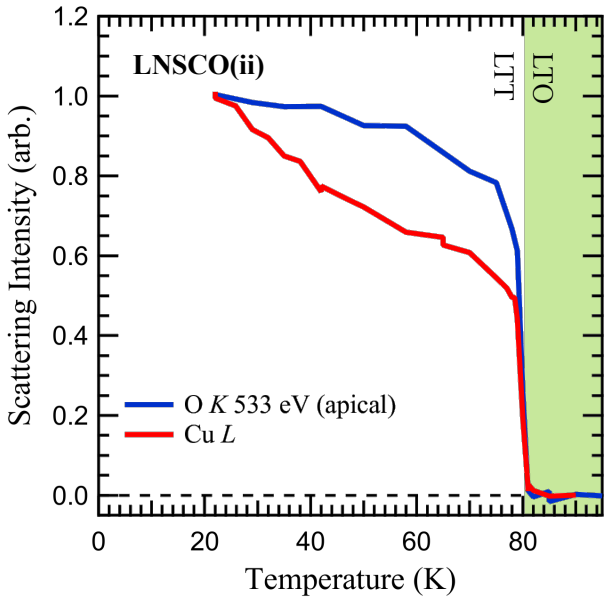

Figure 4.16: Temperature dependence of the ATS scattering intensity at the Cu L (red) and apical O K (blue) resonant edges in LNSCO(ii). As seen in the other samples, the Cu edge that reflects the CuO_2 plane layer shows distinct anisotropy from the apical O edge that reflects the spacer layer and follows the expected trend for the structural transition. This is more evidence for the presence of an electronic nematic phase. (Data is normalized at high and low temperature to 0 and 1, respectively.)

noise. We must therefore conclude that, above our base-temperature of 20 K, CDW order is either absent in LNSCO(ii) or extremely weak. This indicates that electronic nematicity does not require CDW order to form, and in fact its strength—characterized by the degree of separation between the curves—is still quite comparable to the other samples. This is consistent with what was observed for LESCO, where electronic nematicity was seen to persist at temperatures well-above the onset of the CDW.

The LBCO(ii) sample was also examined using the same procedure, except the Channeltron was again employed to record the temperature series spectra. After cleaving and alignment, the ATS peak was found at the expected energy and reciprocal space coordinates. Scans through the ATS peak at the Cu, Ba, and La edges are displayed in Figure 4.18. Again we see that the relative intensity of the second-order peak was far dimmer at Cu than the other two edges, an effect due to a combination of the Cu edge's high-sensitivity to ATS scattering and the energy-dependent flux of the beamline's second-order light. Regardless, the spectra all show high signal-to-noise with smooth evolutions with temperature. As shown in 4.18(d) and (e), the peak's position and FWHM, respectively, remained constant below T_{LTT}, as expected. At temperatures above the transition, the FWHM for Ba and La transition to that of their respective (0 0 2) peaks, and the FWHM of Cu vanishes as the peak is lost to background noise. Note again that the values of the FWHM differ between edges due to their difference in absorption coefficient, and the difference in L_0 values is due to error in our accounting for refraction and beamline drift.

The results of the ATS peak intensity as a function of temperature are plotted in Figure 4.19 with the spectra normalized as before. The result is as obvious as it is surprising: the Cu spectrum from the plane layer identically tracks the spectra from the spacer layer. The implication, of course, is that the in-plane anisotropy of all three orbitals are the same and do not show evidence of any electronic nematicity.

The absence, or at least far weaker presence, of electronic nematicity in this sample is consistent with other features of the spectra. First and foremost, the LTT/LTO transition occurs at a lower temperature than in any of the other samples; roughly 15 to 100 K lower. Since the LTT phase correlates with electronic nematicity, then it is expected that both phases would be suppressed at this doping. Furthermore, the transition itself appears to have less of a first-order character than in the other samples. The reasons for this are not clear, but it may be related to the fact that this Ba-doping exists in the structural phase diagram (Figure 4.5) near the border between the LTT and LTLO phases at low temperature.[1] Regardless, we note that the transition typically has a mix of first-

[1]The LTLO phase exhibits some of the same tilt as the LTT and could possibly still produce measureable

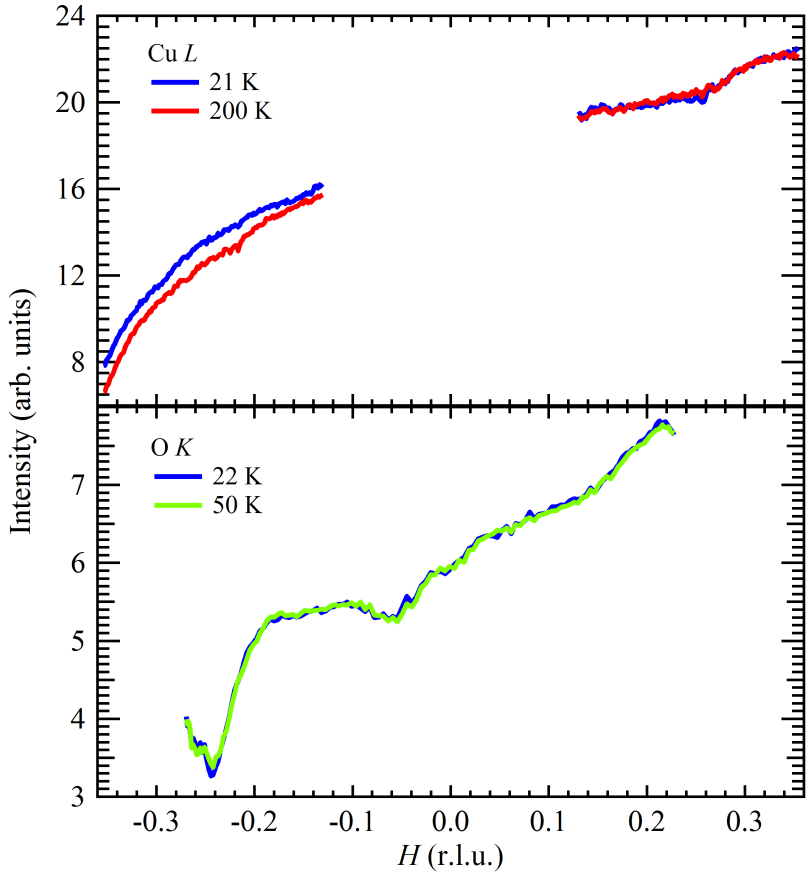

Figure 4.17: Search for the CDW peak in LNSCO(ii) at the Cu L (top) and O K (bottom) edges taken near $L = 1.5$. Scans measured at our base temperature (blue) are expected to show a peak near $H \approx \pm 0.25$ when compared to high-temperature scans (green and red). No evidence of a CDW peak's existence above our base temperature is found.

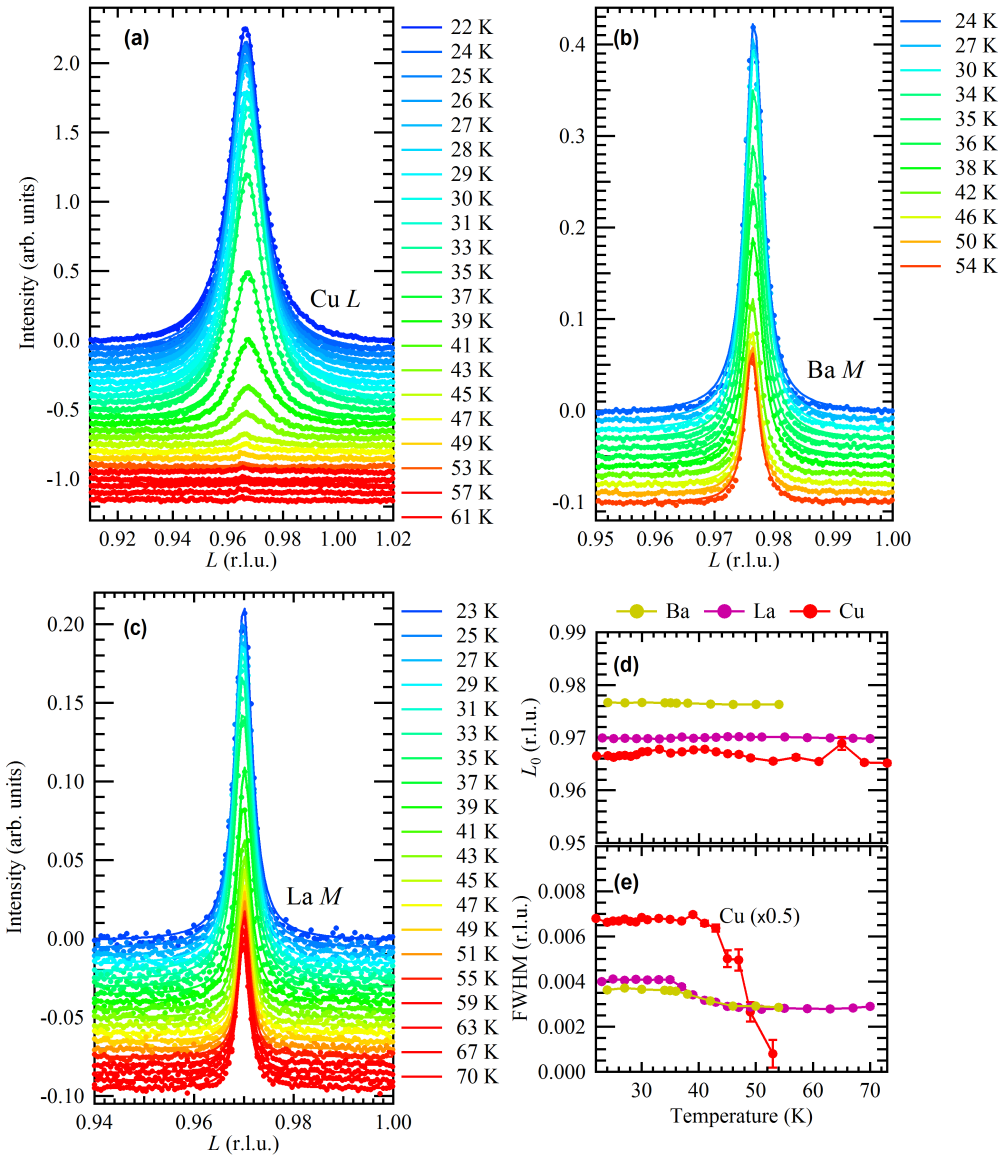

Figure 4.18: Temperature series profiling the ATS peak in LBCO(ii) at the (a) Cu L, (b) Ba M, and (c) La M edges. As before, backgrounds have been removed and data (dots) have been fit with Lorenztians (lines). Values of the peak centre (d) and full-width at half maximum (e) are plotted. Note the FWHM shows a decay near T_{LTT} as the fit transitions from the first-order to second-order peak.

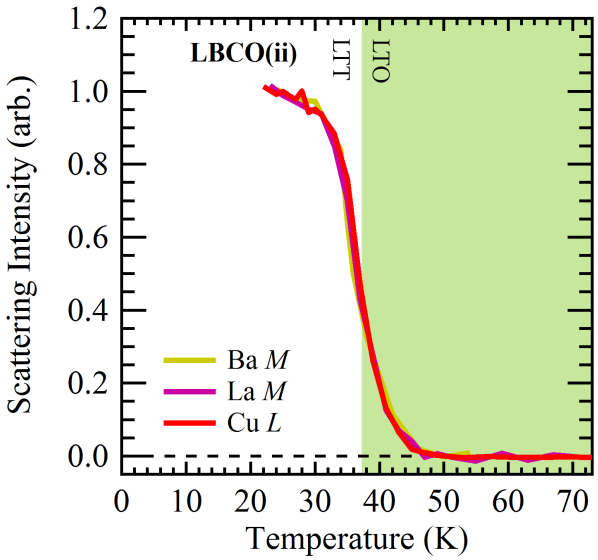

Figure 4.19: Temperature dependence of the ATS scattering intensity at the Cu (red), Ba (gold), and La (purple) edges of LBCO(ii). Unlike the other samples, all three ATS curves track one another and show no sign of an electronic nematic phase being present. (Data is normalized and high and low temperature to 0 and 1, respectively.)

and second-order character, as seen here and in other works,[118,128,190] and this indicates a weaker affinity for the system to transition out of the LTO phase as the temperature falls and into a state that permits electronic nematicity. Lastly, the absolute intensity of the ATS scattering peak was noticeably lower in this sample than in the ones measured previously, which also implies a weaker LTT distortion due to its linear relationship with that measurement. Otherwise, however, the spectra appear typical of ATS curves with an initial, strong increase in intensity followed by a slower rise with decreasing temperature. Along with the compelling overlap and low-noise of the spectra, we are provided with no other apparent explanation—such as an error in our experiment—for the anomalous absence of observed electronic nematicity.

ATS scattering was also recorded at the O edge at both apical and in-plane energies. It was hoped that the in-plane data in particular would shine some light on the unexpected behaviour of the Cu edge, perhaps by confirming the identical trend between the planar and spacer layers. The results of our measurements are plotted in Figure 4.20. Similar to the other edges, the spectra in each temperature series with backgrounds removed (4.20(a) and (b)) exhibit low noise levels, a smooth evolution with temperature, and a stable peak position and shape. The relative intensity of the second-order peak is significant for the in-plane data and non-negligible for the apical, but the (0 0 1) is sufficiently bright in both to provide an accurate measurement of the changing intensity. As well, the peak position and FWHM was recorded in 4.20(d) and (e), respectively, and both show the expected pattern of a constant value below T_{LTT}, followed by a transition to the value of the second-order peak above T_{LTT}. Curiously, however, a plot of intensity versus temperature (4.20(c)) reveals a different evolution for the two energies, and in fact the difference between the two is reversed from what is expected. The apical O, which is a member of the spacer layer, increases more rapidly with decreasing temperature than the in-plane series, and if the data were again normalized as before to converge at low temperature (see below), then the apical O would lie below the in-plane when $T < T_{\mathrm{LTT}}$. Instead, the data in 4.20(c) is normalized to once again showcase the unexpected similarity of the two spectra throughout the transition region.

Figure 4.21 plots the two intensity curves for O with that of Cu, which also accurately represents the Ba and La curves. Here, the curves are normalized as done for the previous samples, and clearly the O curves deviate from Cu with a slower rise as temperature decreases. While this qualitatively matches the deviations seen in other samples where we argued for the presence of electronic nematicity, the O spectra here stand out from the pattern with a more gradual rise that deviates from Cu immediately at the ATS onset temperature. It is unclear if this unique behaviour could be an experimental artefact. Only

ATS scattering.

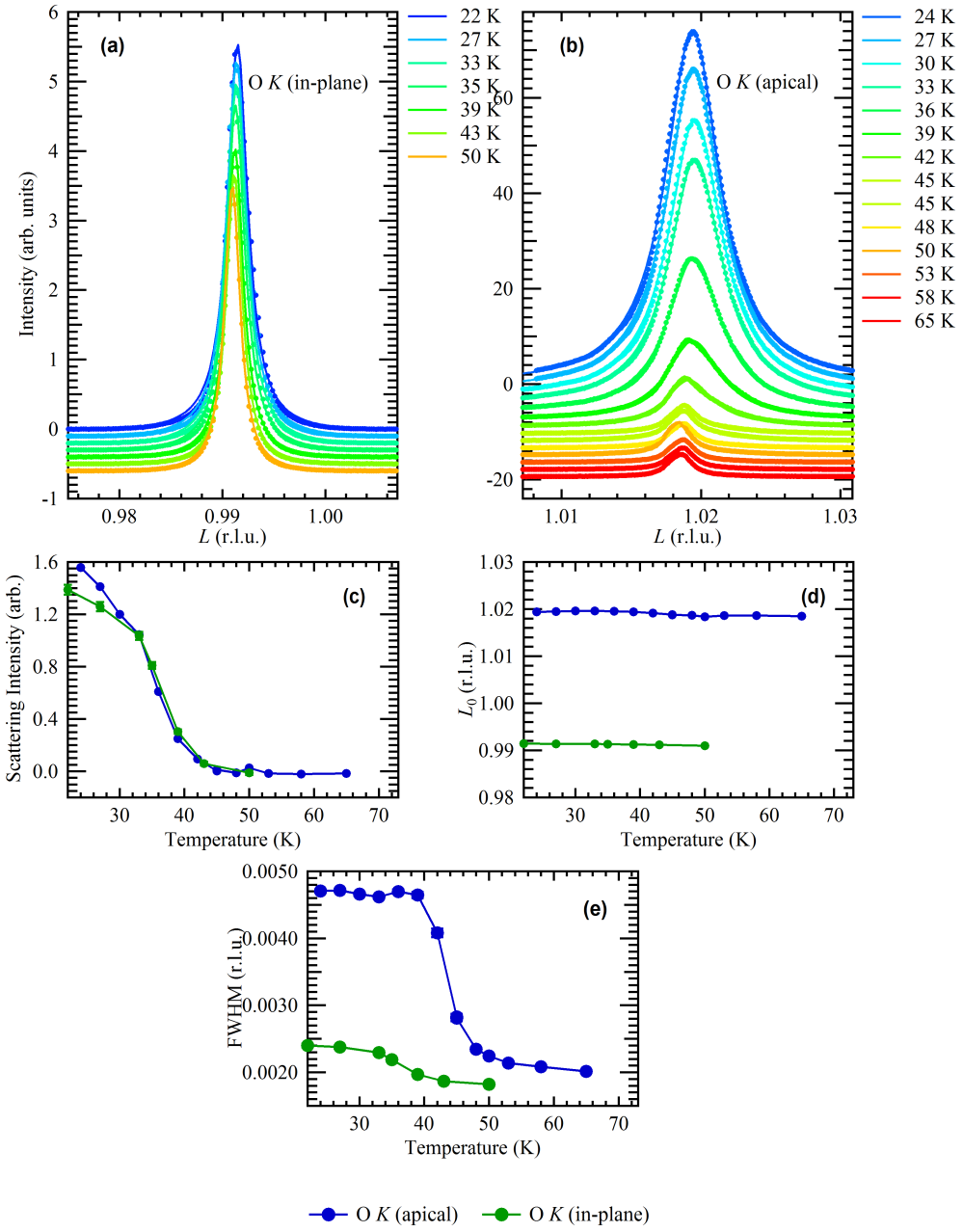

Figure 4.20: Temperature series profiling the ATS scattering peak in LBCO(ii) at the (a) in-plane and (b) apical O K edge energies. Backgrounds have again been removed and the data (dots) are fit by Lorenztians (lines). The fit intensity (c), peak centre (d), and full-width at half maximum (e) are plotted.

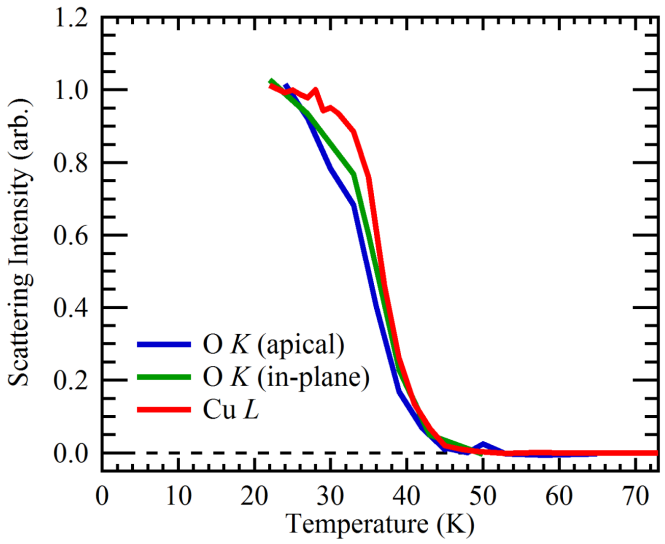

Figure 4.21: Temperature dependence of the ATS scattering intensity in LBCO(ii) comparing in-plane and apical O edges with the Cu edge, which also represents Ba and La. Spectra are normalized as in previous plots. The unusual behaviour of the O edges casts doubt on their demonstration of real electronic nematicity.

for this sample is the magnitude of the deviation comparable to the noise in the (0 0 1) spectra. Even more significantly, the structural transition temperature is the lowest in this sample, which means our normalization method is the least effective here at demonstrating a real deviation. We therefore must conclude that additional measurements, ideally using a cryostat with a lower base-temperature, are needed to confirm if the behaviour observed here is real.

We briefly note here that throughout this study, we have now encountered three anomalous spectra: the two O in LBCO(ii) and Eu in LESCO. As we have discussed, the causes underlying the magnitude and shape of their unusual features is not fully understood. Perhaps a detailed study that focussed on these edges specifically would reveal a common source, such as an experimental peculiarity or an overlooked correlation with another electronic feature. However, for now, we must take them only as curious outliers in our larger body of data.

The results of measuring the CDW ordering peak, recorded with the MCP at the Cu edge, are shown in Figure 4.22. As seen in previous samples, the background varied significantly relative to the peak's maximum intensity (4.22(a)), but the subtraction of a polynomial fit successfully isolated just the Bragg reflection (4.22(b)). While the CDW

peak is often weak in the La214 cuprates, it was especially so in this sample relative to those in Group I. This is similar to the weak intensity of the sample's ATS peak, which provides even further evidence to support the connection between CDW order and intra-unit cell rotational symmetry breaking. However, even the weakness of this peak did not impede the relative ease of its discovery and characterization, which we note in order to highlight a comparison with the case of LNSCO(ii) where we can be confident that the peak was absent. The peak occurred around $H_0 = 0.214$, and though the limited signal resulted in substantial error bars on our characterization, the peak's location and FWHM remained relatively constant before disappearing into the background at high temperature.

Finally, the temperature dependence of the CDW and ATS peaks are plotted together in Figure 4.23. Clearly, the CDW ordering phase and LTT structural phase onset at approximately the same temperature, as seen in LBCO(i) and LNSCO(i), and this further bolsters their correlation. Unique to this sample, however, is the similar trend shared by the two curves. Neglecting a small deviation and acknowledging the significant noise level of the CDW curve, the two appear to grow in-step as temperature decreases to imply a proportionality of the strength of the inter- and intra-unit cell symmetry breaking. Such a strong and direct connection between the two phenomena has not been observed before, and it is curious that it would be seen in LBCO(ii) where both are comparatively weak. Perhaps the overlap is just coincidence; a product of the likely event that the two onset at the same temperature and the predominantly second-order character of the LTT/LTO transition that is particular to this sample. However, we also note that this sample is unique in its lack of observed electronic nematicity, and thus the nature of its electronic correlations could also be unique in such a way that boosts the correlation between the LTT and CDW phases at the expense of the electronic nematic phase.

4.5 The Effect of Tilt Angle on Electronic Nematicity

All of the samples examined in this study exhibit a transition into the LTT phase[1] below some critical temperature, but the nature of that low-temperature structure is actually known to vary somewhat in its defining order parameter: the tilt angle of the O octahedra, Φ. Since the intensity of the ATS scattering is dominated by the resonant diffraction's dependence on energy and the experimental geometry, the absolute degree of anisotropy and the tilt angle from which it derives could not be directly investigated in our study. However, if broken electronic symmetry is indeed linked with the LTT distortion as we

[1] Or possibly the similar LTLO phase.

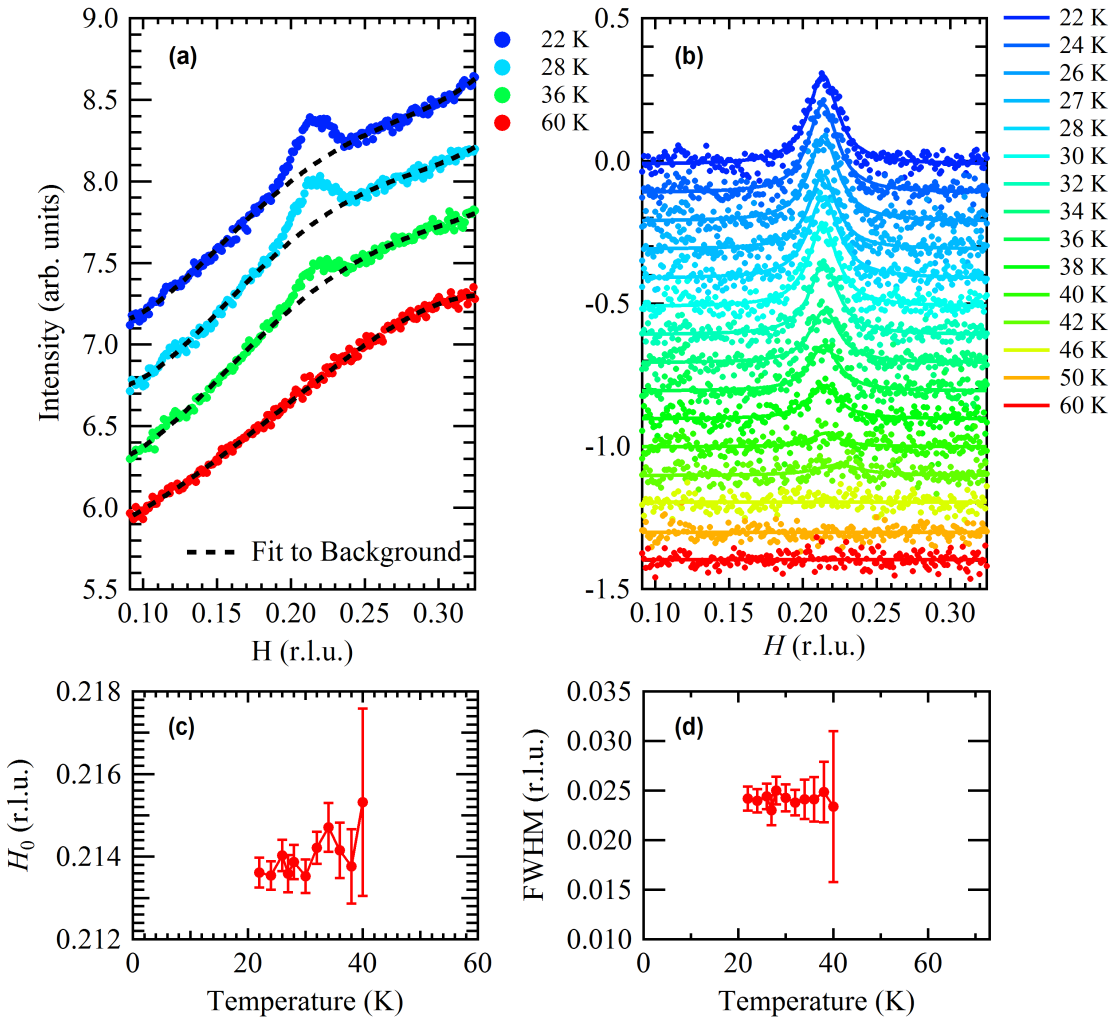

Figure 4.22: Temperature dependence of the CDW peak in LBCO(ii) measured at the Cu L edge near $(H, K, L) = (0.214, 0, 1.5)$. (a) The raw data (dots) with backgrounds fit to a polynomial (dashed lines). (b) Data with backgrounds removed (dots) fit to Lorenztians (lines). The fit centre (c) and full-width at half maximum (d).

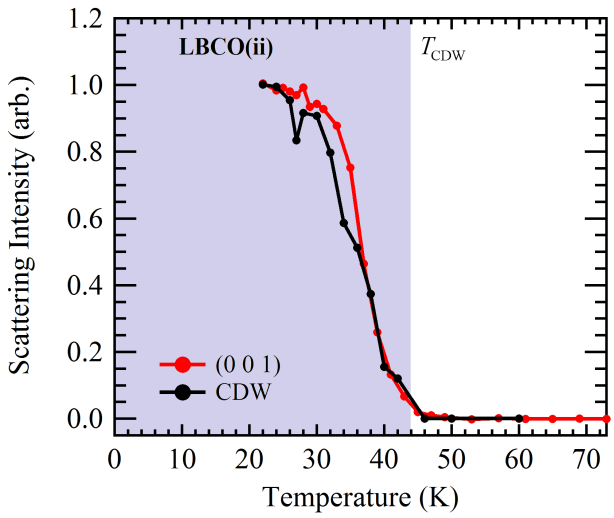

Figure 4.23: Temperature dependence of the ATS scattering intensity and CDW peak intensity, both measured at the Cu L edge, in LBCO(ii). (Data is normalized at high and low temperature to 0 and 1, respectively.)

have argued, then the value of Φ, and not just the binary condition of the presence or absence of a tilt, may be an important tuning parameter for the electronic physics.

The question of what role, if any, the magnitude of Φ plays in determining the features of the La214 electronic phase diagram has been asked many times before. Since the first discovery of the structural phase transitions in these materials, it has been observed that many electronic properties—such as resistivity, Hall coefficient, thermoelectric power, and magnetic susceptibility—undergo seemingly correlated changes.[195–200] Most interestingly to the condensed matter community, it was observed that the dip in the superconducting dome of LBCO's phase diagram coincides with the doping-dependence of its LTT phase, and a causal link between C_4 symmetry breaking and the suppression of superconductivity was immediately suspected.[180,201–203] Studies were constructed to investigate this possibility that exploited the material's diverse array of available dopants: by substituting isovalent rare earth ions and heterovalent alkali earth metals for La^{3+}, the degree of the LTT tilt and the carrier concentration could effectively be tuned independently.[130,181,187,195,204–206] It was found that while structural and electronic transitions often correlated, the connection was not robust. In particular, the suppression of T_c was centred at a carrier concentration of $x = 1/8$ regardless of the material's tilt angle. In light of this, Axe and Crawford[181]

predicted that the origin of the suppression was not a structural effect, but rather an electronic one that was strongly enhanced in the LTT phase, and a charge density wave was theorized as a possible explanation.[207,208] The existence of stripe ordering in this material was later discovered,[61] and recent evidence supports the idea that CDW order suppresses superconductivity generically across the cuprates.[8,66,71,106] As discussed above, our data and others' have demonstrated a strong connection between the LTT phase and CDW order that may explain the observed behaviour. However, more remains to be learned about the mechanism by which it does so and why, for example, it's transition temperature matches that of the LTT phase at some dopings but not others.

Büchner *et al.* performed doping studies on LNSCO with varying Sr and Nd concentrations and attempted to link the material's electronic properties to both the LTT transition temperature and the tilt angle.[187,206] In doing so, they observed a boundary separating regimes of electronic behaviour in their two-dimensional dopant-space that corresponded to a constant critical tilt, Φ_c. Specifically, they reported that the determining factor for whether bulk superconductivity was present in a sample at their base temperature below 10 K was if the tilt angle in that sample was less than $\Phi_c = 3.6°$. Their work therefore suggests that indeed some properties of electronically ordered phases in the La214 cuprates may not be directly related to the presence of the LTT phase, but rather to the degree at which the octahedra are tilted. We believe this to be consistent with our results presented in this chapter. First, our observation of structurally-induced rotational symmetry breaking generating further broken rotational symmetry in the form of an electronic nematic phase may require a critical value of $\Phi_c > 0$. A vanishing Φ_c would leave the system unstable to the formation of electronic nematicity due to local crystal defects, which is not observed. Furthermore, this could explain the lack of nematicity observed in our LBCO(ii) sample; the tilt angle may be below or very close to the critical value. Most importantly, though, an electronic nematic phase provides a concrete link between structural distortions and other correlated electronic states. Without it, the origin of a 3.6° critical angle dictating the presence of superconductivity seems somewhat arbitrary, and the variation in the onset temperature of the CDW phase is more challenging to justify. However, it seems more plausible that electronic nematicity is encouraged through structural nematicity such that it undergoes a steep transition at a small Φ_c, and it then competes with superconductivity either directly or indirectly through its strong cooperative relationship with CDW order.

The results of the work by Büchner *et al.* are reproduced in Figure 4.24 illustrating their proposed value of Φ_c. For future experiments, we propose additional studies like the ones discussed above to again be undertaken that investigate the relationship between the LTT tilt and the material's various electronic phases as a function of isovalent and heterovalent doping. As we have demonstrated, the characterization of the CDW and

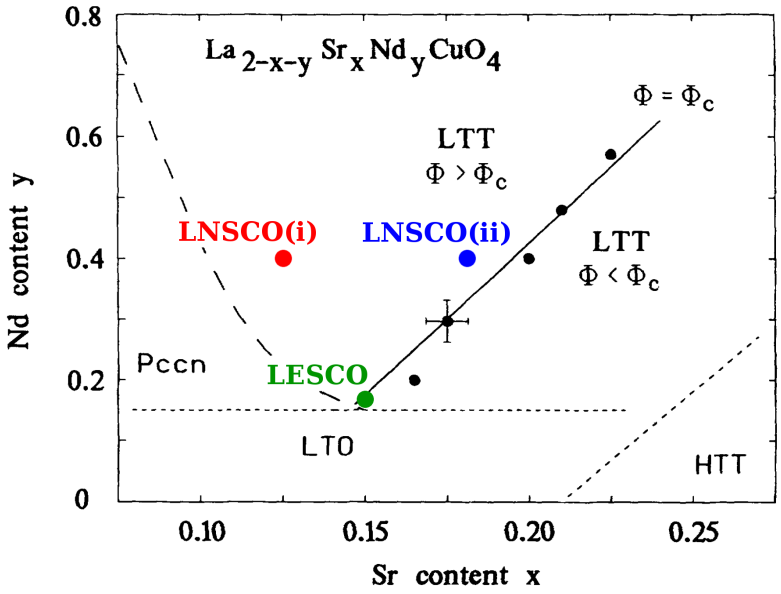

Figure 4.24: Structural phase diagram of LNSCO as a function of Nd and Sr doping showing a potential critical tilt angle Φ_c found by Buchner *et al.* to separate regions with and without superconductivity at temperatures below 10 K (black data points). Our own data for LNSCO and LESCO samples are overlayed in colour. (Figure is adapted from Refs. 187 and 206.)

electronic nematic phases are now easily achieved with modern resonant x-ray scattering facilities. Phase diagrams like the one shown could now be filled-in with substantially more detail; an endeavour that our findings suggest may be extremely valuable to improve our understanding of the strongly correlated electronic phenomena in the cuprates.

As a first step, we have added some of own data to Figure 4.24 for comparison with the authors'. Since Eu and Nd are isovalent with La, they are directly comparable as an agent for modifying the volume of the unit cell without affecting the carrier concentration. We have assumed here a ratio between the ionic diameters of Nd and Eu of 1.30:1.31 and calculated an effective Nd concentration that would produce the same result.[1] Admittedly, this is a rudimentary approach that may neglect some important differences between the crystals, but it should serve as a first-order approximation. Unfortunately, our LBCO data could not be approximated in this way as Ba ions have a larger diameter than La, so no amount of Nd or Sr ions that are smaller than La could approximate the crystal volume. Our results are consistent with the given value of Φ_c. All three of our data points lie

[1] See http://crystalmaker.com/support/tutorials/crystalmaker/atomic-radii/index.html

approximately on or above the critical angle and exhibit electronic nematicity, as expected. LNSCO(i) also experiences robust CDW order that onsets at the LTT transition, which may correspond to its position farther from Φ_c that implies a higher tilt angle. LESCO and LNSCO(ii) lie close to the critical angle, and they consequently experience delayed and potentially-absent CDW onset temperatures, respectively. Of course, we must be cautious about making excessively bold claims with only three data points, and indeed data spanning both sides of the critical condition would provide superior insight. More quantitative information about the relationship between the doping mixture and the tilt angle would also be useful. Perhaps an alternative scatter plot showing data points on the axes of tilt angle (or similar geometric property like unit cell volume) versus carrier concentration would more easily reveal insights about the phase boundaries, whereas using dopant concentration convolutes the two.

4.6 Summary

The La214 cuprates undergo a structural transition at low temperature that breaks the internal symmetry of the unit cell and permits ATS scattering off of the otherwise-forbidden (0 0 1) Bragg peak when measured on resonance. The strength of this ATS peak measures the in-plane anisotropy of a particular orbital and typically has an intensity that is proportional to the extent of the low-temperature distortion. Here, we have compared spectra between multiple orbitals in the unit cell to search for signs of additional anisotropy. We found a dichotomy in the data's temperature evolution: while measurements of orbitals in the rock salt spacer layer expectedly resembled the structural transition, measurements of orbitals in the CuO_2 plane layer showed a significant deviation. We argued that the origins of this deviation must be electronic interactions, and therefore our results constitute an observation of an electronic nematic state.

Five samples with varying carrier concentrations, unit cell volumes, and onset temperatures of the structural transition were studied: $La_{1.875}Ba_{0.125}CuO_4$, $La_{1.475}Nd_{0.4}Sr_{0.125}CuO_4$, $La_{1.65}Eu_{0.2}Sr_{0.15}CuO_4$, $La_{1.42}Nd_{0.4}Sr_{0.18}CuO_4$, and $La_{1.905}Ba_{0.095}CuO_4$. The electronic nematic state was observed in four of them, where it consistently onsets at the same temperature as the structural transition. This implies that its presence depends not only on the existence of the structural change, but also on the material's mix of heterovalent and isovalent dopants. In the material without electronic nematicity, $La_{1.905}Ba_{0.095}CuO_4$, the structural transition also occurs at the lowest temperature of the group, implying that intra-unit cell symmetry breaking is the least stable in this sample.

CDW order, well-studied in the La214 cuprates, was also measured for comparison. For

three of the samples, the CDW peak emerged alongside the structural transition, suggesting that all three symmetry-breaking phases tend to coexist. In $La_{1.65}Eu_{0.2}Sr_{0.15}CuO_4$, where CDW order onsets below the coincident appearance of the structural and electronic nematic phases, an enhancement in the ATS spectra of the CuO_2 orbitals was observed at T_{CDW}. This further supports the idea that these symmetry-breaking phases may cooperate with one another. However, CDW was not found at all in $La_{1.42}Nd_{0.4}Sr_{0.18}CuO_4$ despite it having an electronic nematic phase and the second-highest structural transition temperature.

Our data indicates that the stabilities and onset temperatures of the three phases are related in a nontrivial way. An underlying property that links them together may be the tilt of the O octahedra in the low-temperature structural phase. Building off the proposal by Buchner *et al.*, it may be that this tilt—which varies with doping—induces an electronic nematic state when it breaks the symmetry of the unit cell beyond some critical value. The electronic nematic state, in turn, may influence the formation of a CDW phase, and these two phases may affect the stability of superconductivity. We propose future studies using new dopant combinations that explore the parameter space of carrier concentration, unit cell volume, and low-temperature tilt to test this validity of this underlying connection and to further map out the electronic nematic phase diagram.

Chapter 5

Temperature Dependent XAS of Oxygen-Doped YBCO

5.1 Introduction

As discussed in the preceding chapters, it is now accepted that the pseudogap region of the cuprates' generic phase diagram encompasses multiple ordered electronic phases. The universal presence of a charge density wave has been established near 1/8 hole doping in all branches of the cuprate family tree, and spin density waves are known to exist both at low dopings near the antiferromagnetic phase boundary and alongside charge density wave order in the La-based cuprates (known as stripe order).[29,54] Evidence for additional phases has been accumulating as well, in both theoretical and experimental works (see for example, 35, 54, 159, 209–213), but their nature, number, and generality remain controversal. One such phase, that of electronic nematic order, has received particularly compelling support from theoretical proposals[176,177,214,215] and measurements of transport in $YBa_2Cu_3O_{6+\delta}$ (YBCO) and $La_{2-x}Sr_xCuO_4$ (LSCO),[154] neutron scattering in YBCO,[155–159] and STM in $Bi_2Sr_2CaCu_2O_{8+x}$ (Bi2212).[113] In Chapter 4, further evidence for its existence was presented from observations of anisotropy in the orbitals of the CuO_2 planes in multiple La-based cuprates measured with resonant x-ray scattering, as well as an apparent correlation between this phase and stripe order. However, whether this phase is unique to these materials or if it is indeed a universal feature of the cuprates is so far unclear. To make progress toward answering this question, more experimental data is required that can expound the details of the nematicity already discovered, as well as determine the presence or absence of this phase in other cuprates.

In choosing a direction for further investigations of electronic nematicity, YBCO offers a favourable choice. Its crystals are grown with high purity,[126,216] and the doping concentration is determined by the number of oxygen atoms in the Cu-O-Cu chain layers. As a result, the CuO_2 planes in YBCO have intrinsically less disorder than in the other cuprates. Furthermore, YBCO has a double layer of planes sandwiched between the spacer layers that contrasts with the single plane layer in the La-based compounds, and insight could thus be gained regarding the generality of any results the two structures may be found to have in common. Finally, the body of evidence already supporting the presence of electronic nematicity in this material, as mentioned above, suggests a more likely chance of a successful search. Similar arguments for focusing on YBCO were made during the search for density wave order outside of the La-based cuprates after the discovery of stripe order two decades ago,[65] and the same reasoning is sound when motivating the search for this new phase today.

As discussed in Section 4.1, collecting evidence of an electronic nematic phase is a nontrivial endeavour. Ideally, one would like to witness directly the onset of anisotropy in the orbitals of the CuO_2 planes that cannot be explained by other causes such as orthorhombicity of the lattice or the appearance of density wave order. In the La-based cuprates, the first-order phase transition from the LTO to LTT lattice structure provides a unique opportunity for doing precisely that via resonant x-ray scattering. This opportunity is not found in the other cuprates, but witnessing signatures of an electronic nematic phase using resonant x-ray spectroscopies should still be possible (though perhaps more challenging). Additionally, x-ray absorption and scattering measurements can be tuned to the specific energies and symmetries of the electronic states under study and can clearly distinguish between anisotropy found in the hybridized Cu $3d$ and O $2p$ superconducting orbitals and the rest of the crystal. Transport measurements, on the other hand, collect data from all atoms in the material simultaneously, adding ambiguity to the result, and STM measurements are only sensitive to surface states which may not accurately represent the properties of the bulk. We thus believe it worthwhile that exploratory resonant x-ray studies, informed by the evidence so far collected, now be undertaken on cuprates outside of the La-family.

As a specific example, electronic nematicity should be detectable in the temperature dependence of x-ray absorption spectroscopy (XAS). As described in Section 2.1, XAS spectra provide the unoccupied density of states projected onto an initial electronic wavefunction with symmetry that is determined by the incident photon's polarization vector.[1] Anisotropy in the superconducting states can therefore be uncovered through the compar-

[1]Since the electronic component of the initial wavefunction is a fully occupied, and thus spherically symmetric, set of orbitals.

ison of spectra with incident beams aligned to the a and b crystallographic axes. Some anisotropy is inherently expected in YBCO because of the Cu-O chains that run parallel to the b axis as well as the crystal's orthorhombic unit cell. While this is conceptually well-understood, the accuracy with which these features in the XAS can be quantitatively predicted may be insufficient for a reliable identification of an electronic nematic phase, whose effect on the spectra may be relatively subtle. Instead, electronic nematicity should be evident in the thermal evolution of the spectra where a change in the trend of the anisotropy—that is, a change in how the a-axis and b-axis spectra are evolving relative to each other—will appear below the phase's onset temperature. This change may be sudden or gradual depending on if the electronic nematicity onsets with a first- or second-order transition, respectively.

In this chapter, we investigate the thermal evolution of XAS spectra exploring the superconducting electronic states of YBCO in the hope of detecting signatures of an electronic nematic ordering phase. Three dopings are examined: very-underdoped ($\delta = 0.335$), underdoped ($\delta = 0.5$), and slightly overdoped ($\delta = 0.999$). The very-underdoped sample possesses a hole doping of $p \simeq 0.05$ per Cu atom,[133] which corresponds to the edge of the antiferromagnetic ordering phase and where electronic nematicity has previously been reported with the highest stable temperature (perhaps ≥ 200 K).[158,160] The underdoped sample has a hole doping of $p \simeq 0.10$ and is therefore at the onset of the 1/8 anomaly where superconductivity is suppressed. This is also where the high-temperature phase boundary of electronic nematicity may intersect with the CDW phase boundary near the latter's maximum stable temperature (≈ 150 K).[64,160] Lastly, the slightly overdoped sample has $p \simeq 0.19$, just past where superconductivity maximizes in YBCO and the competing CDW phase is severely weakened. These three dopings showcase important features in YBCO's known phase diagram that may impact the onset temperature of electronic nematicity, and this is likely to improve the chances of finding clear signs of its presence if it exists in this compound.

Ranging from 20 K to 300 K, a large effect is seen at the O K-edge, with changes of up to 25% of the intensity of the pre-edge features occurring in some dopings and orbital symmetries. This is comparable to the evolution of the spectral intensity with doping. The effects are also seen at the Cu L-edge, though with a relative intensity an order of magnitude less than O. Multiple electronic sources for the effects are considered, and it is concluded that the photonic excitations are likely coupling with collective modes in a Franck-Condon mechanism. Evidence for electronic nematicity is inconclusive, but the results provide an upper limit on the magnitude of its effect in XAS spectra.

5.2 Experimental Considerations

Our experiments were carried out at the REIXS beamline of the Canadian Light Source synchrotron.[65] The details of the apparatus are described in Section 3.1. The samples were grown as single-crystals in $BaZrO_3$ crucibles using the self-flux method,[126] and then detwinned and annealed under specific pressures of oxygen[216] to end up with the desired dopings. All measurements were taken at normal incidence ($\theta = 90°$) with the detector angled 35° from the beam ($\Omega = 145°$). The beam was polarized for either purely σ or π scattering and the samples were mounted such that the $\vec{\epsilon}$-vector was directed parallel to a single crystal axis during each measurement. Uncertainty in the mounting procedure was expected to be no more than ±1°. Furthermore, the crystals' faces were mechanically polished down to a grit of 0.05 μm prior to being transported to the synchrotron such that the plane of each surface being measured closely aligned with the planes of the crystals.

Due to the nature of the apparatus and its data collection software, the recorded energy values required an energy-dependent correction with a linear shift that was applied consistently to all spectra of a given edge. For Cu, a value was chosen such that the main peak in the $\vec{\epsilon} \parallel \vec{a}$ and $\vec{\epsilon} \parallel \vec{b}$ spectra was positioned at 931.3 eV, and for O such that the main peak in the $\vec{\epsilon} \parallel \vec{b}$ was at 529.5 eV, as seen in the literature.[65]

As is common in XAS, the fluorescent backgrounds differed slightly between samples and individual surfaces, and thus small corrections were applied in the form of uniform scaling and offsets in the vertical dimension to improve overlap. It is a validation of the high-quality of this dataset that only small scales/offsets were required; in the worst case $\leq 4\%$, and in many cases none at all. The appropriateness of the chosen scale/offset parameters is obvious for most spectra, but the data presented in Figure 5.1 provides deeper insight into how these corrections were chosen by aligning the spectra in the smooth regions far above and below the near-edge structure.

Not all crystal axes were experimentally available on all samples. Therefore, to expand the dataset, multiple samples of the same doping were sometimes measured. This was specifically the case for the doping of $\delta = 0.5$. One sample, referred to here as o2B, allowed measurements with $\vec{\epsilon}$ parallel to the a and b axes, and another sample, c2, the b and c axes. Though identical crystal-orientations, dopings, and preparation techniques should theoretically produce identical spectra in multiple samples, it is expected in practice that there would be some subtle differences (especially in the fluorescent background) due to factors like adsorbants, subtle surface irregularities, and local stoichiometric disorder. Therefore, data for the b axis was repeated to verify that the results were comparable across the two samples. Figure 5.2 shows an example comparison of the intensity of the Cu

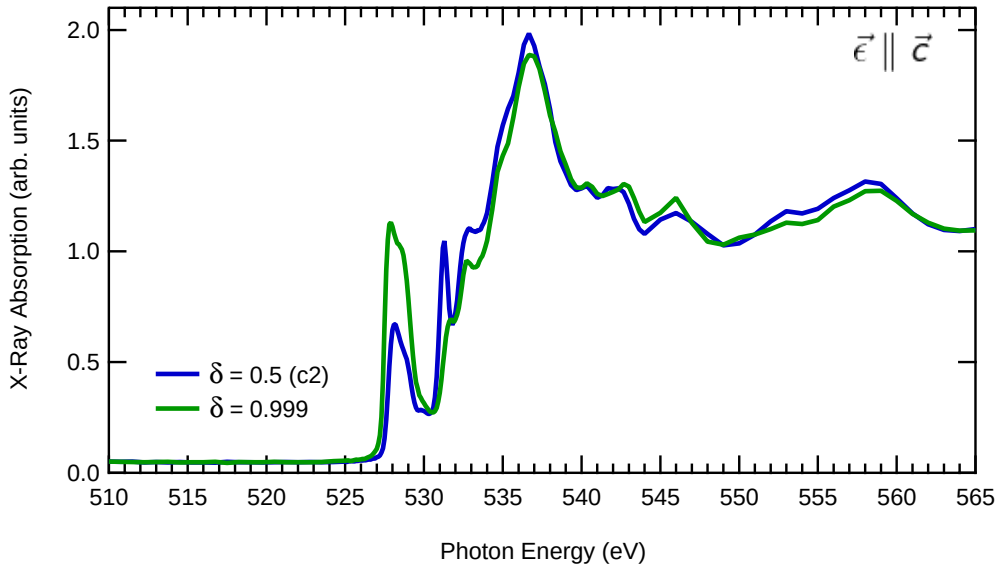

Figure 5.1: O K-edge spectra with $\vec{\epsilon} \parallel \vec{c}$ comparing $\delta = 0.5$ (blue) and $\delta = 0.999$ (green) dopings. Notice that the choice of vertical scaling and offset parameters result in good overlap of the spectra far from the edge. However, if one focuses only on the pre-edge region ($\sim 525 - 535$ eV), as is often reported in the literature, then the appropriateness of the parameters are less obvious.

L_3-edge at the extremities of our temperature range, 22 K and 300 K. Though the peak-to-background intensity is stronger in o2B by about 15%, implying a cleaner surface and deeper penetration depth at this resonance, the qualitative peak shape and its progression from low to high temperature is consistent for both samples.

5.3 Results and Discussion

5.3.1 Doping Dependence

Before analyzing how the spectra change with temperature, it is useful to review the key features of YBCO XAS and their dependence on oxygen doping. Figure 5.3 shows the Cu L_3 absorption edge, for all dopings and crystal axes, at the spectrometer's base temperature of about 22 K. The results are similar to other data in the literature.[32,65,217–222]

The Cu atoms in the CuO_2 planes have a single hole in their valence shell with $3d_{x^2-y^2}$

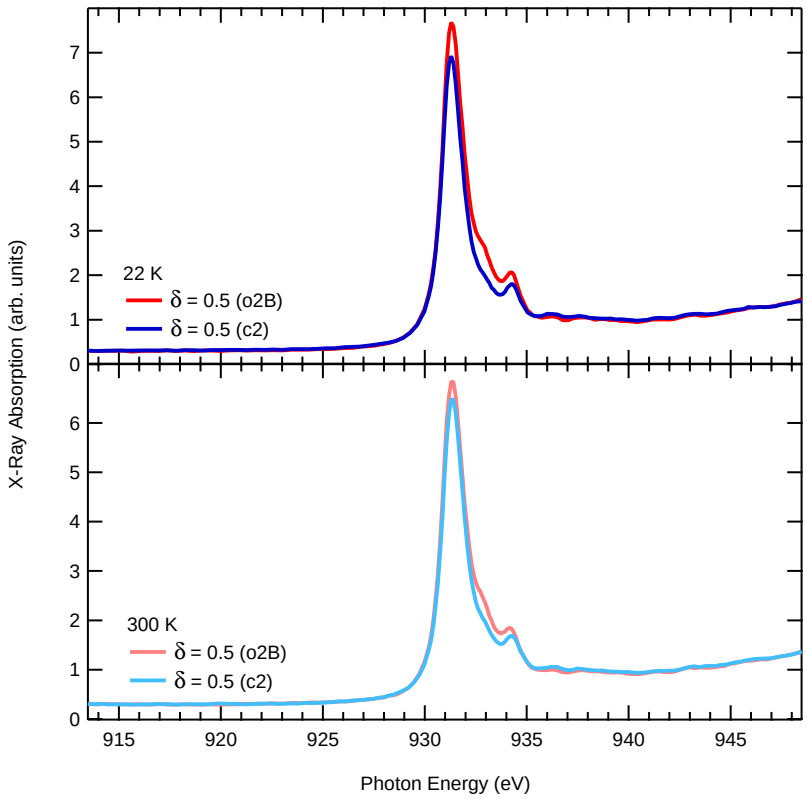

Figure 5.2: Comparison of spectra from the two $\delta = 0.5$ samples, o2B (red) and c2 (blue), with $\vec{\epsilon} \parallel \vec{b}$ at the Cu edge for low (upper panel) and high (lower panel) temperature. The o2B sample has a higher resonant intensity, implying a deeper penetration of the incident beam, but otherwise shows the same features and temperature dependence.

symmetry. This is the cause of the intense peak at 931.3 eV in the $\vec{\epsilon} \parallel \vec{a}$ and $\vec{\epsilon} \parallel \vec{b}$ spectra. There is also weight present at this energy in the $\vec{\epsilon} \parallel \vec{c}$ spectra due to some hybridization of $3d_{x^2-y^2}$ and $3d_{3z^2-r^2}$ states,[65] but its weak intensity relative to the peaks from the chains makes it difficult to discern in the two dopings shown. In addition, holes appear in the hybridized Cu $3d_{x^2-y^2}$ + O $2p_{x(y)}$ orbitals of the planes as O is added to the undoped parent compound. This produces a $3d^9\underline{L}$ ligand state on the high-energy shoulder of the main peak that increases with doping, seen here around 932.8 eV in the $\vec{\epsilon} \parallel \vec{b}$ and (to a lesser extent) in $\vec{\epsilon} \parallel \vec{a}$ spectra.

In the chains, the Cu atoms have a full $3d^{10}$ shell in the undoped parent compound. However a peak in the L-edge that decreases with doping is still observed corresponding

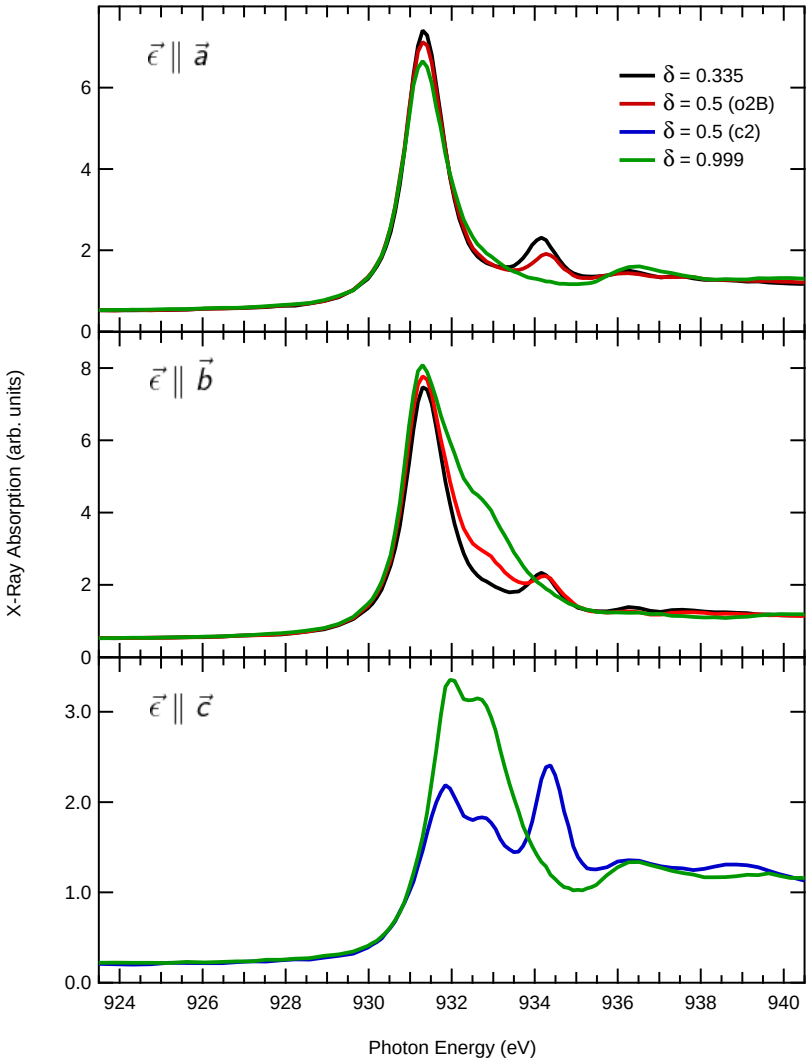

Figure 5.3: XAS of the Cu edge at 22 K showing changes to the spectra with O doping.

to monovalent Cu at about 934.3 eV along all three axes, similar to the phenomenon seen in Cu_2O.[222] Doping introduces holes with $3d_{y^2-z^2}$ symmetry around Cu, as well as $3d^9\underline{L}$ ligand states with neighbouring O. This causes the two, intense peaks at 931.9 and 932.7 eV, respectively, in the $\vec{\epsilon} \parallel \vec{c}$ spectra that increase with doping, as well as contributing additional weight to the shoulder for $\vec{\epsilon} \parallel \vec{b}$. A small peak arising from chain states is also visible around 936.5 eV.

A similar plot for the O K-edge is shown in Figure 5.4. Again, the doping-dependence is similar to data in the literature.[65,217,218] With increasing doping, holes appear in the $2p_x$ and $2p_y$ states of the planes that are hybridized with neighbouring $3d_{x^2-y^2}$ Cu states, producing bright peaks around 529.5 eV for $\vec{\epsilon} \parallel \vec{a}$ and $\vec{\epsilon} \parallel \vec{b}$. The shift in spectral weight indicates the transfer of holes from the upper Hubbard band around 531 eV into Zhang-Rice states in the valence band. In the chains, O produces holes in states hybridized with Cu $3d_{y^2-z^2}$ orbitals that appear at 529 eV and 529.5 eV for $\vec{\epsilon} \parallel \vec{b}$ and $\vec{\epsilon} \parallel \vec{c}$, respectively, and increase with doping. At the same time, other states disappear in the chain layer, as evidence by the decreasing peak near 533 eV.

5.3.2 Temperature Dependence

The results of the XAS measurements of the Cu L and O K edges are illustrated in Figures 5.5 to 5.11. For $\delta = 0.335$, spectra for the a- and b-axes were recorded; for $\delta = 0.5$, all three axes were recorded, but spread across two physical samples; and for $\delta = 0.999$, all three axes were recorded. Discrete temperatures were selected ranging from 22 to 300 K. Going to higher temperatures would have made any temperature-dependent changes in the XAS spectra more dramatic but would also have risked degradation of the oxygen-ordering.[10,141] Difference spectra that highlight the changes from the lowest-temperature curve were also calculated and plotted at the bottom of each figure.

The majority of the Cu spectra show a comparable evolution with temperature. Along the a- and b-axes, both the main peak and the higher-temperature chain peak show a moderate reduction in intensity with increasing temperature. The peaks may also experience slight broadening, but the effect is subtle. Additionally, the peaks appear to migrate to lower energies, with a shift on the order of 0.1 eV. However, this is comparable to the resolution of the spectrometer at this energy, and while this could therefore be an artefact of beamline drift or other errors, the consistency of the pattern in all four samples suggests that it is real. Curiously, the highest temperature spectra deviate from the rest with a shift to higher energy than the base-temperature spectrum, and this we do interpret as an experimental error. Even with meticulous care, the highest temperature scans are the most likely to suffer various discrepancies from sources such as flexing of the cryostat and the longer time period between its measurement and that of the base temperature. Along the c-axis, the same effects are apparent at all peaks but with a somewhat greater magnitude, especially in the $\delta = 0.5$ sample.

The O spectra show more dramatic changes. Unfortunately, they also suffer from more noise due to a variety of common difficulties seen at this energy. As discussed in previous

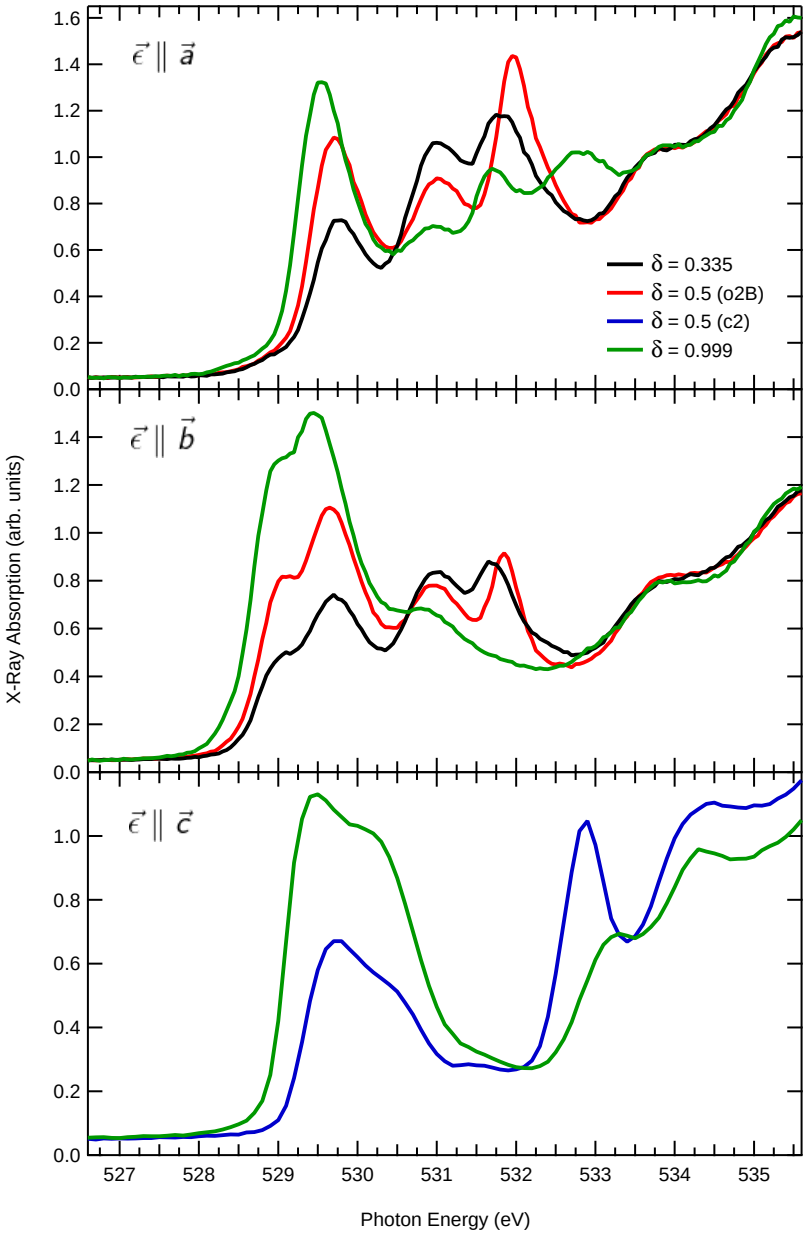

Figure 5.4: XAS of the O edge at 22 K showing chages to the spectra with O doping.

chapters, these can arise, for example, from weaker fluorescence and the adsorption of O-containing compounds on the sample or optical components of the spectrometer, which

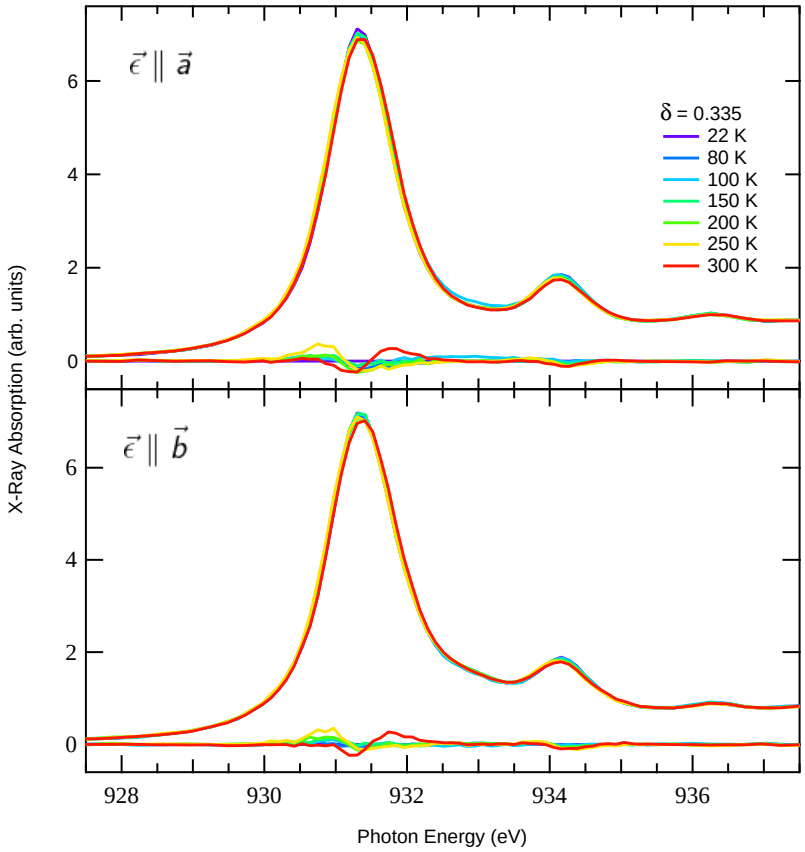

Figure 5.5: Temperature dependence of the $\delta = 0.335$ sample at the Cu edge.

can be difficult to avoid. However, the signal-to-noise ratio varies between samples and polarizations, and clear patterns in the data are apparent. Many peaks again are reduced in intensity and broaden with an increase in temperature. This is particularly dramatic for the peaks at 529.5 and 532 eV in the a- and b-axis spectra, where the $\delta = 0.5$ sample exhibits the greatest change. The peaks corresponding to the chain layer at 533 eV in the c-axis spectra and at 529 eV in the b-axis also diminish and broaden; so much so that the 529 eV peak in $\delta = 0.335$ smears out into a muted shoulder feature. Other peaks, however, increase in intensity. The peak associated with the upper Hubbard band at 531 eV definitively grows with temperature in both the a- and b-axis spectra, and small but consistent increases in spectral weight are even visible in the c-axis spectra (that could be due to a small misalignment of the sample). The enhancement is most obvious in the $\delta = 0.335$ sample and becomes minimal after the majority of spectral weight has been transferred to the

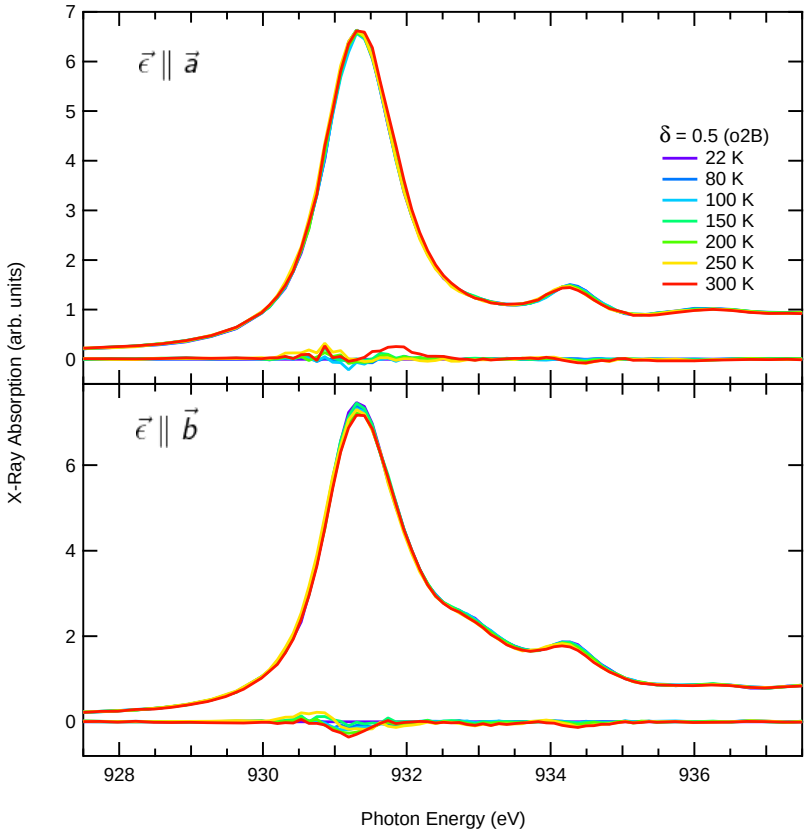

Figure 5.6: Temperature dependence of the $\delta = 0.5$ (o2B) sample at the Cu edge.

Zhang-Rice states in $\delta = 0.999$, as expected. The twin peaks associated with chain states in the c-axis spectra of the $\delta = 0.999$ sample also shows a substantial addition of spectral weight, as well as a noticeable broadening along the low-energy shoulder. This contrasts the minimal change in the same peak in the $\delta = 0.5$. Similar to the case of Cu, small shifts in the positions of the peaks could be present, but they would again be comparable to the energy resolution of the spectrometer and significantly obscured by the higher noise levels.

The most curious change with temperature is the "filling-in" of the valleys between peaks; specifically, between the 529.5 and 531 eV peaks in the a- and b-axis spectra. Peak broadening can and does account for much of the increases seen between peaks throughout the data, but it cannot account for it all. The most dramatic example occurs in the $\delta = 0.335$ sample where a significant peak in the difference spectra appears near 530.5 eV. Clearly, new spectral weight is being added to the XAS, and not just transferred from

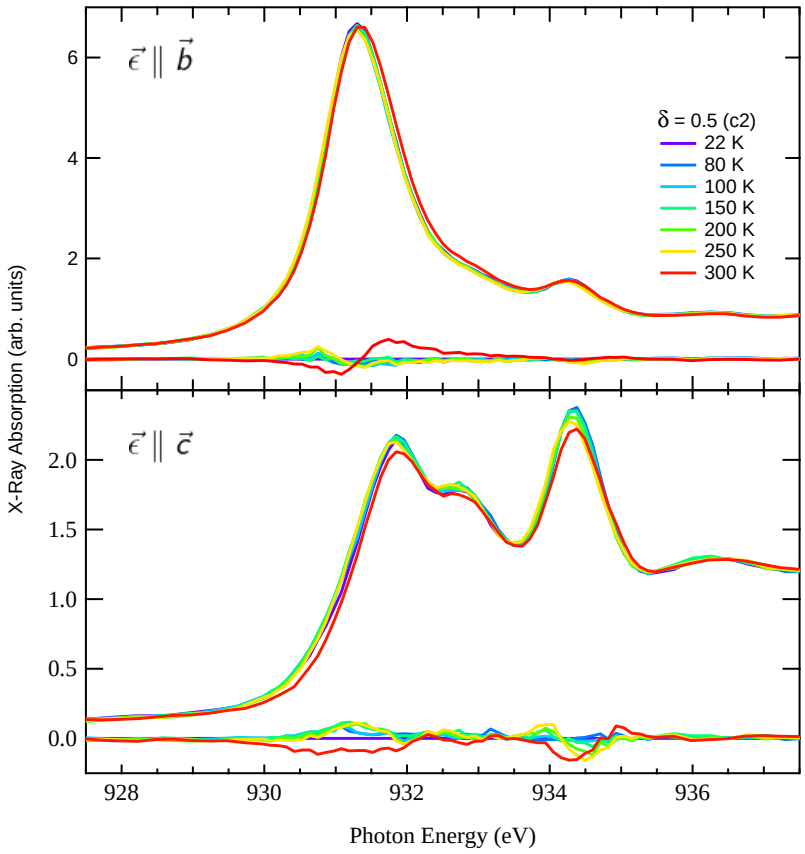

Figure 5.7: Temperature dependence of the $\delta = 0.5$ (c2) sample at the Cu edge.

nearby regions. Small reductions and broadenings of peaks that shift spectral weight have been witnessed before in temperature-dependent studies,[223–228] including in YBCO.[229,230] However, this behaviour is far more dramatic. While we cannot definitively identify its origins, we suspect coupling of the XAS to phonons in an inelastic Franck-Condon-type mechanism. For more on this topic, we direct the reader to consult references such as Refs. 231–233.

From this data, we cannot report any obvious signature of an electronic nematic phase. The changes with temperature occur with the same general pattern and comparable magnitude across polarizations, especially between the a- and b-axis spectra where a nematic phase is expected to manifest. In fact, the general trend of most of the peaks exhibiting a significant reduction in intensity and a modest broadening persists across dopings, occurs

at both absorption edges (albeit with a higher relative magnitude at O), and effects peaks associated with both the plane and chain layers. Even the increase of the upper Hubbard band's peak and the spectral weight in the neighbouring valley occur similarly in both the a- and b-axis spectra for each doping.

To further quantify these observations, the linear dichroism was calculated as a function of temperature between the a- and b-axis for each doping and both absorption edges, and the results are plotted in Figure 5.12. Clearly, very little temperature dependence is evident. Some evolution may be present in the pre-edge of the main Cu peak, but it is comparable to the intensity of the noise. At O, a more convincing decrease in dichroism on the order of 10% of the peak intensity is apparent at the 529 eV pre-edge peak, which is associated with states in the chain layer. Similarly, a small decrease may occur at the peak near 532 eV. However, no obvious change occurs in the states associated with the CuO_2 planes, and we cannot report any apparent onset of an electronic nematic phase.

5.4 Conclusions

With a mounting body of theoretical proposals and experimental evidence for the presence of electronic nematic ordering in underdoped cuprates, it is important to search for this phase in more materials using a variety of experimental techniques and determine how widespread it may be. However, collecting unambiguous evidence for this elusive state can be challenging and requires creative approaches. Resonant x-ray spectroscopies are a powerful probe of the symmetry of electronic orbitals, and it falls to reason that they could be useful tools in this endeavour. Indeed, resonant soft x-ray scattering has been used to discover electronic nematicity in the La-based cuprates, as described in Chapter 4, using a method that is limited in applicability to that material family. We proposed that near-edge XAS, which shares the same physical process at its heart as resonant scattering, could also reveal this phase through an examination of the temperature evolution of absorption spectra. If so, this technique would have the benefit of a wide applicability across the cuprates. We tested this hypothesis on three dopings of YBCO by measuring at the Cu L and O K edges with polarizations aligned to the three crystallographic axes. Many effects of temperature on the XAS were observed, including the reduction and broadening of many peaks. Conversely, the peak corresponding to the upper Hubbard band gained intensity, as did the adjacent region at lower energy. We suggested that this was an indication of effects from phonon coupling. Ultimately, though, few signs of a temperature-dependent anisotropy were observed, and we must report a null result in the search for electronic nematicity. Instead, our results provide an upper bound on the visibility of any effects

from an electronic nematic phase on XAS at the Cu and O edges if it does indeed exist in YBCO at these dopings, as other studies support.[154–159]

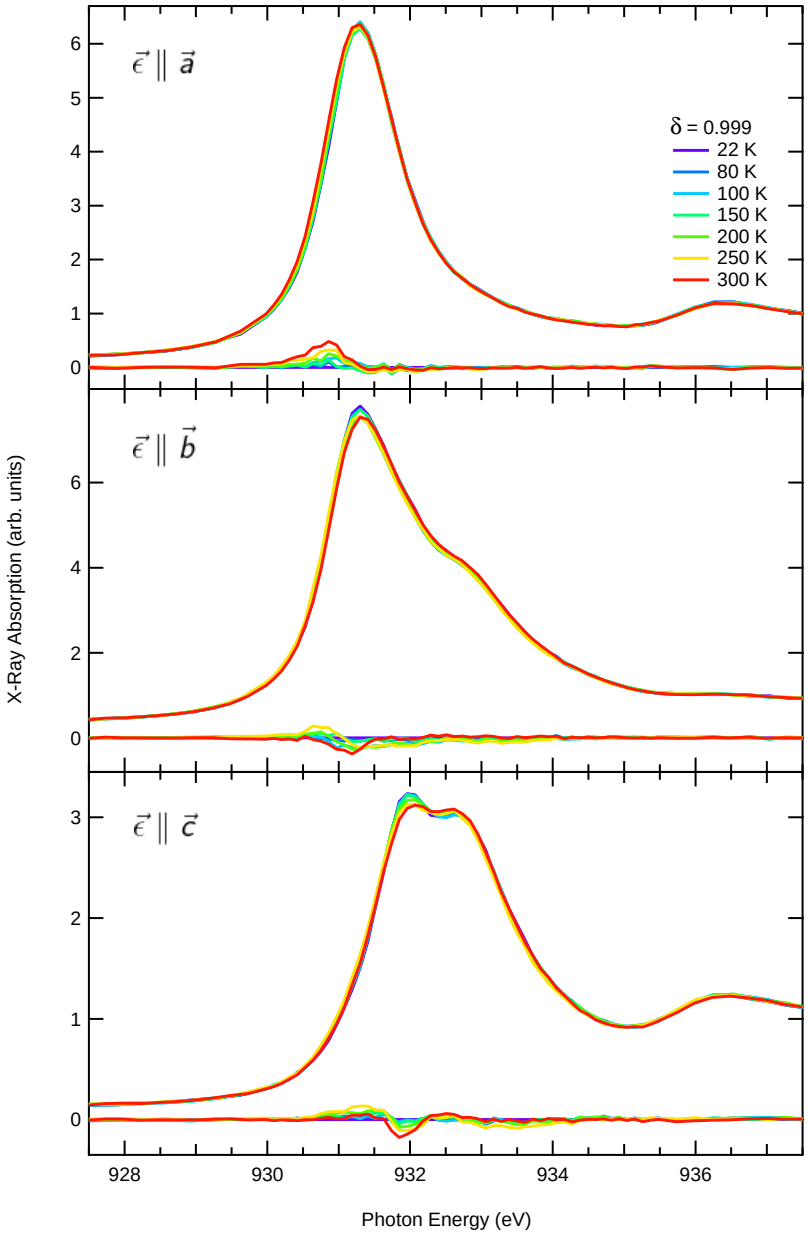

Figure 5.8: Temperature dependence of the $\delta = 0.999$ sample at the Cu edge.

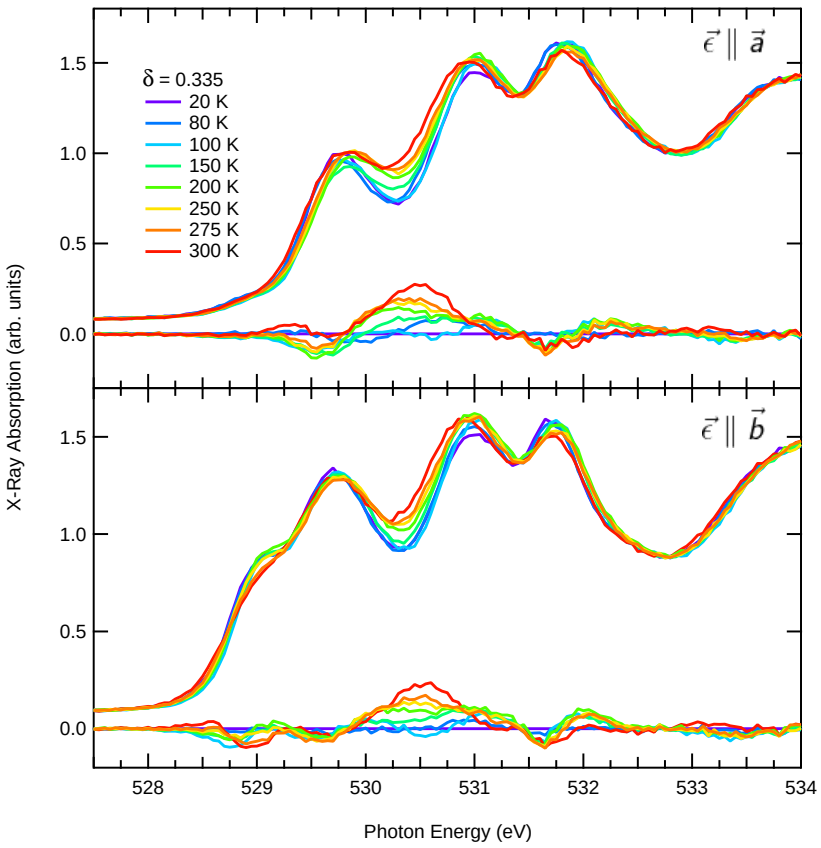

Figure 5.9: Temperature dependence of the $\delta = 0.335$ sample at the O edge.

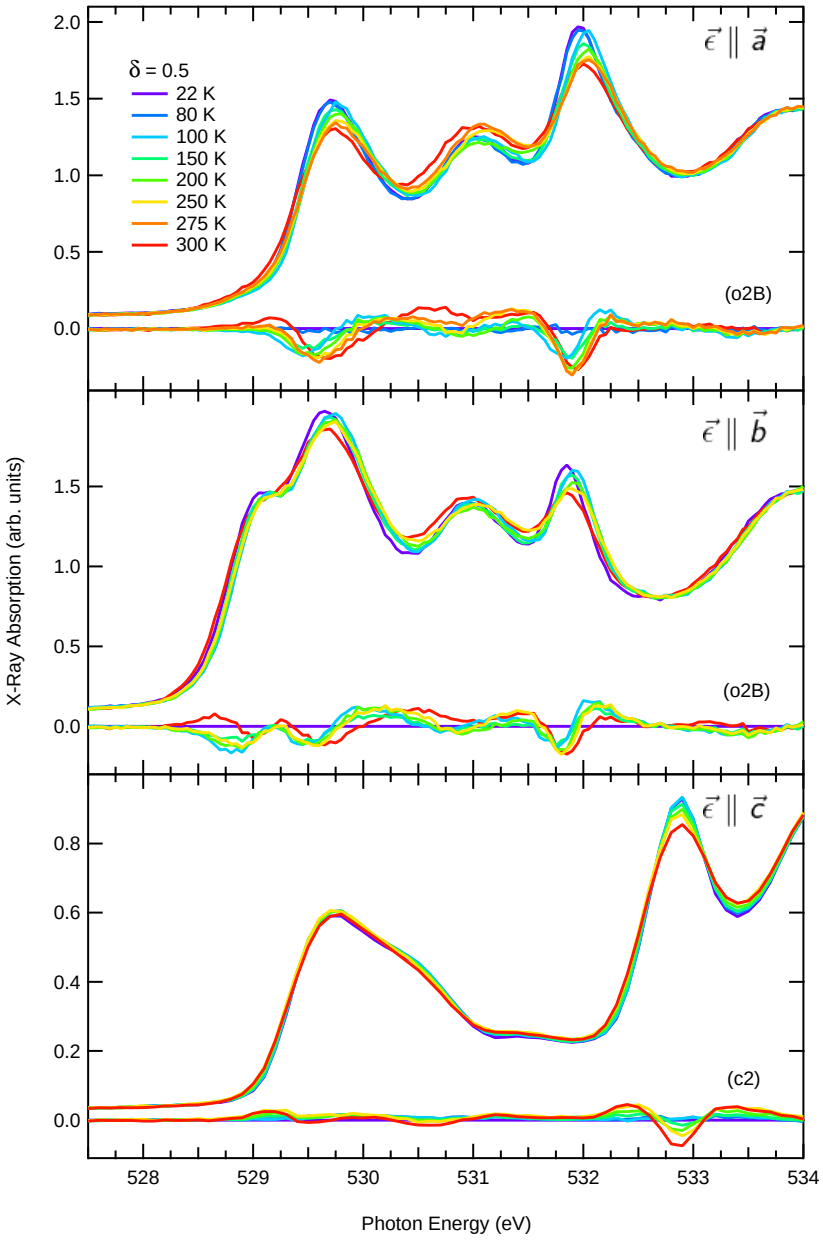

Figure 5.10: Temperature dependence of the $\delta = 0.5$ sample at the O edge.

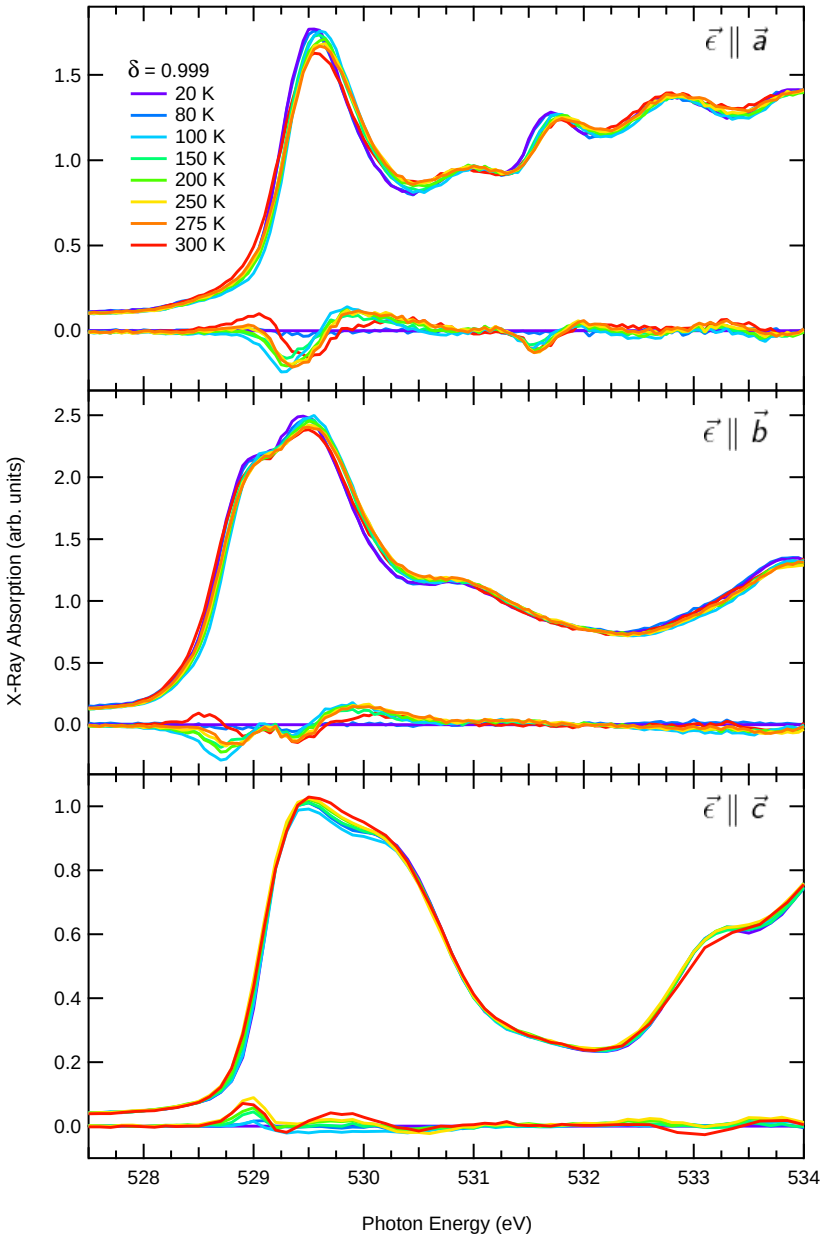

Figure 5.11: Temperature dependence of the $\delta = 0.999$ sample at the O edge.

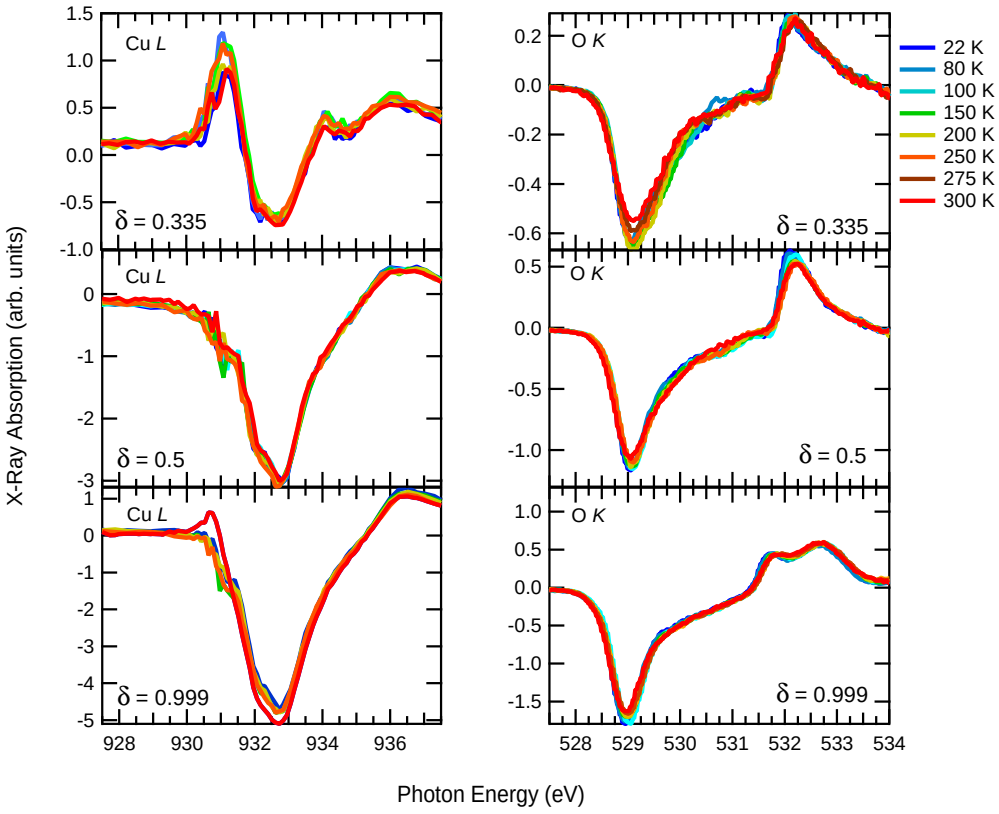

Figure 5.12: The x-ray linear dichroism at the Cu L (left) and O K (right) absorption edges for the $\delta = 0.335$ (top), $\delta = 0.5$ (middle), and $\delta = 0.999$ (bottom) samples, calculated as a-axis spectra minus b-axis. Due to the difference in fluorescence, only relative magnitudes can be compared between datasets. Only small changes with temperature are evident.

Chapter 6

Conclusion

After three decades of intense study, many mysteries still remain in the electronic structure of the cuprates. The rich interactions between electrons that lead to complicated ordering patterns have provided a deep well from which researchers continue to draw new understanding with both theoretical and experimental studies. How the symmetry of the electronic structure breaks at different temperatures and dopings, and the details of how the electrons subsequently order and behave, has been a particularly important source of insight. With the work in this dissertation, we hope to contribute further understanding on this topic, particularly regarding the local structure of charges in the CDW phase and the characterization of new broken symmetry phases such as electronic nematicity. Resonant x-ray spectroscopies have proven themselves very powerful for studying the electronic structure of the cuprates and were obvious tools of choice for this endeavour. While our study of the temperature dependence of XAS spectra found a null result, our novel experiments using RSXS will hopefully provide new effective methodologies for studies of electronic symmetry. We also hope that our work has added to the (already massive) pool of experimental data on the cuprates in a meaningful way by addressing the critical question surrounding the detailed nature of charge ordering patterns.

In Chapter 3, we used RSXS to probe the symmetry of the CDW order in 1/8-doped LBCO and two dopings of YBCO. Model calculations revealed a monopolar character in LBCO and along the b-axis of YBCO. This deviates from some theoretical proposals that have suggested a quadrupolar CDW as a generic feature of the cuprates. It also contrasts a similar report made earlier on YBCO that implemented a less ideal experimental geometry, highlighting the importance of geometry on this type of experiment. Along the a-axis, the CDW exhibited a surprisingly different symmetry. We were unable to uniquely determine the scattering tensor, for which more data, and perhaps a refinement of the scattering

model, would be needed. However, our results indicated the presence of orbital order along this direction, and we determined that a CDW with either strong asymmetry or modulations of the orientations of its orbitals could produce our dataset.

In Chapter 4, we exploited a low-temperature structural distortion that breaks the local rotational symmetry in the unit cell of the La-based cuprates to perform resonant ATS scattering. By comparing spectra generated from different orbitals, electronic nematic behaviour could be deduced that deviated from the structural anisotropy. Examining five samples with varying isovalent and heterovalent dopant concentrations, we observed a usual onset of an electronic nematic phase at the structural transition, and in one case an absence of the phase. We also recorded the temperature dependence of the CDW peak in these samples which behaves similarly. It too was absent in only one sample, but not in the same sample. Most interestingly, the CDW onset at a lower temperature in $La_{1.65}Eu_{0.2}Sr_{0.15}CuO_4$, where it was seen to enhance the intensity of the electronic nematicity. We argued that the three symmetry breaking phases (the LTT structure, CDW, and electronic nematicity) tend to coexist and may enhance one another, but their different doping- and temperature-dependencies implied a nontrivial connection. An underlying mechanism could be the magnitude of the structural tilt that could induce an electronic nematic phase above some critical value, and then enhance its strength thereafter. As seen in our sample, the electronic nematicity may then interact with the CDW phase, and thus directly or indirectly suppress superconductivity.

In Chapter 5, near-edge XAS spectra were measured at the Cu L and O K edges for three dopings of YBCO; with $\delta = 0.335$, $\delta = 0.5$, and $\delta = 0.999$. We hypothesized that an electronic nematic phase would manifest as a relative change in the temperature evolution of these spectra such that the spontaneous onset of additional anisotropy would be apparent. We examined and characterized the observable changes in the spectra. This most commonly included the reduction and broadening of peaks, some more dramatically than others, that spanned both absorption edges, all dopings, and all polarizations. In contrast, the peaks associated with the upper Hubbard band and the twin peaks in the c-axis spectra showed an increase of intensity with temperature. Substantial spectral weight was also added in the region just below the upper Hubbard band. We proposed that phonon coupling through a Franck-Condon mechanism could be responsible. The x-ray linear dichroism was also calculated between the a- and b-axis data where electronic nematicity was expected to be the most dramatic in the CuO_2 plane states. Ultimately, only subtle changes to the anisotropy were observed, and the presence of an electronic nematic phase could not be verified. Instead, our results provided an upper limit on the visibility of any effects from this phase that may help guide future work.

Going forward, our research naturally extends into further studies. Large datasets

spanning multiple branches of the cuprate family tree—and many dopings along each branch—are required to convincingly establish the universal presence or absence of the electronic orders and their properties that we have studied. Measuring the symmetry of the CDW in more samples as we did here for LBCO and YBCO could provide valuable insight into its generic structure, and doing so at a series of orientations that varied in L could increase the precision of the findings. Additionally, this work would benefit from an improvement in the model for the scattering tensor that could remove ambiguity in the interpretation of data and perhaps extend its applicability to additional orbitals that are less directly involved in the CDW. As we showed in our own data, this RSXS experiment has the potential to map out complicated forms of a CDW, including those with multiple modulating parameters, and thus any further refinements could provide crucial insights about this important and intensely studied phase. Similarly, our study of the electronic nematic phase in La-based cuprates would benefit from additional dopings. As discussed earlier, exploring the two-dimensional doping space of carrier concentration and unit cell volume would allow for a more robust analysis of how these properties affect this phase and its relationship to CDW order and structural anisotropy. Unfortunately, this experimental method is inherent to La-based cuprates and cannot be performed on other families, but the establishment of electronic nematicity as a common form of ordering here justifies more focussed efforts to find it elsewhere by other means. It would also be very interesting to see if the onset of CDW order enhances electronic nematicity, or vice versa, in other materials like was seen here in $La_{1.65}Eu_{0.2}Sr_{0.15}CuO_4$. This could be done in YBCO, for example, where there is compelling evidence from other techniques that electronic nematicity is present. Additionally, further investigations of anomalous spectra, such as seen here for Eu in $La_{1.65}Eu_{0.2}Sr_{0.15}CuO_4$ or O in $La_{1.905}Ba_{0.095}CuO_4$, could lead to unexpected insight if the results can be consistently reproduced. Finally, though our investigation of electronic nematicity using near-edge XAS in YBCO provided a null result, it would be beneficial to repeat the procedure on more materials and continue the search for this important phase. Doing so in conjunction with other probes for electronic nematicity, and/or on materials where the phase is more certain to be present, could improve confidence in the effectiveness of this method, or else confirm that the effects are too weak to be reliably observed.

Ultimately, it is our hope that the research presented here has contributed another step in the right direction on the path to understanding the complex interactions of electrons in the cuprates. Perhaps it will inspire a new experiment or study that yields a critical insight leading to the long-hoped-for unifying microscopic theory of these intricate ordering phases.

References

[1] P Abbamonte, A Rusydi, S Smadici, G D Gu, G A Sawatzky, and D L Feng. Spatially modulated 'Mottness' in $La_{2-x}Ba_xCuO_4$. *Nat. Phys.*, 1(3):155–158, Dec 2005.

[2] D. J. Huang, H.-J. Lin, J. Okamoto, K. S. Chao, H.-T. Jeng, G. Y. Guo, C.-H. Hsu, C.-M. Huang, D. C. Ling, W. B. Wu, C. S. Yang, and C. T. Chen. Charge-Orbital Ordering and Verwey Transition in Magnetite Measured by Resonant Soft X-Ray Scattering. *Phys. Rev. Lett.*, 96(9):096401, Mar 2006.

[3] P. Abbamonte, G. Blumberg, A. Rusydi, A. Gozar, P. G. Evans, T. Siegrist, L. Venema, H. Eisaki, E. D. Isaacs, and G. A. Sawatzky. Crystallization of charge holes in the spin ladder of $Sr_{14}Cu_{24}O_{41}$. *Nature*, 431(7012):1078–1081, Oct 2004.

[4] K. J. Thomas, J. P. Hill, S. Grenier, Y. J. Kim, P. Abbamonte, L. Venema, A. Rusydi, Y. Tomioka, Y. Tokura, D. F. McMorrow, G. Sawatzky, and M. Van Veenendaal. Soft x-ray resonant diffraction study of magnetic and orbital correlations in a manganite near half doping. *Phys. Rev. Lett.*, 92(23):2–5, 2004.

[5] S. B. Wilkins, P. D. Spencer, P. D. Hatton, S. P. Collins, M. D. Roper, D. Prabhakaran, and A. T. Boothroyd. Direct Observation of Orbital Ordering in $La_{0.5}Sr_{1.5}MnO_4$ Using Soft X-ray Diffraction. *Phys. Rev. Lett.*, 91(16):167205, Oct 2003.

[6] C. Schüßler-Langeheine, J. Schlappa, A. Tanaka, Z. Hu, C. F. Chang, E. Schierle, M. Benomar, H. Ott, E. Weschke, G. Kaindl, O. Friedt, G. A. Sawatzky, H.-J. Lin, C. T. Chen, M. Braden, and L. H. Tjeng. Spectroscopy of Stripe Order in $La_{1.8}Sr_{0.2}NiO_4$ Using Resonant Soft X-Ray Diffraction. *Phys. Rev. Lett.*, 95(15):156402, Oct 2005.

[7] R. Comin, R. Sutarto, F. He, E. H. da Silva Neto, L. Chauviere, A. Fraño, R. Liang, W. N. Hardy, D. A. Bonn, Y. Yoshida, H. Eisaki, A. J. Achkar, D. G. Hawthorn,

B. Keimer, G. A. Sawatzky, and A. Damascelli. Symmetry of charge order in cuprates. *Nat. Mater.*, 14(8):796–800, 2015.

[8] A. J. Achkar, F. He, R. Sutarto, Christopher McMahon, M. Zwiebler, M. Hücker, G. D. Gu, Ruixing Liang, D. A. Bonn, W. N. Hardy, J. Geck, and D. G. Hawthorn. Orbital symmetry of charge-density-wave order in $La_{1.875}Ba_{0.125}CuO_4$ and $YBa_2Cu_3O_{6.67}$. *Nat. Mater.*, 15(6):616–620, Feb 2016.

[9] A J Achkar, M Zwiebler, Christopher McMahon, F He, R Sutarto, Isaiah Djianto, Zhihao Hao, G D Gu, A Revcolevschi, H Zhang, Y Kim, J Geck, and D G Hawthorn. Nematicity in stripe ordered cuprates probed via resonant x-ray scattering. *Science*, 351(001):1–5, 2016.

[10] A. J. Achkar, X. Mao, Christopher McMahon, R. Sutarto, F. He, Ruixing Liang, D. a. Bonn, W. N. Hardy, and D. G. Hawthorn. Impact of Quenched Oxygen Disorder on Charge Density Wave Order in $YBa_2Cu_3O_{6+x}$. *Phys. Rev. Lett.*, 113(10):107002, Sep 2014.

[11] Haofei Wei, Chiara Sacco, Alice Galdi, Christopher McMahon, Jacob Ruf, Tianyu Shi, Cissy Suen, Carolina Adamo, John Harter, Ronny Sutarto, Feizhou He, Luigi Maritato, Darrell Schlom, and David Hawthorn. Non-collinear charge correlations with $8a_0$ periodicity in the prototypical electron-doped cuprate $sr_{1-x}la_xcuo_2$. *Nature Communications*. Manuscript submitted for publication.

[12] H Zhang, N Gauquelin, C McMahon, D G Hawthorn, G A Botton, and J Y T Wei. Synthesis of high-oxidation Y-Ba-Cu-O phases in superoxygenated thin films. *Phys. Rev. Mater.*, 2(3):33803, 2018.

[13] H. Zhang, N. Gauquelin, C. McMahon, D.G. Hawthorn, G.A. Botton, and J.Y.T. Wei. Phase conversion of y-ba-cu-o thin films by super-oxygenation and cu-enrichment. In J. Bonča and S. Kruchinin, editors, *Nanomaterials for Security. NATO Science for Peace and Security Series A: Chemistry and Biology*, pages 45–56. Springer, Dordrecht, 2016.

[14] J. Bardeen, L. N. Cooper, and J. R. Schrieffer. Theory of Superconductivity. *Phys. Rev.*, 108(5):1175–1204, Dec 1957.

[15] J. Bardeen, L. N. Cooper, and J. R. Schrieffer. Microscopic Theory of Superconductivity. *Phys. Rev.*, 106(1):162–164, Apr 1957.

[16] Ernie Tretkoff. Reliving the Good Old Days of Superconductivity. *APS News*, 16(5), 2007.

[17] J G Bednorz and K. A. Müller. Possible highT c superconductivity in the Ba-La-Cu-O system. *Zeitschrift für Phys. B Condens. Matterur*, 64(2):189–193, Jun 1986.

[18] K. A. Müller and J. G. Bednorz. The Discovery of a Class of High-Temperature Superconductors. *Science*, 237(4819):1133–1139, Sep 1987.

[19] J. G. Bednorz, M. Takashige, and K. A. Müller. Susceptibility Measurements Support High-T_c Superconductivity in the Ba-La-Cu-O System. *Europhys. Lett.*, 3(3):379–386, Feb 1987.

[20] Malcolm R. Beasley and Theodore H. Geballe. Superconducting materials. *Phys. Today*, 37(10):60–68, Oct 1984.

[21] Jean Muller. A15-type superconductors. *Reports Prog. Phys.*, 43(5):641–687, May 1980.

[22] Niel W. Ashcroft and N. David Mermin. *Solid State Physics*. Brooks/Cole, Cengage Learning, eighth edition, 1976.

[23] M. K. Wu, J. R. Ashburn, C. J. Torng, P. H. Hor, R. L. Meng, L. Gao, Z. J. Huang, Y. Q. Wang, and C. W. Chu. Superconductivity at 93 K in a new mixed-phase Y-Ba-Cu-O compound system at ambient pressure. *Phys. Rev. Lett.*, 58(9):908–910, Mar 1987.

[24] A. P. Drozdov, M. I. Eremets, I. A. Troyan, V. Ksenofontov, and S. I. Shylin. Conventional superconductivity at 203 kelvin at high pressures in the sulfur hydride system. *Nature*, 525(7567):73–76, Aug 2015.

[25] Yoichi Kamihara, Hidenori Hiramatsu, Masahiro Hirano, Ryuto Kawamura, Hiroshi Yanagi, Toshio Kamiya, and Hideo Hosono. Iron-Based Layered Superconductor: LaOFeP. *J. Am. Chem. Soc.*, 128(31):10012–10013, Aug 2006.

[26] Yoichi Kamihara, Takumi Watanabe, Masahiro Hirano, and Hideo Hosono. Iron-Based Layered Superconductor La[$O_{1-x}F_x$]FeAs (x = 0.05-0.12) with T_c = 26 K. *J. Am. Chem. Soc.*, 130(11):3296–3297, Mar 2008.

[27] Tadashi C. Ozawa and Susan M. Kauzlarich. Chemistry of layered d -metal pnictide oxides and their potential as candidates for new superconductors. *Sci. Technol. Adv. Mater.*, 9(3):033003, Jul 2008.

[28] Andrew Achkar. *Charge Density Wave Order in Cuprate Superconductors Studied by Resonant Soft X-ray Scattering*. PhD thesis, University of Waterloo, Waterloo, Ontario, Canada, 2015.

[29] John M. Tranquada. Spins, stripes, and superconductivity in hole-doped cuprates. In *AIP Conf. Proc.*, volume 1550, pages 114–187, May 2013.

[30] M R Norman and C Pépin. The electronic nature of high temperature cuprate superconductors. *Reports Prog. Phys.*, 66(10):1547–1610, Oct 2003.

[31] J. Orenstein and A. J. Millis. Advances in the Physics of High-Temperature Superconductivity. *Science*, 288(5465):468–474, Apr 2000.

[32] J Fink, N. Nücker, E. Pellegrin, H Romberg, M Alexander, and M Knupfer. Electron energy-loss and x-ray absorption spectroscopy of cuprate superconductors and related compounds. *J. Electron Spectros. Relat. Phenomena*, 66(3-4):395–452, Jan 1994.

[33] Andrea Damascelli, Zahid Hussain, and Zhi-Xun Shen. Angle-resolved photoemission studies of the cuprate superconductors. *Rev. Mod. Phys.*, 75(2):473–541, Apr 2003.

[34] Warren E. Pickett. Electronic structure of the high-temperature oxide superconductors. *Rev. Mod. Phys.*, 61(2):433–512, Apr 1989.

[35] Tom Timusk and Bryan Statt. The pseudogap in high-temperature superconductors: an experimental survey. *Reports Prog. Phys.*, 62(1):61–122, Jan 1999.

[36] L. P. Gor'kov. Microscopic Derivation of the Ginzburg-Landau Equations in the Theory of Superconductivity. *J. Exp. Theor. Phys.*, 9(6):1364–1367, 1959.

[37] J. P. Carbotte. Properties of boson-exchange superconductors. *Rev. Mod. Phys.*, 62(4):1027–1157, Oct 1990.

[38] Mark Buchanan. Mind the pseudogap. *Nature*, 409(6816):8–11, Jan 2001.

[39] P. W. Anderson. The Resonating Valence Bond State in La_2CuO_4 and Superconductivity. *Science*, 235(4793):1196–1198, Mar 1987.

[40] D. A. Wollman, D. J. Van Harlingen, W. C. Lee, D. M. Ginsberg, and A. J. Leggett. Experimental determination of the superconducting pairing state in YBCO from the phase coherence of YBCO-Pb dc SQUIDs. *Phys. Rev. Lett.*, 71(13):2134–2137, Sep 1993.

[41] C. C. Tsuei, J. R. Kirtley, C. C. Chi, Lock See Yu-Jahnes, A. Gupta, T. Shaw, J. Z. Sun, and M. B. Ketchen. Pairing Symmetry and Flux Quantization in a Tricrystal Superconducting Ring of $YBa_2Cu_3O_{7-\delta}$. *Phys. Rev. Lett.*, 73(4):593–596, Jul 1994.

[42] Z.-X. Shen, D. S. Dessau, B. O. Wells, D. M. King, W. E. Spicer, A. J. Arko, D. Marshall, L. W. Lombardo, A. Kapitulnik, P. Dickinson, S. Doniach, J. DiCarlo, T. Loeser, and C. H. Park. Anomalously large gap anisotropy in the $a-b$ plane of $Bi_2Sr_2CaCu_2O_{8+\delta}$. *Phys. Rev. Lett.*, 70(10):1553–1556, Mar 1993.

[43] H Ding, J. C. Campuzano, A. F. Bellman, T. Yokoya, M. R. Norman, M Randeria, T. Takahashi, H. Katayama-Yoshida, T. Mochiku, K. Kadowaki, and G. Jennings. Momentum Dependence of the Superconducting Gap in $Bi_2Sr_2CaCu_2O_8$. *Phys. Rev. Lett.*, 74(14):2784–2787, Apr 1995.

[44] R J Kelley, Jian Ma, C. Quitmann, G. Margaritondo, and M. Onellion. Superconducting gap and order parameter in $Bi_2Sr_2CaCu_2O_{8+x}$. *Phys. Rev. B*, 50(1):590–593, Jul 1994.

[45] Makoto Hashimoto, Inna M. Vishik, Rui-Hua He, Thomas P. Devereaux, and Zhi-Xun Shen. Energy gaps in high-transition-temperature cuprate superconductors. *Nat. Phys.*, 10(7):483–495, Jul 2014.

[46] P. Monthoux, D. Pines, and G. G. Lonzarich. Superconductivity without phonons. *Nature*, 450(7173):1177–1183, 2007.

[47] W. S. Lee, I. M. Vishik, K. Tanaka, D. H. Lu, T. Sasagawa, N. Nagaosa, T. P. Devereaux, Z. Hussain, and Z.-X. Shen. Abrupt onset of a second energy gap at the superconducting transition of underdoped Bi2212. *Nature*, 450(7166):81–84, Nov 2007.

[48] J M Tranquada, D E Cox, W Kunnmann, H Moudden, G Shirane, M Suenaga, P Zolliker, D Vaknin, S K Sinha, M S Alvarez, A. J. Jacobson, and D. C. Johnston. Neutron-Diffraction Determination of Antiferromagnetic Structure of Cu Ions in $YBa_2Cu_3O_{6+x}$ with $x = 0.0$ and 0.15. *Phys. Rev. Lett.*, 60(2):156–159, Jan 1988.

[49] David G. Hawthorn. *Thermal conduction in the high temperature superconductors LSCO and Tl2201: A field and doping dependent study.* PhD thesis, University of Toronto, Toronto, Ontario, Canada, 2005.

[50] D J Scalapino and S R White. Superconducting condensation energy and an antiferromagnetic exchange-based pairing mechanism. *Phys. Rev. B*, 58(13):8222–8224, Oct 1998.

[51] D. J. Scalapino. The Cuprate Pairing Mechanism. *Science*, 284(5418):1282–1283, May 1999.

[52] Louis Taillefer. Scattering and Pairing in Cuprate Superconductors. *Annu. Rev. Condens. Matter Phys.*, 1(1):51–70, Aug 2010.

[53] Riccardo Comin. Resonant x-ray studies of electronic orders in quantum solids. Retrieved from the University of Minnesota Digital Conservancy, 2018.

[54] I M Vishik. Photoemission perspective on pseudogap, superconducting fluctuations, and charge order in cuprates: a review of recent progress. *Reports Prog. Phys.*, 81(6):062501, Jun 2018.

[55] J. M. Harris, Z. X. Shen, P. J. White, D. S. Marshall, M. C. Schabel, J. N. Eckstein, and I. Bozovic. Anomalous superconducting state gap size versus T_c behavior in underdoped $Bi_2Sr_2Ca_{1-x}Dy_xCu_2O_{8+\delta}$. *Phys. Rev. B*, 54(22):R15665–R15668, Dec 1996.

[56] H. Ding, T. Yokoya, J. C. Campuzano, T. Takahashi, M. Randeria, M. R. Norman, T. Mochiku, K. Kadowaki, and J. Giapintzakis. Spectroscopic evidence for a pseudogap in the normal state of underdoped high-T_c superconductors. *Nature*, 382(6586):51–54, Jul 1996.

[57] A G Loeser, Z.-X. Shen, D S Dessau, D S Marshall, C H Park, P Fournier, and A Kapitulnik. Excitation Gap in the Normal State of Underdoped $Bi_2Sr_2CaCu_2O_{8+\delta}$. *Science*, 273(5273):325–329, Jul 1996.

[58] V. J. Emery and S. A. Kivelson. Importance of phase fluctuations in superconductors with small superfluid density. *Nature*, 374(6521):434–437, Mar 1995.

[59] J Corson, R Mallozzi, J Orenstein, J. N. Eckstein, and I. Bozovic. Vanishing of phase coherence in underdoped $Bi_2Sr_2CaCu_2O_{8+\delta}$. *Nature*, 398(6724):221–223, Mar 1999.

[60] Z A Xu, N P Ong, Y Wang, T Kakeshita, and S Uchida. Vortex-like excitations and the onset of superconducting phase fluctuation in underdoped $La_{2-x}Sr_xCuO_4$. *Nature*, 406(6795):486–488, Aug 2000.

[61] J. M. Tranquada, J. M. Tranquada, B. J. Sternlieb, B. J. Sternlieb, J. D. Axe, J. D. Axe, Y. Nakamura, Y. Nakamura, S. Uchida, and S. Uchida. Evidence for stripe correlations of spins and holes in copper oxide superconductors, 1995.

[62] K. McElroy, R. W. Simmonds, J. E. Hoffman, D.-H. Lee, J. Orenstein, H. Eisaki, S. Uchida, and J. C. Davis. Relating atomic-scale electronic phenomena to wave-like quasiparticle states in superconducting $Bi_2Sr_2CaCu_2O_{8+\delta}$. *Nature*, 422(6932):592–596, Apr 2003.

[63] T. Hanaguri, C. Lupien, Y. Kohsaka, D.-H. Lee, M. Azuma, M. Takano, H. Takagi, and J. C. Davis. A 'checkerboard' electronic crystal state in lightly hole-doped $Ca_{2-x}Na_xCuO_2Cl_2$. *Nature*, 430(7003):1001–1005, Aug 2004.

[64] Riccardo Comin and Andrea Damascelli. Resonant X-Ray Scattering Studies of Charge Order in Cuprates. *Annu. Rev. Condens. Matter Phys.*, 7(1):369–405, Mar 2016.

[65] D. G. Hawthorn, K. M. Shen, J. Geck, D. C. Peets, H. Wadati, J. Okamoto, S.-W. Huang, D. J. Huang, H.-J. Lin, J. D. Denlinger, Ruixing Liang, D. a. Bonn, W. N. Hardy, and G. a. Sawatzky. Resonant elastic soft x-ray scattering in oxygen-ordered $YBa_2Cu_3O_{6+\delta}$. *Phys. Rev. B*, 84(7):075125, Aug 2011.

[66] G Ghiringhelli, M Le Tacon, M Minola, S Blanco-Canosa, C Mazzoli, N B Brookes, G M De Luca, A Frano, D G Hawthorn, F He, T Loew, M Moretti Sala, D C Peets, M Salluzzo, E Schierle, R Sutarto, G a Sawatzky, E Weschke, B Keimer, and L Braicovich. Long-range incommensurate charge fluctuations in $(Y,Nd)Ba_2Cu_3O_{6+x}$. *Science*, 337(6096):821–5, Aug 2012.

[67] A. J. Achkar, F. He, R. Sutarto, J. Geck, H. Zhang, Y.-J. Kim, and D. G. Hawthorn. Resonant X-Ray Scattering Measurements of a Spatial Modulation of the Cu $3d$ and O $2p$ Energies in Stripe-Ordered Cuprate Superconductors. *Phys. Rev. Lett.*, 110(1):017001, Jan 2013.

[68] R. Comin, R. Sutarto, E. H. Da Silva Neto, L. Chauviere, R. Liang, W. N. Hardy, D. a. Bonn, F. He, G. a. Sawatzky, and A. Damascelli. Broken translational and rotational symmetry via charge stripe order in underdoped $YBa_2Cu_3O_{6+y}$. *Science*, 347(6228):1335–1339, 2015.

[69] W. Tabis, Y. Li, M. Le Tacon, L. Braicovich, A. Kreyssig, M. Minola, G. Dellea, E. Weschke, M. J. Veit, M. Ramazanoglu, A. I. Goldman, T. Schmitt, G. Ghiringhelli,

N. Barišić, M. K. Chan, C. J. Dorow, G. Yu, X. Zhao, B. Keimer, and M. Greven. Charge order and its connection with Fermi-liquid charge transport in a pristine high-T_c cuprate. *Nat. Commun.*, 5(1):5875, Dec 2014.

[70] H.-H. Wu, M. Buchholz, C. Trabant, C.F. Chang, A.C. Komarek, F. Heigl, M.v. Zimmermann, M. Cwik, F. Nakamura, M. Braden, and C. Schüßler-Langeheine. Charge stripe order near the surface of 12-percent doped $La_{2-x}Sr_xCuO_4$. *Nat. Commun.*, 3(1):1023, Jan 2012.

[71] J. Chang, E. Blackburn, A. T. Holmes, N. B. Christensen, J. Larsen, J. Mesot, Ruixing Liang, D. A. Bonn, W. N. Hardy, A. Watenphul, M. v. Zimmermann, E. M. Forgan, and S. M. Hayden. Direct observation of competition between superconductivity and charge density wave order in $YBa_2Cu_3O_y$. *Nat. Phys.*, 8(12):871–876, 2012.

[72] S. A. Kivelson, E. Fradkin, and V. J. Emery. Electronic liquid-crystal phases of a doped Mott insulator. *Nature*, 393(6685):550–553, Jun 1998.

[73] V J Emery, S a Kivelson, and J M Tranquada. Stripe phases in high-temperature superconductors. *Proc. Natl. Acad. Sci.*, 96(16):8814–8817, Aug 1999.

[74] Jan Zaanen and Olle Gunnarsson. Charged magnetic domain lines and the magnetism of high-T_c oxides. *Phys. Rev. B*, 40(10):7391–7394, Oct 1989.

[75] S. A. Kivelson, I. P. Bindloss, E. Fradkin, V. Oganesyan, J. M. Tranquada, A. Kapitulnik, and C. Howald. How to detect fluctuating stripes in the high-temperature superconductors. *Rev. Mod. Phys.*, 75(4):1201–1241, Oct 2003.

[76] S. Sachdev and Shou-Cheng Zhang. Tuning Order in Cuprate Superconductors. *Science*, 295(5554):452–454, Jan 2002.

[77] F. W. Lytle, D. E. Sayers, and E. A. Stern. Extended x-ray-absorption fine-structure technique. II. Experimental practice and selected results. *Phys. Rev. B*, 11(12):4825–4835, Jun 1975.

[78] E A Stern. The Analysis of Materials by X-Ray Absorption. *Sci. Am.*, 234(4):96–103, Apr 1976.

[79] D.C. Koningsberger and R. Prins. *X-ray absorption: principles, applications, techniques of EXAFS, SEXAFS, and XANES*. 1 1988.

[80] F de Groot. High-resolution X-ray emission and X-ray absorption spectroscopy. *Chem. Rev.*, 101(6):1779–808, Jun 2001.

[81] Frank de Groot and Akio Kotani. *Core Level Spectroscopy of Solids*. CRC Press, 2008.

[82] J. J. Rehr and RC C. Albers. Theoretical approaches to x-ray absorption fine structure. *Rev. Mod. Phys.*, 72(3):621–654, 2000.

[83] Heiko Wende. Recent advances in x-ray absorption spectroscopy. *Reports Prog. Phys.*, 67(12):2105–2181, 2004.

[84] J. Stöhr and H. C. Siegmann. *Magnetism: From Fundamentals to Nanoscale Dynamics*. Springer, 2006.

[85] Stefan Hüfner. *Photoelectron Spectroscopy: Principles and Applications*. Springer, 2003.

[86] L A Grunes. Study of the K edges of $3d$ transition metals in pure and oxide form by x-ray-absorption spectroscopy. *Phys.Rev.B.*, 27(4):2111, 1983.

[87] S Eisebitt, T Boske, J E Rubensson, and W Eberhardt. Determination of Absorption-Coefficients for Concentrated Samples by Fluorescence Detection. *Phys. Rev. B*, 47(21):103–109, 1993.

[88] F M F de Groot. X-ray absorption spectroscopy and dichroism of transition metals and their compounds. *J. Electron Spectros. Relat. Phenomena*, 67:529–622, 1994.

[89] A. J. Achkar, T. Z. Regier, H. Wadati, Y.-J. Kim, H. Zhang, and D. G. Hawthorn. Bulk sensitive x-ray absorption spectroscopy free of self-absorption effects. *Phys. Rev. B*, 83(8):081106, Feb 2011.

[90] A J Achkar, T Z Regier, E J Monkman, K M Shen, and D G Hawthorn. Determination of total x-ray absorption coefficient using non-resonant x-ray emission. *Sci. Rep.*, 1:182, Jan 2011.

[91] A. J. Achkar, T. Z. Regier, E. J. Monkman, K. M. Shen, and D. G. Hawthorn. Determination of total x-ray absorption coefficient using non-resonant x-ray emission. *Sci. Rep.*, 1:182, Jan 2011.

[92] Roger Grinter. *The Quantum in Chemistry: An Experimentalist's View*. John Wiley & Sons, 2005.

[93] P. A. M. Dirac. The Quantum Theory of the Emission and Absorption of Radiation. *Proc. R. Soc. A Math. Phys. Eng. Sci.*, 114(767):243–265, Mar 1927.

[94] J Fink, E Schierle, E Weschke, and J Geck. Resonant elastic soft x-ray scattering. *Reports Prog. Phys.*, 76(5):056502, 2013.

[95] Charles Kittel. *Introduction to Solid State Physics*. John Wiley & Sons, Inc., eigth edition, 2005.

[96] Jens Als-Nielsen and Des McMorrow. *Elements of Modern X-Ray Physics*. John Wiley & Sons, Ltd., 2001.

[97] John David Jackson. *Classical Electrodynamics*. John Wiley & Sons, Inc., third edition, 1999.

[98] H. A. Kramers and W. Heisenberg. Über die Streuung von Strahlung durch Atome. *Zeitschrift für Phys. A Hadron. Nucl.*, 31(1):681–708, 1925.

[99] Albert Messiah. *Quantum Mechanics*. Wiley, 1958.

[100] Leonard I. Schiff. *Quantum Mechanics*. McGraw-Hill, third edition, 1968.

[101] Franz Mandl and Graham Shaw. *Quantum Field Theory*. John Wiley & Sons, 2010.

[102] A. J. Achkar, R. Sutarto, X. Mao, F. He, A. Frano, S. Blanco-Canosa, M. Le Tacon, G. Ghiringhelli, L. Braicovich, M. Minola, M. Moretti Sala, C. Mazzoli, Ruixing Liang, D. a. Bonn, W. N. Hardy, B. Keimer, G. a. Sawatzky, and D. G. Hawthorn. Distinct Charge Orders in the Planes and Chains of Ortho-III-Ordered $YBa_2Cu_3O_{6+\delta}$ Superconductors Identified by Resonant Elastic X-ray Scattering. *Phys. Rev. Lett.*, 109(16):167001, Oct 2012.

[103] Tao Wu, Hadrien Mayaffre, Steffen Krämer, Mladen Horvatić, Claude Berthier, W. N. Hardy, Ruixing Liang, D. A. Bonn, and Marc-Henri Julien. Magnetic-field-induced charge-stripe order in the high-temperature superconductor $YBa_2Cu_3O_y$. *Nature*, 477(7363):191–194, 2011.

[104] E. Blackburn, J. Chang, M. Hücker, A. T. Holmes, N. B. Christensen, Ruixing Liang, D. A. Bonn, W. N. Hardy, U. Rütt, O. Gutowski, M. V. Zimmermann, E. M. Forgan, and S. M. Hayden. X-ray diffraction observations of a charge-density-wave order in superconducting ortho-II $YBa_2Cu_3O_{6.54}$ single crystals in zero magnetic field. *Phys. Rev. Lett.*, 110(13):1–5, 2013.

[105] R Comin, A Frano, M M Yee, Y Yoshida, H Eisaki, E Schierle, E Weschke, R Sutarto, F He, A Soumyanarayanan, Yang He, M Le Tacon, I S Elfimov, Jennifer E Hoffman, G A Sawatzky, B Keimer, and A Damascelli. Charge Order Driven by Fermi-Arc Instability in $Bi_2Sr_{2-x}La_xCuO_{6+d}$. *Science*, 343(January):390–392, 2014.

[106] E. H. da Silva Neto, P. Aynajian, A. Frano, R. Comin, E. Schierle, E. Weschke, A. Gyenis, J. Wen, J. Schneeloch, Z. Xu, S. Ono, G. Gu, M. Le Tacon, and A. Yazdani. Ubiquitous Interplay Between Charge Ordering and High-Temperature Superconductivity in Cuprates. *Science*, 343(6169):393–396, Jan 2014.

[107] Y. Kohsaka, C. Taylor, K. Fujita, A. Schmidt, C. Lupien, T. Hanaguri, M. Azuma, M. Takano, H. Eisaki, H. Takagi, S. Uchida, and J. C. Davis. An Intrinsic Bond-Centered Electronic Glass with Unidirectional Domains in Underdoped Cuprates. *Science*, 315(5817):1380–1385, 2007.

[108] Subir Sachdev and Rolando La Placa. Bond order in two-dimensional metals with antiferromagnetic exchange interactions. *Phys. Rev. Lett.*, 111(2):1–5, 2013.

[109] K. B. Efetov, H. Meier, and C. Pépin. Pseudogap state near a quantum critical point. *Nat. Phys.*, 9(7):442–446, 2013.

[110] Kangjun Seo, Han Dong Chen, and Jiangping Hu. d-wave checkerboard order in cuprates. *Phys. Rev. B - Condens. Matter Mater. Phys.*, 76(2):1–4, 2007.

[111] Matthias Vojta and Oliver Rösch. Superconducting d-wave stripes in cuprates: Valence bond order coexisting with nodal quasiparticles. *Phys. Rev. B - Condens. Matter Mater. Phys.*, 77(9):1–5, 2008.

[112] W. A. Atkinson, A. P. Kampf, and S. Bulut. Charge order in the pseudogap phase of cuprate superconductors. *New J. Phys.*, 17(1):13025, 2015.

[113] M. J. Lawler, K. Fujita, Jhinhwan Lee, A. R. Schmidt, Y. Kohsaka, Chung Koo Kim, H. Eisaki, S. Uchida, J. C. Davis, J. P. Sethna, and Eun Ah Kim. Intra-unit-cell electronic nematicity of the high-T_c copper-oxide pseudogap states. *Nature*, 466(7304):347–351, 2010.

[114] Jian-Xin Li, Chang-Qin Wu, and Dung-Hai Lee. Checkerboard charge density wave and pseudogap of high-T_c cuprate. *Phys. Rev. B*, 74(18):184515, Nov 2006.

[115] Andrea Allais, Johannes Bauer, and Subir Sachdev. Density wave instabilities in a correlated two-dimensional metal. *Phys. Rev. B - Condens. Matter Mater. Phys.*, 90(15):1–5, 2014.

[116] Debanjan Chowdhury and Subir Sachdev. Density-wave instabilities of fractionalized Fermi liquids. *Phys. Rev. B - Condens. Matter Mater. Phys.*, 90(24):1–10, 2014.

[117] K. Fujita, M. H. Hamidian, S. D. Edkins, C. K. Kim, Y. Kohsaka, M. Azuma, M. Takano, H. Takagi, H. Eisaki, S.-i. Uchida, A. Allais, M. J. Lawler, E.-A. Kim, S. Sachdev, and J. C. S. Davis. Direct phase-sensitive identification of a d-form factor density wave in underdoped cuprates. *Proc. Natl. Acad. Sci.*, 111(30):E3026–E3032, 2014.

[118] M. Hücker, M. v. Zimmermann, G. D. Gu, Z. J. Xu, J. S. Wen, Guangyong Xu, H. J. Kang, A. Zheludev, and J. M. Tranquada. Stripe order in superconducting $La_{2-x}Ba_xCuO_4$ ($0.095 \leq x \leq 0.155$). *Phys. Rev. B*, 83(10):104506, Mar 2011.

[119] S. Blanco-Canosa, A. Frano, E. Schierle, J. Porras, T. Loew, M. Minola, M. Bluschke, E. Weschke, B. Keimer, and M. Le Tacon. Resonant x-ray scattering study of charge-density wave correlations in $YBa_2Cu_3O_{6+x}$. *Phys. Rev. B*, 90(5):054513, Aug 2014.

[120] M. Hücker, N. B. Christensen, A. T. Holmes, E. Blackburn, E. M. Forgan, Ruixing Liang, D. A. Bonn, W. N. Hardy, O. Gutowski, M. V. Zimmermann, S. M. Hayden, and J. Chang. Competing charge, spin, and superconducting orders in underdoped YBa2 Cu3 Oy. *Phys. Rev. B - Condens. Matter Mater. Phys.*, 90(5):1–11, 2014.

[121] Kazuhiro Fujita, Andrew R. Schmidt, Eun-Ah Kim, Michael J. Lawler, Dung Hai Lee, J. C. Davis, Hiroshi Eisaki, and Shin-ichi Uchida. Spectroscopic Imaging Scanning Tunneling Microscopy Studies of Electronic Structure in the Superconducting and Pseudogap Phases of Cuprate High-T_c Superconductors. *J. Phys. Soc. Japan*, 81(1):011005, 2012.

[122] W. D. Wise, M. C. Boyer, Kamalesh Chatterjee, Takeshi Kondo, T. Takeuchi, H. Ikuta, Yayu Wang, and E. W. Hudson. Charge-density-wave origin of cuprate checkerboard visualized by scanning tunnelling microscopy. *Nat. Phys.*, 4(9):696–699, 2008.

[123] K. Yamada, C. H. Lee, K. Kurahashi, J. Wada, S. Wakimoto, S. Ueki, H. Kimura, Y. Endoh, S. Hosoya, G. Shirane, R. J. Birgeneau, M. Greven, M. A. Kastner, and Y. J. Kim. Doping dependence of the spatially modulated dynamical spin correlations and the superconducting-transition temperature in $La_{2-x}Sr_xCuO_4$. *Phys. Rev. B*, 57(10):6165–6172, 1998.

[124] S. Blanco-Canosa, A. Frano, T. Loew, Y. Lu, J. Porras, G. Ghiringhelli, M. Minola, C. Mazzoli, L. Braicovich, E. Schierle, E. Weschke, M. Le Tacon, and B. Keimer.

Momentum-dependent charge correlations in $YBa_2Cu_3O_{6+\delta}$superconductors probed by resonant x-ray scattering: Evidence for three competing phases. *Phys. Rev. Lett.*, 110(18):1–5, 2013.

[125] X.L Yan, J.F Zhou, X.J Niu, X.L Chen, Q.Y Tu, and X Wu. Crystal growth of La_2CuO_4 and $La_{2-x}Ba_xCuO_4$ by the travelling-solvent floating zone method. *J. Cryst. Growth*, 242(1-2):161–166, Jul 2002.

[126] Ruixing Liang, D A Bonn, and W N Hardy. Growth of high quality YBCO single crystals using $BaZrO_3$ crucibles. *Phys. C*, 304(1-2):105–111, 1998.

[127] D G Hawthorn, F He, L Venema, H Davis, a J Achkar, J Zhang, R Sutarto, H Wadati, a Radi, T Wilson, G Wright, K M Shen, J Geck, H Zhang, V Novák, and G a Sawatzky. An in-vacuum diffractometer for resonant elastic soft x-ray scattering. *Rev. Sci. Instrum.*, 82(7):073104, Jul 2011.

[128] Young-June Kim, G. D. Gu, T. Gog, and D. Casa. X-ray scattering study of charge density waves in $La_{2-x}Ba_xCuO_4$. *Phys. Rev. B*, 77(6):064520, Feb 2008.

[129] Jörg Fink, Victor Soltwisch, Jochen Geck, Enrico Schierle, Eugen Weschke, and Bernd Büchner. Phase diagram of charge order in $La_{1.8-x}Eu_{0.2}Sr_xCuO_4$ from resonant soft x-ray diffraction. *Phys. Rev. B*, 83(9):092503, Mar 2011.

[130] Y Maeno, A Odagawa, N Kakehi, T. Suzuki, and T. Fujita. Structural, normal-state, and superconducting properties of $(La_{1-x}Ba_{x-y}Sr_y)_2CuO_4$. *Phys. C Supercond.*, 173(5-6):322–330, Feb 1991.

[131] Takashi Suzuki and Toshizo Fujita. Anomalous Change in Crystalline Structure of $(La_{1-x}Ba_x)_2CuO_{4-\delta}$. *J. Phys. Soc. Japan*, 58(6):1883–1886, 1989.

[132] V Antal, K Zmorayová, J Kováč, V Kavečanský, P Diko, M Eisterer, and H W Weber. The influence of annealing in flowing argon on the microstructural and superconducting properties of Al doped YBCO bulks. *Supercond. Sci. Technol.*, 23(6):065014, Jun 2010.

[133] Ruixing Liang, D. A. Bonn, and W. N. Hardy. Evaluation of CuO_2 plane hole doping in $YBa_2Cu_3O_{6+x}$ single crystals. *Phys. Rev. B - Condens. Matter Mater. Phys.*, 73(18):1–4, 2006.

[134] Arno P. Kampf, Douglas J. Scalapino, and Steven R. White. Stripe orientation in an anisotropic $t - J$ model. *Phys. Rev. B*, 64(5):052509, Jul 2001.

[135] Matthias Vojta. Lattice symmetry breaking in cuprate superconductors: Stripes, nematics, and superconductivity. *Adv. Phys.*, 58(6):699–820, 2009.

[136] Subir Sachdev. Colloquium: Order and quantum phase transitions in the cuprate superconductors. *Rev. Mod. Phys.*, 75(3):913–932, Jul 2003.

[137] N. B. Christensen, H. M. Rønnow, J. Mesot, R. A. Ewings, N. Momono, M. Oda, M. Ido, M. Enderle, D. F. McMorrow, and A. T. Boothroyd. Nature of the Magnetic Order in the Charge-Ordered Cuprate $La_{1.48}Nd_{0.4}Sr_{0.12}CuO_4$. *Phys. Rev. Lett.*, 98(19):197003, May 2007.

[138] Mark H. Fischer, Si Wu, Michael Lawler, Arun Paramekanti, and Eun Ah Kim. Nematic and spin-charge orders driven by hole-doping a charge-transfer insulator. *New J. Phys.*, 16, 2014.

[139] Max A. Metlitski and Subir Sachdev. Quantum phase transitions of metals in two spatial dimensions. II. Spin density wave order. *Phys. Rev. B*, 82(7):075128, 2010.

[140] Youichi Yamakawa and Hiroshi Kontani. Spin-Fluctuation-Driven Nematic Charge-Density Wave in Cuprate Superconductors: Impact of Aslamazov-Larkin Vertex Corrections. *Phys. Rev. Lett.*, 114(25):257001, Jun 2015.

[141] N.H Andersen, M von Zimmermann, T Frello, M Käll, D Mønster, P.-A Lindgård, J Madsen, T Niemöller, H.F Poulsen, O Schmidt, J.R Schneider, Th Wolf, P Dosanjh, R Liang, and W.N Hardy. Superstructure formation and the structural phase diagram of $YBa_2Cu_3O_{6+x}$. *Phys. C Supercond.*, 317-318:259–269, May 1999.

[142] E. M. Forgan, E. Blackburn, A. T. Holmes, A. K. R. Briffa, J. Chang, L. Bouchenoire, S. D. Brown, Ruixing Liang, D. Bonn, W. N. Hardy, N. B. Christensen, M. V. Zimmermann, M. Hücker, and S. M. Hayden. The microscopic structure of charge density waves in underdoped $YBa_2Cu_3O_{6.54}$ revealed by X-ray diffraction. *Nat. Commun.*, 6:10064, 2015.

[143] Christopher McMahon, A. J. Achkar, E. H. da Silva Neto, I. Djianto, J. Menard, F. He, R. Sutarto, R. Comin, Ruixing Liang, D. A. Bonn, W. N. Hardy, A. Damascelli, and D. G. Hawthorn. Orbital symmetries of charge density wave order in $YBa_2Cu_3O_{6+x}$. Unpublished, 2019.

[144] J. Chang, E. Blackburn, O. Ivashko, A. T. Holmes, N. B. Christensen, M. Hücker, Ruixing Liang, D. A. Bonn, W. N. Hardy, U. Rütt, M. V. Zimmermann, E. M.

Forgan, and S. M. Hayden. Magnetic field controlled charge density wave coupling in underdoped $YBa_2Cu_3O_{6+x}$. *Nat. Commun.*, 7(May):1–7, 2016.

[145] R. A. Borzi, S. A. Grigera, J. Farrell, R. S. Perry, S. J. S. Lister, S. L. Lee, D. A. Tennant, Y. Maeno, and A. P. Mackenzie. Formation of a Nematic Fluid at High Fields in $Sr_3Ru_2O_7$. *Science*, 315(5809):214–217, 2007.

[146] J.-H. Chu, J. G. Analytis, K. De Greve, P. L. McMahon, Z. Islam, Y. Yamamoto, and I. R. Fisher. In-Plane Resistivity Anisotropy in an Underdoped Iron Arsenide Superconductor. *Science*, 329(5993):824–826, Aug 2010.

[147] M. G. Kim, R. M. Fernandes, A. Kreyssig, J. W. Kim, A. Thaler, S. L. Bud'ko, P. C. Canfield, R. J. McQueeney, J. Schmalian, and A. I. Goldman. Character of the structural and magnetic phase transitions in the parent and electron-doped $BaFe_2As_2$ compounds. *Phys. Rev. B*, 83(13):134522, 2011.

[148] S. Kasahara, H. J. Shi, K. Hashimoto, S. Tonegawa, Y. Mizukami, T. Shibauchi, K. Sugimoto, T. Fukuda, T. Terashima, Andriy H. Nevidomskyy, and Y. Matsuda. Electronic nematicity above the structural and superconducting transition in $BaFe_2(As_{1-x}P_x)_2$. *Nature*, 486(7403):382–385, 2012.

[149] K. Nakayama, Y. Miyata, G. N. Phan, T. Sato, Y. Tanabe, T. Urata, K. Tanigaki, and T. Takahashi. Reconstruction of band structure induced by electronic nematicity in an FeSe superconductor. *Phys. Rev. Lett.*, 113(23):1–5, 2014.

[150] H.-H. Kuo, J.-H. Chu, J. C. Palmstrom, S. A. Kivelson, and I. R. Fisher. Ubiquitous signatures of nematic quantum criticality in optimally doped Fe-based superconductors. *Science*, 352(6288):958–962, May 2016.

[151] Yuki Nagai, Hiroki Nakamura, and Masahiko MacHida. Rotational isotropy breaking as proof for spin-polarized Cooper pairs in the topological superconductor $Cu_xBi_2Se_3$. *Phys. Rev. B - Condens. Matter Mater. Phys.*, 86(9):1–5, 2012.

[152] Liang Fu. Odd-parity topological superconductor with nematic order: Application to $Cu_xBi_2Se_3$. *Phys. Rev. B - Condens. Matter Mater. Phys.*, 90(10):1–5, 2014.

[153] S. Davis, Z. Huang, K. Han, Ariando, T. Venkatesan, and V. Chandrasekhar. Signatures of electronic nematicity in (111) $LaAlO_3/SrTiO_3$ interfaces. *Phys. Rev. B*, 97(4):041408, Jan 2018.

[154] Yoichi Ando, Kouji Segawa, Seiki Komiya, and A. N. Lavrov. Electrical Resistivity Anisotropy from Self-Organized One Dimensionality in High-Temperature Superconductors. *Phys. Rev. Lett.*, 88(13):4, 2002.

[155] C. Stock, W. J.L. Buyers, R. Liang, D. Peets, Z. Tun, D. Bonn, W. N. Hardy, and R. J. Birgeneau. Dynamic stripes and resonance in the superconducting and normal phases of $YBa_2Cu_3O_{6.5}$ ortho-II superconductor. *Phys. Rev. B - Condens. Matter Mater. Phys.*, 69(1):1–22, 2004.

[156] V. Hinkov, P. Bourges, S. Pailhès, Y. Sidis, A. Ivanov, C. D. Frost, T. G. Perring, C. T. Lin, D. P. Chen, and B. Keimer. Spin dynamics in the pseudogap state of a high-temperature superconductor. *Nat. Phys.*, 3(11):780–785, 2007.

[157] V Hinkov, D Haug, B. Fauque, P Bourges, Y Sidis, A Ivanov, C Bernhard, C T Lin, and B Keimer. Electronic Liquid Crystal State in the High-Temperature Superconductor $YBa_2Cu_3O_{6.45}$. *Science*, 319(5863):597–600, Feb 2008.

[158] D. Haug, V. Hinkov, Y. Sidis, P. Bourges, N. B. Christensen, A. Ivanov, T. Keller, C. T. Lin, and B. Keimer. Neutron scattering study of the magnetic phase diagram of underdoped $YBa_2Cu_3O_{6+x}$. *New J. Phys.*, 12, 2010.

[159] R. Daou, J. Chang, David Leboeuf, Olivier Cyr-Choinière, Francis Laliberté, Nicolas Doiron-Leyraud, B. J. Ramshaw, Ruixing Liang, D. A. Bonn, W. N. Hardy, and Louis Taillefer. Broken rotational symmetry in the pseudogap phase of a high-T_c superconductor. *Nature*, 463(7280):519–522, 2010.

[160] O. Cyr-Choinière, G. Grissonnanche, S. Badoux, J. Day, D. A. Bonn, W. N. Hardy, R. Liang, N. Doiron-Leyraud, and Louis Taillefer. Two types of nematicity in the phase diagram of the cuprate superconductor $YBa_2Cu_3O_y$. *Phys. Rev. B - Condens. Matter Mater. Phys.*, 92(22):1–7, 2015.

[161] Eduardo Fradkin and Steven A Kivelson. Liquid Crystal Phases of Quantum Hall Systems. *Phys. Rev. B*, 59(12):8065–8079, 1999.

[162] Erez Berg, Eduardo Fradkin, and Steven A. Kivelson. Charge-4e superconductivity from pair-density-wave order in certain high-temperature superconductors. *Nat. Phys.*, 5(11):830–833, 2009.

[163] I Ja Pomeranchuk. On the stability of a Fermi liquid. *Sov. Phys. JETP*, 8:361, 1958.

[164] Vadim Oganesyan, Steven A. Kivelson, and Eduardo Fradkin. Quantum theory of a nematic Fermi fluid. *Phys. Rev. B*, 64(19):195109, Oct 2001.

[165] Eduardo Fradkin, Steven A Kivelson, Michael J Lawler, James P. Eisenstein, and Andrew P Mackenzie. Nematic Fermi Fluids in Condensed Matter Physics. *Annu. Rev. Condens. Matter Phys.*, 1(1):153–178, Aug 2010.

[166] Y. Lubashevsky, Lidong Pan, T. Kirzhner, G. Koren, and N. P. Armitage. Optical Birefringence and Dichroism of Cuprate Superconductors in the THz Regime. *Phys. Rev. Lett.*, 112(14):147001, Apr 2014.

[167] C. Wexler and Alan T. Dorsey. Disclination unbinding transition in quantum Hall liquid crystals. *Phys. Rev. B - Condens. Matter Mater. Phys.*, 64(11):1–5, 2001.

[168] Sudip Chakravarty, R. B. Laughlin, Dirk K. Morr, and Chetan Nayak. Hidden order in the cuprates. *Phys. Rev. B*, 63(9):094503, Jan 2001.

[169] J. Zaanen, Z. Nussinov, and S. I. Mukhin. Duality in 2 + 1D quantum elasticity: Superconductivity and quantum nematic order. *Ann. Phys. (N. Y).*, 310(1):181–260, 2004.

[170] Eugene Demler, Werner Hanke, and Shou Cheng Zhang. SO(5) theory of antiferromagnetism and superconductivity. *Rev. Mod. Phys.*, 76(3 I):909–974, 2004.

[171] Steven A. Kivelson, Eduardo Fradkin, and Theodore H. Geballe. Quasi-one-dimensional dynamics and nematic phases in the two-dimensional Emery model. *Phys. Rev. B - Condens. Matter Mater. Phys.*, 69(14):1–7, 2004.

[172] Kai Sun, Benjamin M. Fregoso, Michael J. Lawler, and Eduardo Fradkin. Fluctuating stripes in strongly correlated electron systems and the nematic-smectic quantum phase transition. *Phys. Rev. B*, 78(8):085124, Aug 2008.

[173] Hae Young Kee, Hyeonjin Doh, and Thomas Grzesiak. Intimate relations between electronic nematic, d-density wave and d-wave superconducting states. *J. Phys. Condens. Matter*, 20(25), 2008.

[174] Kai Sun and Eduardo Fradkin. Time-reversal symmetry breaking and spontaneous anomalous Hall effect in Fermi fluids. *Phys. Rev. B - Condens. Matter Mater. Phys.*, 78(24):1–17, 2008.

[175] Kai Sun, Hong Yao, Eduardo Fradkin, and Steven A. Kivelson. Topological insulators and nematic phases from spontaneous symmetry breaking in 2D fermi systems with a quadratic band crossing. *Phys. Rev. Lett.*, 103(4):1–4, 2009.

[176] A. Mesaros, K. Fujita, H. Eisaki, S. Uchida, J. C. Davis, S. Sachdev, J. Zaanen, M. J. Lawler, and Eun Ah Kim. Topological defects coupling smectic modulations to intra-unit-cell nematicity in cuprates. *Science*, 333(6041):426–430, 2011.

[177] Laimei Nie, Akash V. Maharaj, Eduardo Fradkin, and Steven A. Kivelson. Vestigial nematicity from spin and/or charge order in the cuprates. *Phys. Rev. B*, 96(8):1–11, 2017.

[178] J. Georg Bednorz and K. Alex Müller. Perovskite-type oxides—The new approach to high-T_c superconductivity. *Rev. Mod. Phys.*, 60(3):585–600, Jul 1988.

[179] Guo-meng Zhao, Vidula Kirtikar, and Donald E. Morris. Isotope effects and possible pairing mechanism in optimally doped cuprate superconductors. *Phys. Rev. B*, 63(22):220506, May 2001.

[180] J. D. Axe, A. H. Moudden, D. Hohlwein, D. E. Cox, K. M. Mohanty, A. R. Moodenbaugh, and Youwen Xu. Structural phase transformations and superconductivity in $La_{2-x}Ba_xCuO_4$. *Phys. Rev. Lett.*, 62(23):2751–2754, Jun 1989.

[181] J. D. Axe and M. K. Crawford. Structural instabilities in lanthanum cuprate superconductors. *J. Low Temp. Phys.*, 95(1-2):271–284, 1994.

[182] Tineke Thio, T. R. Thurston, N W Preyer, P. J. Picone, M. A. Kastner, H. P. Jenssen, D. R. Gabbe, C. Y. Chen, R. J. Birgeneau, and Amnon Aharony. Antisymmetric exchange and its influence on the magnetic structure and conductivity of La_2CuO_4. *Phys. Rev. B*, 38(1):905–908, Jul 1988.

[183] M. Hücker. Structural aspects of materials with static stripe order. *Phys. C Supercond. its Appl.*, 481:3–14, 2012.

[184] M. Hücker, M. v. Zimmermann, M. Debessai, J. S. Schilling, J. M. Tranquada, and G. D. Gu. Spontaneous Symmetry Breaking by Charge Stripes in the High Pressure Phase of Superconducting $La_{1.875}Ba_{0.125}CuO_4$. *Phys. Rev. Lett.*, 104(5):057004, Feb 2010.

[185] David H. Templeton and Lieselotte K. Templeton. Polarized X-ray Absorption and Double Refraction in Vanadyl Bisacetylacetonate. *Acta Crystallogr. Sect. A Found. ...*, A36:237–241, 1980.

[186] VE Dmitrienko. Forbidden reflections due to anisotropic X-ray susceptibility of crystals. *Acta Crystallogr. Sect. A Found. ...*, A39(1):29–35, 1983.

[187] B. Büchner, M. Breuer, A. Freimuth, and A. P. Kampf. Critical buckling for the disappearance of superconductivity in rare-earth-doped $La_{2-x}Sr_xCuO_4$. *Phys. Rev. Lett.*, 73(13):1841–1844, 1994.

[188] M K Crawford, R L Harlow, S Deemyad, V Tissen, J S Schilling, E M Mccarron, S W Tozer, D E Cox, N Ichikawa, S Uchida, and Q Huang. High-pressure study of structural phase transitions and superconductivity in $La_{1.48}Nd_{0.4}Sr_{0.12}CuO_4$. *Phys. Rev. B*, 71:104513, 2005.

[189] M. Haruta, T. Nagai, N. R. Lugg, M. J. Neish, M. Nagao, K. Kurashima, L. J. Allen, T. Mizoguchi, and K. Kimoto. Atomic resolution chemical bond analysis of oxygen in La_2CuO_4. *J. Appl. Phys.*, 114(8):2–10, 2013.

[190] S. B. Wilkins, M. P. M. Dean, Jörg Fink, Markus Hücker, J. Geck, V. Soltwisch, E. Schierle, E. Weschke, G. Gu, S. Uchida, N. Ichikawa, J. M. Tranquada, and J. P. Hill. Comparison of stripe modulations in $La_{1.875}Ba_{0.125}CuO_4$ and $La_{1.48}Nd_{0.4}Sr_{0.12}CuO_4$. *Phys. Rev. B*, 84(19):195101, Nov 2011.

[191] M Braden, W Schnelle, W Schwarz, N Pyka, G Heger, Z Fisk, K Gamayunov, I Tanaka, and H Kojima. Elastic and inelastic neutron scattering studies on the tetragonal to orthorhombic phase transition of $La_{2-x}Sr_xCuO_{4\pm\delta}$. *Zeitschrift für Phys. B Condens. Matter*, 94(1-2):29–37, Mar 1994.

[192] Jungho Kim, H. Zhang, G. D. Gu, and Young-June Kim. Charge Stripes and Superconductivity in $La_{2-x}Ba_xCuO_4$ and $La_{1.6-x}Nd_{0.4}Sr_xCuO_4$. *J. Supercond. Nov. Magn.*, 22(3):251–254, 2009.

[193] M. Fujita, K. Yamada, H. Hiraka, P. Gehring, S. Lee, S. Wakimoto, and G. Shirane. Static magnetic correlations near the insulating-superconducting phase boundary in $La_{2-x}Sr_xCuO_4$. *Phys. Rev. B*, 65(6):064505, 2002.

[194] H. Kimura, Y. Noda, H. Goka, M. Fujita, K. Yamada, M. Mizumaki, N. Ikeda, and H. Ohsumi. Relationship between charge stripe order and structural phase transitions in $La_{1.875}Ba_{0.125-x}Sr_xCuO_4$. *Phys. Rev. B - Condens. Matter Mater. Phys.*, 70(13):1–8, 2004.

[195] M Sera, Y. Ando, S Kondoh, K Fukuda, M Sato, I Watanabe, S. Nakashima, and K. Kumagai. Transport and magnetic anomalies at the structural transition to the

new low temperature phase in $La_{2-x}Ba_xCuO_4$. *Solid State Commun.*, 69(8):851–855, Feb 1989.

[196] Tineke Thio, C. Y. Chen, B. S. Freer, D. R. Gabbe, H. P. Jenssen, M. A. Kastner, P. J. Picone, N. W. Preyer, and R. J. Birgeneau. Magnetoresistance and the spin-flop transition in single-crystal La_2CuO_{4+y}. *Phys. Rev. B*, 41(1):231–239, 1990.

[197] B Keimer, R J Birgeneau, A Cassanho, Y Endoh, M Greven, M A Kastner, and G Shirane. Soft phonon behavior and magnetism at the low temperature structural phase transition of $La_{1.65}Nd_{0.35}CuO_4$. *Z. Phys. B*, 91:373, 1993.

[198] N. Bonesteel, T. Rice, and F. Zhang. Spin-orbit coupling and spirals in doped La_2CuO_4. *Phys. Rev. Lett.*, 68(17):2684–2687, 1992.

[199] W E Pickett, R E Cohen, and H Krakauer. Lattice instabilities, isotope effect, and high-T_c superconductivity in $La_{2-x}Ba_xCuO_4$. *Phys. Rev. Lett.*, 67(2):228–231, 1991.

[200] L. Shekhtman, Amnon Aharony, and O. Entin-Wohlman. Bond-dependent symmetric and antisymmetric superexchange interactions in La_2CuO_4. *Phys. Rev. B*, 47(1):174–182, 1993.

[201] A R Moodenbaugh, Youwen Xu, M. Suenaga, T. J. Folkerts, and R. N. Shelton. Superconducting properties of $La_{2-x}Ba_xCuO_4$. *Phys. Rev. B*, 38(7):4596–4600, Sep 1988.

[202] S J L Billinge, G H Kwei, A C Lawson, and J D Thompson. Superconductivity and the Low-Temperature Orthorhombic to Tetragonal Phase Transition in $La_{2-x}Ba_xCu0_4$. 71(12):15–17, 1993.

[203] Ken-ichi Kumagai, Hirozumi Matoba, Nobuo Wada, Masahiro Okaji, and Koichi Nara. Some Anomalies Due to the Low-Temperature Structural Transition around $x = 0.12$ in $La_{2-x}Ba_xCuO_4$. *J. Phys. Soc. Japan*, 60:1448–1451, 1991.

[204] M. K. Crawford, R. L. Harlow, E. M. McCarron, W. E. Farneth, J. D. Axe, H. Chou, and Q. Huang. Lattice instabilities and the effect of copper-oxygen-sheet distortions on superconductivity in doped La_2CuO_4. *Phys. Rev. B*, 44(14):7749–7752, 1991.

[205] Y Nakamura and S Uchida. Anisotropic transport properties of single-crystal $La_{2-x-y}Nd_ySr_xCuO_4$: Effect of the structural phase transition. *Phys. Rev. B. Condens. Matter*, 46(9):5841–5844, 1992.

[206] B. Büchner, M. Breuer, M. Cramm, A. Freimuth, H. Micklitz, W. Schlabitz, and A. P. Kampf. Superconducting/non-superconducting phase boundary in the low temperature tetragonal phase of (La,RE)-Sr-Cu-O. *J. Low Temp. Phys.*, 95(1-2):285–291, 1994.

[207] R S Markiewicz. Structural phase transitions and superconductivity in $La_{2-x}A_xCuO_4$, A=Sr,Ba. *J. Phys. Condens. Matter*, 2(28):6223–6226, Jul 1990.

[208] S. Barišić and J. Zelenko. Electron mechanism for the structural phase transitions in $La_{2-x}Ba_xCuO_4$. *Solid State Commun.*, 74(5):367–370, May 1990.

[209] C. M. Varma. Pseudogap Phase and the Quantum-Critical Point in Copper-Oxide Metals. *Phys. Rev. Lett.*, 83(17):3538–3541, Oct 1999.

[210] C. M. Varma. Theory of the pseudogap state of the cuprates. *Phys. Rev. B*, 73(15):155113, 2006.

[211] T. M. Rice, Kai-Yu Yang, and F. C. Zhang. A phenomenological theory of the anomalous pseudogap phase in underdoped cuprates. *Reports Prog. Phys.*, 75(1):016502, Jan 2012.

[212] B. Keimer, S. A. Kivelson, M. R. Norman, S. Uchida, and J. Zaanen. From quantum matter to high-temperature superconductivity in copper oxides. *Nature*, 518(7538):179–186, Feb 2015.

[213] B. Fauqué, Y. Sidis, V. Hinkov, S. Pailhès, C. T. Lin, X. Chaud, and P. Bourges. Magnetic order in the pseudogap phase of high-TC superconductors. *Phys. Rev. Lett.*, 96(19):1–4, 2006.

[214] Laimei Nie, Gilles Tarjus, and S. A. Kivelson. Quenched disorder and vestigial nematicity in the pseudogap regime of the cuprates. *Proc. Natl. Acad. Sci.*, 111(22):7980–7985, Jun 2014.

[215] S. Bulut, W. A. Atkinson, and A. P. Kampf. Spatially modulated electronic nematicity in the three-band model of cuprate superconductors. *Phys. Rev. B*, 88(15):155132, Oct 2013.

[216] Ruixing Liang, D A Bonn, and Walter N Hardy. Preparation and X-ray characterization of highly ordered ortho-II phase $YBa_2Cu_3O_{6.50}$ single crystals. *Phys. C Supercond.*, 336(1–2):57–62, 2000.

[217] N. Nücker, E. Pellegrin, P. Schweiss, J. Fink, S. Molodtsov, C. Simmons, G. Kaindl, W. Frentrup, A. Erb, and G. Müller-Vogt. Site-specific and doping-dependent electronic structure of YBa2Cu3Ox probed by O 1s and Cu 2p x-ray-absorption spectroscopy. *Phys. Rev. B*, 51(13):8529–8542, Apr 1995.

[218] M Merz, N Nücker, P Schweiss, S Schuppler, C. Chen, V Chakarian, J Freeland, Y. Idzerda, M Kläser, G. Müller-Vogt, and Th Wolf. Site-Specific X-Ray Absorption Spectroscopy of Y1-xCaxBa2Cu3O7-y: Overdoping and Role of Apical Oxygen for High Temperature Superconductivity. *Phys. Rev. Lett.*, 80(23):5192–5195, Jun 1998.

[219] A. Krol, Z. H. Ming, Y. H. Kao, N. Nücker, G. Roth, J. Fink, G. C. Smith, Key Taeck Park, Jaejun Yu, A. J. Freeman, A. Erband, G. Müller-Vogt, J. Karpinski, E. Kaldis, and K. Schönmann. Hole states inCuO_2 planes and Cu-O chains of $YBa_2Cu_4O_8$ probed by soft-x-ray absorption spectroscopy. *Phys. Rev. B*, 45(5):2581–2584, Feb 1992.

[220] J. A. Yarmoff, D. R. Clarke, W. Drube, U. O. Karlsson, A. Taleb-Ibrahimi, and F. J. Himpsel. Valence electronic structure of $Y_1Ba_2Cu_3O_7$. *Phys. Rev. B*, 36(7):3967–3970, Sep 1987.

[221] P. Kuiper, G. Kruizinga, J. Ghijsen, M. Grioni, P. J. W. Weijs, F. M. F. de Groot, G. A. Sawatzky, H. Verweij, L. F. Feiner, and H. Petersen. X-ray absorption study of the O $2p$ hole concentration dependence on O stoichiometry in $YBa_2Cu_3O_x$. *Phys. Rev. B*, 38(10):6483–6489, Oct 1988.

[222] M. Grioni, J. F. van Acker, M. T. Czyžyk, and J. C. Fuggle. Unoccupied electronic structure and core-hole effects in the x-ray-absorption spectra of Cu_2O. *Phys. Rev. B*, 45(7):3309–3318, Feb 1992.

[223] N. Mannella, A. Rosenhahn, M. Watanabe, B. Sell, A. Nambu, S. Ritchey, E. Arenholz, A. Young, Y. Tomioka, and C. S. Fadley. Temperature-dependent x-ray absorption spectroscopy of colossal magnetoresistive perovskites. *Phys. Rev. B - Condens. Matter Mater. Phys.*, 71(12):1–5, 2005.

[224] Y. T. Tsai, W. J. Chang, S. W. Huang, J. Y. Lin, J. Y. Lee, J. M. Chen, K. H. Wu, T. M. Uen, Y. S. Gou, and J. Y. Juang. Temperature-dependent X-ray absorption near edge spectroscopy of doped $LaMnO_3$: Ion-size and the Jahn-Teller distortion effects. *Phys. B Condens. Matter*, 404(8-11):1404–1408, 2009.

[225] D. Testemale, J.L. Hazemann, H. Emerich, B. Etschmann, W. Liu, J. Brugger, O. Proux, and W. van Beek. An XAS study of the structure and thermodynamics of Cu(I) chloride complexes in brines up to high temperature (400°C, 600bar). *Geochim. Cosmochim. Acta*, 71(20):4920–4941, 2007.

[226] G.S. Henderson, P. Lagarde, A.-M. Flank, D.R. Neuville, S. Shoval, D. de Ligny, G. Panczer, L. Cormier, and J. Roux. Silica polymorphs, glass and melt: An in situ high temperature XAS study at the Si K-edge. *J. Non. Cryst. Solids*, 355(18-21):1099–1102, 2009.

[227] F. Bridges, C. H. Booth, G. H. Kwei, J. J. Neumeier, and G. A. Sawatzky. Temperature dependent changes of the Mn $3d$ and $4p$ bands near T_c in colossal magnetoresistance systems: XANES study of $La_{1-x}Ca_xMnO_3$. *Phys. Rev. B*, 61(14):R9237–R9240, Apr 2000.

[228] Q. Qian, T. A. Tyson, C.-C. Kao, M. Croft, S.-W. Cheong, and M. Greenblatt. Thermal effects in the x-ray spectra of $La_{1-x}Ca_xMnO_3$. *Phys. Rev. B*, 62(20):13472–13481, Nov 2000.

[229] K. B. Garg, S. Dalela, N. L. Saini, R. K. Singhal, D. C. Jain, and C. T. Chen. Polarised XAS study of anomalous temperature dependence of aggregation of itinerant holes and pair formation in a $YBa_2Cu_3O_{7-\delta}$ single crystal. *Phys. C Supercond. its Appl.*, 399(3-4):98–106, 2003.

[230] Martin Magnuson, Thorsten Schmitt, and Laurent C. Duda. Polarization-dependent resonant inelastic X-ray scattering study at the Cu L and O K-edges of $YBa_2Cu_3O_{7-x}$. *J. Electron Spectros. Relat. Phenomena*, 224(July):38–44, 2018.

[231] J. N. Hancock, G. Chabot-Couture, and M. Greven. Lattice coupling and Franck-Condon effects in K-edge resonant inelastic X-ray scattering. *New J. Phys.*, 12:1–10, 2010.

[232] F. Hennies, S. Polyutov, I. Minkov, A. Pietzsch, M. Nagasono, F. Gel'mukhanov, L. Triguero, M.-N. Piancastelli, W. Wurth, H. Ågren, and A. Föhlisch. Nonadiabatic Effects in Resonant Inelastic X-Ray Scattering. *Phys. Rev. Lett.*, 95(16):163002, Oct 2005.

[233] Mathias P. Ljungberg. Vibrational effects in x-ray absorption and resonant inelastic x-ray scattering using a semiclassical scheme. *Phys. Rev. B*, 96(21):1–12, 2017.

[234] Shin-ichi Uchida. *High Temperature Superconductivity*. Springer, 2015.

[235] Anna E. Böhmer and Andreas Kreisel. Nematicity, magnetism and superconductivity in FeSe. *J. Phys. Condens. Matter*, 30(2), 2018.

[236] Lauren E Hayward, David G Hawthorn, Roger G Melko, and Subir Sachdev. Angular fluctuations of a multicomponent order describe the pseudogap of $YBa_2Cu_3O_{6+x}$. *Science*, 343(6177):1336–9, Mar 2014.

[237] Youichi Yamakawa, Seiichiro Onari, and Hiroshi Kontani. Nematicity and magnetism in FeSe and other families of Fe-based superconductors. *Phys. Rev. X*, 6(2):1–15, 2016.

[238] John M. Tranquada. Spins, stripes, and superconductivity in hole-doped cuprates. In *AIP Conf. Proc.*, volume 1550, pages 114–187, 2013.

[239] Andrej Mesaros, Kazuhiro Fujita, Stephen D. Edkins, Mohammad H. Hamidian, Hiroshi Eisaki, Shin-ichi Uchida, J. C. Séamus Davis, Michael J. Lawler, and Eun-Ah Kim. Commensurate $4a_0$-period charge density modulations throughout the $Bi_2Sr_2CaCu_2O_{8+x}$ pseudogap regime. *Proc. Natl. Acad. Sci.*, 113(45):12661–12666, 2016.

[240] R. M. Fernandes, A. V. Chubukov, and J. Schmalian. What drives nematic order in iron-based superconductors? *Nat. Phys.*, 10(2):97–104, 2014.

[241] Rafael M. Fernandes and Andrew J. Millis. Nematicity as a probe of superconducting pairing in iron-based superconductors. *Phys. Rev. Lett.*, 111(12):1–5, 2013.

[242] Yann Gallais and Indranil Paul. Charge nematicity and electronic Raman scattering in iron-based superconductors. *Comptes Rendus Phys.*, 17(1-2):113–139, 2016.

[243] Eduardo H. da Silva Neto, Riccardo Comin, Feizhou He, Ronny Sutarto, Yeping Jiang, Richard L Greene, George a Sawatzky, and Andrea Damascelli. Charge ordering in the electron-doped superconductor $Nd_{2-x}Ce_xCuO_4$. *Science*, 347(6219):282–285, 2015.

[244] L. Fanfarillo, G. Giovannetti, M. Capone, and E. Bascones. Nematicity at the Hund's metal crossover in iron superconductors. *Phys. Rev. B*, 95(14):1–7, 2017.

[245] Tao Wu, Hadrien Mayaffre, Steffen Krämer, Mladen Horvatic, Claude Berthier, W. N. Hardy, Ruixing Liang, D. A. Bonn, and Marc Henri Julien. Incipient charge order observed by NMR in the normal state of $YBa_2Cu_3O_y$. *Nat. Commun.*, 6(96), 2015.

[246] Patrick A. Lee, Naoto Nagaosa, and Xiao Gang Wen. Doping a Mott insulator: Physics of high-temperature superconductivity. *Rev. Mod. Phys.*, 78(1), 2006.

[247] Fa Wang, Steven A. Kivelson, and Dung Hai Lee. Nematicity and quantum paramagnetism in FeSe. *Nat. Phys.*, 11(11):959–963, 2015.

[248] D. C. Peets, D. G. Hawthorn, K. M. Shen, Young-June Kim, D. S. Ellis, H. Zhang, Seiki Komiya, Yoichi Ando, G. a. Sawatzky, Ruixing Liang, D. a. Bonn, and W. N. Hardy. X-Ray Absorption Spectra Reveal the Inapplicability of the Single-Band Hubbard Model to Overdoped Cuprate Superconductors. *Phys. Rev. Lett.*, 103(8):087402, Aug 2009.

[249] M. E. Simon and C. M. Varma. Detection and Implications of a Time-Reversal Breaking State in Underdoped Cuprates. *Phys. Rev. Lett.*, 89(24):247003, 2002.

[250] Ziqiang Wang, Gabriel Kotliar, and Xiao Fang Wang. Flux-density wave and superconducting instability of the staggered-flux phase. *Phys. Rev. B*, 42(13):8690–8693, 1990.